COLLAPSE FRAGILITY ANALYSIS OF REINFORCED CONCRETE TALL BUILDINGS

A THESIS SUBMITTED TO
THE GRADUATE SCHOOL OF NATURAL AND APPLIED SCIENCES
OF
MIDDLE EAST TECHNICAL UNIVERSITY

BY

ERHAN BUDAK

IN PARTIAL FULFILLMENT OF THE REQUIREMENTS
FOR
THE DEGREE OF DOCTOR OF PHILOSOPHY
IN
CIVIL ENGINEERING

SEPTEMBER 2022

Approval of the thesis:

COLLAPSE FRAGILITY ANALYSIS OF REINFORCED CONCRETE TALL BUILDINGS

submitted by **ERHAN BUDAK** in partial fulfillment of the requirements for the degree of **Doctor of Philosophy in Civil Engineering, Middle East Technical University** by,

Prof. Dr. Halil Kalıpçılar
Dean, Graduate School of **Natural and Applied Sciences** _____

Prof. Dr. Erdem Canbay
Head of the Department, **Civil Engineering** _____

Assoc. Prof. Dr. Ozan Cem Çelik
Supervisor, **Civil Engineering, METU** _____

Prof. Dr. Halûk Sucuoğlu
Co-Supervisor, **Civil Engineering, METU** _____

Examining Committee Members:

Prof. Dr. Murat Altuğ Erberik
Civil Engineering, METU _____

Assoc. Prof. Dr. Ozan Cem Çelik
Civil Engineering, METU _____

Assist. Prof. Dr. Bekir Özer Ay
Architecture, METU _____

Prof. Dr. Serdar Soyöz
Civil Engineering, Boğaziçi University _____

Assoc. Prof. Dr. Ufuk Yazgan
Civil Engineering, Istanbul Technical University _____

Date: 02.09.2022

I hereby declare that all information in this document has been obtained and presented in accordance with academic rules and ethical conduct. I also declare that, as required by these rules and conduct, I have fully cited and referenced all material and results that are not original to this work.

Name, Last name: Erhan Budak

Signature:

ABSTRACT

COLLAPSE FRAGILITY ANALYSIS OF REINFORCED CONCRETE TALL BUILDINGS

Budak, Erhan
Doctor of Philosophy, Civil Engineering
Supervisor: Assoc. Prof. Dr. Ozan Cem Çelik
Co-Supervisor: Prof. Dr. Halûk Sucuoğlu

September 2022, 161 pages

Seismic performance of a 253 m tall reinforced concrete core wall building in Istanbul, designed according to performance-based seismic design principles, was assessed to determine the response parameters that control the serviceability, safety and collapse performance limit states. An ambient vibration test of the building was performed to identify its dynamic properties, including the damping properties for service loads. A three-dimensional linear elastic finite element structural model of the building was developed and validated with the in-situ dynamic properties, which was the basis for the nonlinear finite element model developed subsequently. The collapse capacity of the building was determined using incremental dynamic analysis. Structure- and member-specific seismic fragility curves were derived and the performance of the building at various levels of earthquake hazard in the region was evaluated. The intensities and annual occurrence frequencies of earthquake ground motions leading to local and global collapse were calculated. The effects of the angle of seismic incidence on structural response and consequently on seismic fragilities were discussed. The findings of this study will further improve the understanding of the seismic performance of tall concrete core wall buildings with outrigger systems under different seismic hazard levels.

Keywords: Dynamic Tests, Earthquakes, Fragility, High-Rise Buildings, Seismic Design

ÖZ

BETONARME YÜKSEK BİNALARIN GÖÇME KIRILGANLIK ANALİZİ

Budak, Erhan
Doktora, İnşaat Mühendisliği
Tez Yöneticisi: Doç. Dr. Ozan Cem Çelik
Ortak Tez Yöneticisi: Prof. Dr. Halûk Sucuoğlu

Eylül 2022, 161sayfa

İstanbul'da performansa dayalı sismik tasarım ilkelerine göre tasarlanmış 253 m yüksekliğinde bir betonarme çekirdek duvarlı binanın deprem performansı, servis, güvenlik ve göçme performans sınır durumlarını kontrol eden tepki parametrelerinin belirlenmesi için değerlendirilmiştir. Sönümleme özellikleri de dahil olmak üzere yapının dinamik özelliklerini belirlemek için çevresel titreşim testi yapılmıştır. Binanın üç boyutlu doğrusal elastik sonlu elemanlar modeli geliştirilmiş ve çevresel titreşim testinden elde edilen dinamik özelliklerle doğrulanmıştır. Bu model daha sonra geliştirilen yapının doğrusal olmayan sonlu elemanlar modelinin temeli olmuştur. Artımlı dinamik analiz yöntemi kullanılarak binanın çökme kapasitesi hesaplanmıştır. Yapıya ve elemana özgü sismik kırılganlık ilişkileri elde edilmiş ve binanın bölgedeki çeşitli deprem tehlikesi seviyelerindeki performansı değerlendirilmiştir. Kısmi ve tam göçmeye neden olan deprem yer hareketlerinin şiddetleri ve yıllık oluşum frekansları hesaplanmıştır. Deprem geliş açısının yapının üzerindeki etkileri ve sismik kırılganlık eğrileri üzerindeki etkisi irdelenmiştir. Bu araştırmanın bulguları, farklı sismik tehlike seviyeleri altında tasarlanan dış destekli çekirdek perdeli sistemlere sahip betonarme yüksek yapıların deprem performansının anlaşılmasını geliştirecektir.

Anahtar Kelimeler: Depremler, Dinamik Testler, Kırılganlık, Sismik Tasarım, Yüksek Binalar

To my family

ACKNOWLEDGEMENTS

I would like to express my deepest gratitude to my supervisor Dr. Ozan Cem Çelik and co-supervisor Dr. Halûk Sucuoğlu for their guidance, advice, criticism, encouragements and insight throughout this study.

I would also like to thank my thesis committee members Dr. Murat Altuğ Erberik for his advice and contributions throughout this study and Dr. Bekir Özer Ay for his help in ground motion selection and advice throughout this study, and my external thesis committee members Dr. Serdar Soyöz and Dr. Ufuk Yazgan for their suggestions on improving this thesis.

I would like to extend my thanks to Dr. Sinan Akkar and Dr. Erkan Özer, peer reviewers of the tall building investigated in this study, whom I have discussed the design details, and Design Group Inc. for providing the design data of the building.

I would like to thank Suleyman Tunç and Mustafa Hatipoğlu for cabling the accelerometers and providing technical assistance on the data acquisition system, and Hasan Metin and Oğuzhan Gümüş for mounting the accelerometers during the ambient vibration test of the building.

I would like to thank to Dr. Alper Aldemir for being a supportive big brother, teacher and friend to me. He also deserves my appreciation as he has always been with me in my hard times with his knowledge and guidance.

I would also like to thank my precious colleagues İsmail Ozan Demirel, Dr. Gizem Mestav Sarıca, Müge Özgenoğlu, Beyazıt Bestami Aydın, Yunus İşıkli, Yavuz Semerdöken, Dr. Rehber Akdoğan for their support, encouragement and patience in this period.

A very special thanks goes to my dear wife Nazlıcan Gültekin Budak for the enormous support and love she has given to me during the course of this study. Thanks to her understanding and never ending encouragement, I was able to get

through the hard times and keep my focus. Her immense love and emotional support are gratefully acknowledged.

I would like to thank to our little sweet boy Tekin Efe. You are our hero.

Finally, my deepest gratitude goes to my parents, sisters and brothers for their endless support and encouragement throughout my graduate studies. This dissertation would not have been possible without them.

TABLE OF CONTENTS

LIST OF TABLES

TABLES

LIST OF FIGURES

FIGURES

CHAPTER 1

INTRODUCTION

1.1 Background

The population of tall buildings, with a signification portion in regions of high seismicity, is steadily increasing in the world. In non-seismic regions, design of tall buildings under gravity and wind loading is well developed and has a history longer than a century. However, tall building boom in seismic regions is a fairly new phenomenon. In Istanbul, the number of buildings taller than 100 m has exceeded 200 [Budak et al. 2018]. Tall buildings are unique in architectural and structural features when compared to ordinary multistory buildings. These differences become more prominent in seismic zones where seismicity and unique dynamic building characteristics dominate structural design. Past seismic design practices and code-based prescriptive procedures developed for ordinary buildings may not promote the desired behavior for tall buildings under earthquake excitations [Moehle 2008; Budak and Sucuoglu 2016]. Hence, chapters devoted particularly to tall buildings have been included in the recent seismic design codes, or pertinent guidelines have been developed [AFAD 2018a; LATBSDC 2020; PEER 2017; SEONAC 2007]. Seismic design of modern tall buildings are mostly performed by engineering experience and knowledge, relying heavily on sophisticated computer software.

There are three major difficulties in the seismic design of tall buildings in regions of high seismicity. First, seismic codes and guidelines for regulating tall building design have been published fairly recently and they are mostly informative, not yet legally binding (except the Turkish Building Earthquake Code, (TBEC) [AFAD 2018a]). Second, tall buildings are not typical in their structural systems. There is even no consensus on the description of a tall building. Design engineers are developing new forms by adopting new member types and materials for approaching increased

heights. Third, although some tall buildings in seismic regions have experienced strong ground shaking, quite limited information was reported following the post-earthquake investigations on these buildings [Celebi et al. 2017a]. No tall building has collapsed or severely damaged so far under the loads considered in their design. However, there is no adequate reliable data on the damage sustained by existing tall buildings under strong earthquakes as well as the societal impact of this damage, both economical and psychological.

Given the complexity and geometry of tall buildings, scaled laboratory studies are unlikely to provide accurate results for the actual structural systems. Accordingly, non-destructive dynamic field tests such as ambient vibration tests are performed to identify the dynamic properties (natural vibration frequencies, modal damping ratios, etc.) of existing tall buildings. Notwithstanding the large number of such studies in the literature [Pan et al. 2016, Celebi et al. 2013b; 2017b; 2019], the identified dynamic properties were rarely used in validating the finite element structural models of tall buildings due to the complexity and different sources of uncertainties involved in the model updating process [Zhou et al. 2017]. Hence, most ambient vibration studies were recorded response data-driven studies and did not incorporate finite element modeling. Some of them provided the dynamic properties that were reported by the designers based on the finite element models used in design calculations [Pan et al. 2016; Celebi 2016; Celebi et al. 2013b; 2017b; 2019]. In the light of these studies on instrumented structures, a database of dynamic properties can be assembled to improve the design and analysis of tall buildings. One important outcome of such studies is that the critical damping ratio used in the design of tall buildings was reduced to 2.5% from the almost universally adopted 5% [LATBSDC 2015], and yet again changed and given as a function of the building height [LATBSDC 2017].

Seismic risk assessment requires probabilistic prediction of the safety and performance of buildings under uncertain future seismic actions. Seismic fragility curves play a central role in regional seismic risk and loss estimation and in developing seismic codes [Rossetto and Elnashai 2003]. There has been a growing

need for fragility curves of tall buildings due to their increased presence in the building inventories of most cities in the last decade. There is limited observational or empirical data about the effects of earthquakes on tall buildings and hence, the only viable method to derive seismic fragilities of tall buildings is analytical simulations. Uncertainties in seismic hazard, ground motions, structural system and material properties, structural modeling parameters, and damage and loss analyses should all be incorporated in the development seismic fragilities of tall buildings. Three-dimensional (3-D) nonlinear dynamic analyses required to consider different sources of uncertainties are computationally demanding. Hence, researchers have focused on the uncertainties that have the greatest impact on seismic fragilities [Rigato and Medina 2007; Skoulidou and Romao 2019; 2020].

This study focuses on the behavior of reinforced concrete (RC) tall buildings with outrigger systems in seismic regions. An existing tall building in Istanbul is selected as the case study building, which will be subjected to an ambient vibration test. Nonlinear dynamic analyses will be performed using a 3-D finite element model to derive the seismic fragility curves of the building with particular emphasis for the collapse limit states. The effect of angle of seismic incidence (ASI) on the fragilities will also be investigated especially due to the parallelogram footprint of the building.

1.2 Objectives and Scope

The objective of this study is to investigate the structural response of an existing tall building with an RC core wall and outrigger system in Istanbul and assess its seismic performance through building-specific fragility curves. The following critical steps are necessary to achieve the goals of this study:

(1) Perform an ambient vibration test of the building to identify its in-situ dynamic characteristics, including damping properties for service loads.

(2) Develop a 3-D linear elastic finite element structural model of the building, determine its natural vibration periods and mode shapes, and validate them with the in-situ dynamic properties.

(3) Develop a 3-D nonlinear finite element model of the building.

(4) Investigate and identify the critical structure- and member-specific response parameters that significantly control the serviceability, safety and collapse performances of the building.

(5) Derive structure- and member-specific seismic fragility curves and evaluate the performance of the building at various levels of earthquake hazard in the region.

(6) Investigate the effect of ASI on structural response and subsequently on seismic fragilities.

The findings of this study will further improve the understanding of the seismic performance of tall concrete core wall buildings with outrigger systems under strong earthquake excitations.

1.3 Thesis Outline

This chapter has presented the context of this study, which will be addressed in the subsequent chapters.

Chapter 2 presents a brief literature review on in-situ dynamic tests with particular emphasis on ambient vibration tests of instrumented tall buildings, seismic performance and fragility analysis of tall buildings and the effect of ASI on structural response.

Chapter 3 describes the building characteristics and presents the performance-based structural design of the tall building in Istanbul, which is selected for this study, develops the 3-D linear and nonlinear finite element models of the building and presents the selected strong earthquake ground motions based on the previous probabilistic seismic hazard analysis carried out for the building site.

Chapter 4 presents the temporary monitoring scheme of the building, identification of its dynamic characteristics from the recorded ambient vibration responses, comparisons of the in-situ dynamic properties with those from its finite element model, critical damping ratio statistics for service-level evaluations and the simulated floor accelerations when the building is subjected to the 2019 M_w 5.8 Marmara Sea earthquake ground motions.

Chapter 5 presents the performance-based seismic design evaluation of the building, identifying the controlling response parameters, and defines the partial collapse and near collapse failure stages of the building.

Chapter 6 derives the seismic fragility curves of the building, evaluates its seismic vulnerability and investigates the effect of ASI on structural response and seismic fragilities.

Finally, Chapter 7 presents a summary of the research, major conclusions drawn from this study and future research.

CHAPTER 2

LITERATUARE REVIEW

2.1 Introduction

This chapter summarizes previous studies on the recorded ambient vibration and earthquake responses of instrumented tall buildings, the seismic performance and fragility analysis of tall buildings and the effect of ASI on structural response.

2.2 Ambient Vibration and Earthquake Response Records of Instrumented Tall Buildings

Dynamic properties of existing structures can be identified by in-situ dynamic tests. These tests can be categorized into three groups depending on the source of excitations: forced vibration, ambient vibration and seismic monitoring. In forced vibration testing, structural responses are recorded while sweeping the frequency of the vibration generator. Once the steady-state responses are extracted at each operated frequency [Celik and Gulkan 2021a], relatively straightforward methods are used for identifying the dynamic properties as compared to those in ambient vibration testing and seismic monitoring. However, forced vibration testing has a number of shortcomings [Celik and Gulkan 2021b]. It is not practical to excite very large and massive structures by a vibration generator. Transportation and mounting of the vibration generator is not an easy task. Although forced vibration tests are non-destructive dynamic tests, occupants especially at the upper floors can sense the structural vibrations near resonance frequencies in these tests [Celik et al. 2015]. Moreover, the operating frequency range of the vibration generator limits the natural vibration frequencies that can be identified, which is not the case in ambient vibration testing. Wind induced ambient excitation is assumed as a white noise random process

that has a flat frequency spectrum. Ambient vibration testing is considered as a favorable and economical non-destructive test method for identifying the dynamic properties of structures [Ventura et al. 2005]. On the other hand, data collected from instrumented structures when subjected to strong earthquake excitations are of utmost importance for understanding the actual behavior of structures under design-level loads.

In-situ dynamic testing of any tall building is important for identifying its unique dynamic characteristics. If such tests are also accompanied by finite element simulations then structural modeling approaches for various structural systems can be improved. However, such studies are limited in the literature [Zhou et al. 2017]. Some studies reported the available dynamic properties from the finite element models that were developed by the designers for design calculations, without any attempt to reflect the test conditions of the buildings and to match the identified dynamic properties [Pan et al. 2016; Celebi et al. 2013a; 2013b; 2016; 2017a; 2017b]. Finite element structural models can be updated with the knowledge of natural vibration frequencies, mode shapes and modal damping ratios. Studies on instrumented structures have helped developing a database of dynamic properties of different structural systems. Design and analysis of buildings can be improved by using these data [Celebi et al. 2017a].

Celebi et al. [2013a] identified the dynamic properties of a 19-story RC dual core-wall and frame building in Chile from the aftershock records of the 2010 M_w 8.8 Maule, Chile earthquake. No damage was observed during the earthquake excitation. The recorded peak ground acceleration (PGA) at the building site during the aftershock was 0.002 g. In the finite element model of the building, gross section properties were used together with the modulus of elasticity for concrete per ACI 318 [ACI 2014], fixed support conditions were employed and rigid diaphragms were defined at all floors. The natural vibration frequencies determined from its finite element model without any live loads, consistent with the aftershock state of the building, matched the identified frequencies. Beating effects were also observed in the recorded responses.

Celebi et al. [2013b] analyzed the ambient vibration records of an instrumented 64-story RC core wall building with unique dynamic response modification features. The identified dynamic properties were significantly different than those computed using design-level analyses, which was attributed to the buckling-restrained braces and tuned liquid sloshing dampers expected to contribute to the building response at strong levels of shaking.

Pan et al. [2016] identified the dynamic properties of a 128-story building in Shanghai from its ambient vibration records. The first-mode natural frequencies in the North-South (N-S), East-West (E-W) and torsional directions were identified as 0.11 Hz, 0.11 Hz and 0.22 Hz respectively. These frequencies matched those determined from the finite element model of the building, which was used for the design of the building. The associated modal damping ratios were 1.7%, 1.7% and 0.9%, respectively.

Zhou et al. [2017] identified the dynamic properties of 10 RC tall buildings, three of them with shear wall and frame structural systems and seven of them with shear wall structural systems, from their ambient vibration records. The identified natural vibration periods were compared with those determined from the finite element models that were taking into account the mass and stiffness of the infill walls. The models in which the infill walls were modeled using shell elements or diagonal struts yielded quite close natural periods to those identified from the ambient records. The fundamental periods were also compared with those computed using 25 different empirical equations.

Celebi [2017] identified the dynamic properties of a 58-story RC dual core shear wall and outrigger frame building from the 2014 M_w 6.0 Napa and the 2011 M_w 3.8 Berkeley earthquakes. The recorded accelerations at the basement level of the building from these records were 0.01 g and 0.012 g, respectively. The identified first-mode natural frequencies were 0.25 Hz, 0.28 Hz and 0.43 Hz in the N-S, E-W and torsional directions, respectively. The recorded maximum interstory drift ratio (IDR) was about 0.015%. The identified mode shapes were not affected by the

presence of outrigger frames due to small amplitude vibrations caused by these earthquakes. Damping ratios less than 1% were extracted from both earthquake records.

Zhang et al. [2018] identified the dynamic properties of a 127-story, 632 m super-tall building from its ambient vibration records and reduced-scale shake table tests. The identified fundamental period of the building was 10 s.

2.3 Seismic Performance and Fragility Analysis of Tall Buildings

Research studies on existing tall buildings investigating the relationship between the adopted seismic design criteria and the achieved seismic performance are limited in literature [Korista et al. 1997; Fan et al. 2009; Wang et al. 2017; Bilotta et al. 2018]. Lu et al. [2013] carried out the collapse simulation of a 550 m tall, 119-story mega-braced frame-core tube building (to be built) in China by developing a rigorous nonlinear finite element model. The structural system of the building is common in tall buildings located in highly seismic regions. The finite element simulations revealed that the main collapse mode of this super-tall building is of vertical "pancake" type. Furthermore, the collapse regions do not necessarily coincide with the initial plastic zones predicted by the nonlinear time history analysis (NTHA) under maximum considered earthquake (MCE). Shome et al. [2015] analyzed two 42-story tall RC buildings with a dual system and a core wall system, and a 40-story buckling-restrained braced steel building that were designed using various design standards and guidelines, under a variety of earthquake ground motions. The objective was estimating the mean monetary loss and its uncertainty based on the PEER performance-based earthquake engineering methodology [PEER 2010]. The dual-system building was found to perform better than the other buildings.

Seismic risk assessment requires probabilistic prediction of the safety and performance of buildings under uncertain future seismic actions. Multiple disciplines, including engineering seismology, structural engineering and building

economics, are involved in this process. All information from these distinct disciplines should be incorporated in a probabilistic assessment framework efficiently [Ellingwood et al. 2007]. Seismic fragility analysis constitutes the structural engineering component of this framework. Seismic fragility curve is a probabilistic tool representing the probability of reaching a damage state (or a performance level) given the seismic hazard. In other words, seismic fragility curve is the conditional probability of reaching a structural damage state as a function of a ground motion intensity measure (IM). A lognormal cumulative distribution function (CDF) is often used to define a collapse fragility function:

$$P(\text{Collapse}|IM = x) = \Phi\left[\frac{\ln(x/m_R)}{\beta}\right] \tag{2.1}$$

where $P(\text{Collapse}|IM = x)$ is the probability that a ground motion with an $IM = x$ will cause the structure to collapse, $\Phi[\,]$ is the standard normal CDF, m_R is the median collapse capacity (the IM level at 50% probability of collapse) and β is the logarithmic standard deviation (also referred to as the dispersion of $\ln(IM)$).

In a fragility analysis, the seismic IM represents the seismic hazard and the simulated structural system response is conditioned on this IM. A sufficient and efficient IM is desired in the derivation of seismic fragilities. A sufficient IM results in structural response being independent of any other ground motion characteristics while an efficient IM reduces the variability of the structural response given an IM [Luco and Cornell 2007; Celik and Ellingwood 2010a]. In literature, various IMs (e.g., PGA, peak ground velocity (PGV), spectral acceleration at the fundamental period (T_1) of the structure for 5% damping ($S_a(T_1)$) have been proposed. The use of a particular IM in seismic risk analysis should be guided by the extent to which the IM corresponds to damage to the structural elements.

In literature, there are different approaches for deriving fragility curves. Rossetto and Elnashai [2003] classified the fragility curves into four groups: expert-opinion based, empirical, analytical and hybrid. For example, the fragility curves implemented in the loss estimation software package HAZUS [National Institute of Building

Sciences 1999] are essentially based on expert opinion. Empirical fragility curves are developed based on mostly post-earthquake damage surveys. Damage probability matrices are developed using the collected damage data with the shake map showing the seismic IM distribution. However, such seismic fragilities have some drawbacks. Survey teams are not able to collect data for different building types and damage states. They are subjective in identifying the building damage states. Hence, various shake maps are generated for the same earthquake event. On the other hand, analytical fragility curves are derived using numerical models that simulate the behavior of systems under various seismic IM levels. Hybrid fragility curves are derived using a combination of these approaches [Akkar et al. 2005].

Due to the growing number of tall buildings and lack of seismic risk assessment tools for tall buildings in the form of fragility curves, fragility analysis of tall buildings has become popular in the last decade. However, both the experimental and observational data is very limited [Celebi et al. 2017]. Hence, the only viable method to derive the seismic fragility curves of tall buildings is analytical [Ji et al. 2007a; 2007b; 2009]. This derivation needs comprehensive assessment of the factors that are affecting the seismic response of the unique structural systems of these buildings, as well as accurate estimation of their response [Ji et al. 2007a; 2009; Pejovic and Jankovic 2016].

One of the first studies to derive seismic fragility curves of RC tall buildings was carried out by Ji et al. [2007a; 2007b; 2009]. They used a 2-D nonlinear lumped-mass model for the structural analysis of a 54-story RC building. Among the uncertainties in both seismic demand and capacity computations, the ground motion uncertainty was shown to be the dominant uncertainty in the probabilistic seismic risk analysis consistent with other studies for different structural systems [Porter et al. 2002; Kwon and Elnashai 2006; Kinali and Ellingwood 2007; Celik and Ellingwood 2010b]. Hence, ground motions were treated as the principal source of uncertainty in the analyses. Fragility curves were derived for serviceability, damage control and collapse prevention limit states, which were defined in terms of maximum IDR (IDR_{max}), set at 0.2%, 0.5% and 1.1%, respectively. On the other

hand, HAZUS limit states were defined at IDR_{max} values of 0.2%, 0.5%, 1.5% and 4.0% at the onset of slight, moderate, extensive and complete damage states, respectively, for tall buildings with ductile walls.

Mwafy [2012] derived seismic fragility curves for tall buildings in the United Arab Emirates. 2-D nonlinear finite element models of six reference buildings, 10 to 60 stories tall, were developed. The study showed that as the building height decreases, tall buildings become more vulnerable to earthquake excitations. In addition, they were more vulnerable to seismic demands from severe distant earthquakes than moderate close earthquakes.

Pejovic and Jankovic [2016] derived seismic fragility curves of 20-, 30- and 40-story RC core wall buildings in the Southern Euro-Mediterranean seismic zone for four different limit states. Limit states at the onset of slight, moderate, extensive and complete damage states were defined at IDR_{max} values of 0.25%, 0.5%, 0.9% and 1.6%, respectively.

Alwaeli et al. (2017) developed seismic scenario based building specific performance limit state criteria, in terms of net interstory drift due to shear and flexural deformations, for tall RC wall buildings using a 30-story RC wall building as a case study. They showed that the performance limit states are dependent on the structural system, arrangement and geometry of vertical elements and axial force level in the lower stories.

Zhang and He (2020) carried out seismic collapse risk assessment of a 660 m tall, 118-story building with a typical mega-frame/core-tube/outrigger resisting system. Fragility curves incorporating the uncertainties in material and damping properties were developed, by employing stripe analysis. Peak ground displacement when used as the seismic IM as opposed to PGA and PGV in deriving the fragility curves, the overall uncertainty was significantly reduced. However, the uncertainty in ground motions due to the record-to-record variability was significant consistent with previous studies.

2.4 The Effect of ASI on Structural Response

The structural response, the seismic performance assessment and the development of the seismic fragility curves are affected by the IM used for the ground motion selection and scaling, the number of ground motions or group size that are selected for the evaluation, and the ASI. [Rigato and Medina 2007; Skoulidou et al. 2019; Skoulidou and Romao 2019]. ASI is the angle between the direction of application of the input ground motion with respect to the building's structural axes. The importance of ASI on structural response in line with the type of structure being analyzed, the method of analysis, the aim of the analysis, and the demand and intensity parameters was long recognized in the literature. The effect of ASI on the nonlinear structural response and hence on the seismic fragilities was studied by many researchers [Lucchini et al. 2011; Nguyen and Kim 2013; Fontara et al. 2015; Kostinakis et al. 2015; Kalkan and Reyes 2015].

Fontara et al. [2015] and Nguyen and Kim [2013] analyzed single-story asymmetric buildings under different earthquake ground motions and ASI values. They showed that the effect of ASI on structural response cannot be ignored but there is no specific ASI value (or a range of ASI values) that causes the maximum structural response. Similar conclusions were made by Kalkan and Reyes [2015] based on linear and nonlinear time history analyses of single- and nine-story steel buildings.

Kostinakis et al. [2015] investigated the combined effect of ASI and several structural parameters, such as the ratio of the base shear taken by structural walls, the ratio of horizontal stiffness in two orthogonal directions and structural eccentricity, on eight mid-rise buildings. They concluded that the structural damage is underestimated when the ground motion pairs are applied along the principal axes of the buildings.

Rigato and Medina [2007] investigated the effect of ASI of the ground motion for a single story structure subjected to bi-directional ground motions. The results demonstrated that if an inelastic building is imposed to bi-directional ground motions

only along the principal axes of the building, the obtained inelastic deformation responses are underestimated when compared to those obtained at other ASI. In addition, the critical angle for a given demand parameter varies with the structural properties, the types of structural model and the level of inelastic behavior. Hence, they concluded that performance evaluation and design validation of a building designed to undergo inelastic deformations should ideally be carried out with bi-directional ground motions imposed at several angles according to the principal axis of the building.

Lagaros [2010] analyzed a six story symmetrical and an asymmetrical RC building. The results showed that twenty ground motions imposed along five random ASIs are a good choice to account for the randomness of both the ground motion and the ASI on the estimation of demand parameters in a loss assessment framework.

Giannopoulos and Vamvatsikos [2018] also analyzed a single degree of freedom model and six story steel moment resisting frame building to investigate the effect of ground motion group size and the ASI on the engineer demand parameter. Their study demonstrated that ASI has a lesser effect that of the ground motion group size. Hence, the contribution of the ASI could be ignored.

Skoulidou and Romao [2020] also proposed the minimum number of ASI that should be considered, given as a function of the number ground motions performed in inelastic dynamic analysis. Based on the results, if only mean values of the demands are needed, using only 1 ASI with at the least 30 ground motions should be considered but using 2 or 3ASIs is a good choice for a safer side. In addition, as the ground motion size decreases, the required number of ASI increases to be safer choice. Skoulidou and Romao [2021] also studied the effect of uncertainty related to the ASI of a group of ground motions, as well as to that of the ground motion group size, in seismic loss prediction of RC buildings. Results indicate that the comparative influence of the ground motion group size in the anticipated annual losses is much more crucial when compared to the results obtained for different ASI.

2.5 Summary

Research on existing tall buildings questioning the adopted seismic design criteria and the achieved seismic performances is limited. 3-D nonlinear dynamic analyses required to consider different sources of uncertainties, especially the uncertainty in earthquake ground motions, which was shown to be the dominant uncertainty, in a probabilistic risk assessment framework are computationally demanding. In-situ dynamic properties of tall buildings can be identified by performing ambient vibration tests and can be used in validating the 3-D finite element models for reliable response analysis, which was rarely the case. The effect of ASI on the structural response of buildings taller than 200 m was not investigated previously. Due to their increased presence in the building inventories of most cities and the high consequences of their failure to meet their performance-based design objectives, tall buildings, especially in regions of high seismicity, are particularly important for the safety of the society as a whole. It is evident that there has been an urgent need for seismic risk assessment tools in the form of fragility curves tailored to unique characteristics of individual tall buildings. Building-specific collapse fragility curves of an existing tall building in Istanbul will be developed addressing the above research issues in the following chapters.

CHAPTER 3

STRUCTURAL DESIGN AND MODELING OF A 253 M TALL BUILDING IN ISTANBUL

3.1 Introduction

This chapter presents the building characteristics and performance-based structural design of a tall concrete core wall building with an outrigger system in Istanbul, which is used as the case study building in this study, develops the analytical models of the building and presents the selected strong earthquake ground motion records based on the previous probabilistic seismic hazard analysis carried out for the building site.

3.2 Building Characteristics

The building is a 253 m tall, 62-story RC office building, including eight podium floors below ground level, the ground (G) floor and 53 floors above ground level. The typical floor-to-floor height is 4.0 m, whereas the height of the ground story is 8.75 m and the total height of the podium stories is 31.75 m. It was completed in 2019 and is currently the sixth tallest building in Turkey and thirty-sixth in Europe [CTBUH 2022]. Figure 3.1 shows the view of the building from the northeast (NE) corner during its construction, the typical podium floor plan and the building section. The parallelogram footprint was necessitated due to the plan optimization based on the available land geometry, which causes additional torsional effects under lateral loading.

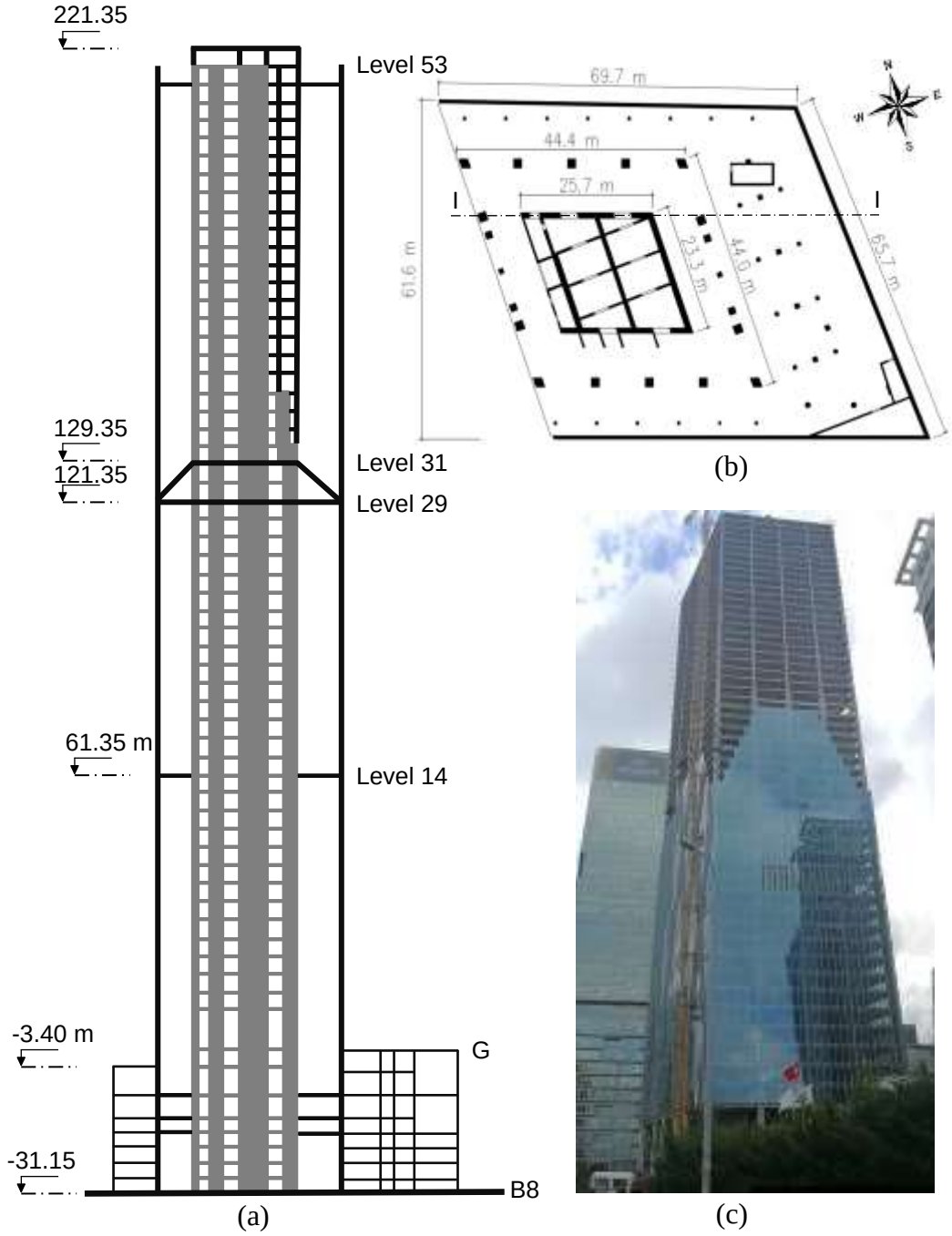

Figure 3.1 (a) Building section I-I, (b) typical podium floor plan and (c) construction view from the NE corner.

Typical floor plan of the tower is shown in Figure 3.2. The main segments of the core shear walls P1–P8 are 1.00 m thick, whereas P22 and P25 are 1.10 m thick, at the lower stories. Thicknesses gradually reduce in four stages to 0.60 m at the upper

stories. P24 is 0.80 m thick at the lower half of the tower and 0.60 m at the upper half. Other wall segments are 0.40 m thick throughout the height of the building. The ratio of the core shear wall area to the tower floor area varies from 3.6% at the building base to 2.0% at the building top along the N-S direction and from 2.8% to 1.6% along the E-W direction. 2.2 m long 0.85 m deep and 3.3 m long 1.12 m deep coupling beams exist in the E-W direction.

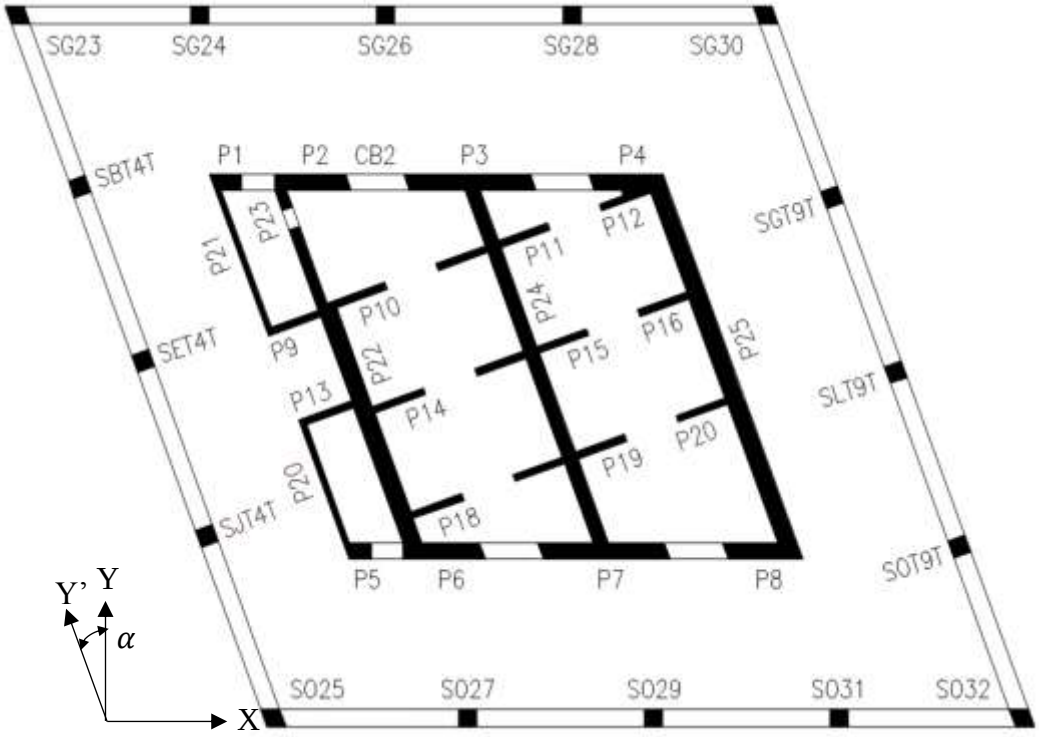

Figure 3.2 Building typical tower floor plan.

At the eight podium stories, square RC columns are 1.50–1.60 m in size under the tower except at the top podium story and 0.90 m elsewhere. Above the top podium floor level up to floor 27, square composite columns with encased HD 400 steel sections are 1.00–1.10 m in size, whereas square RC columns are 0.60–1.00 m in size at the upper stories. Table 3.1 presents the types and sizes of the square tower columns along the building height.

Table 3.1 Properties of square tower columns.

Level	Type	Dimension (m)
L48–Roof	RC	0.6
L40–L48	RC	0.7
L37–L40	RC	0.8
L32–L37	RC	0.9
L27–L32	RC	1.0
L2–L27	Composite	1.0
B1–L2	Composite	1.1
B5–B1	RC	1.5
B8–B5	RC	1.6

Three pairs of two-story tall diagonal RC outrigger braces in the N-S (Y) direction and two pairs of similar outriggers in the E-W (X) direction were incorporated between floors 29 and 31 (Figure 3.3) to reduce the interstory drifts and bending moments in the core wall under wind and earthquake effects. The outrigger members are 1.20 m deep and 0.75 m wide.

The tower floors are composed of 0.25 m thick conventional RC flat plates. Slab thickness at the upper podium level was selected as 0.40 m to control the backstay effects, and reduces to 0.30 m at the lower podium floors. The perimeter beams are 0.60 m deep and 1.00 m wide.

The building has a 4.8 m thick mat foundation under the tower, which gradually reduces to 3.5 m, 2.0 m and 1.5 m under the podium floors. It is located on stiff soil (Soil Group ZC [AFAD 2018a]), equivalent to NEHRP Type C [FEMA 2020], where the average shear wave velocity in the upper 30 m of the site profile, V_{s30}, is 500 m/s.

(a)

(b) (c)

Figure 3.3 (a) Isometric view of outrigger system, and (b) outriggers along X-direction and (c) Y-direction.

Concrete characteristic strength, f_{ck}, is 60 MPa at the core walls, coupling beams and tower columns, and 40 MPa at all other members. Characteristic yield strength of reinforcing steel, f_{yk}, is 420 MPa, whereas yield strength of structural steel, f_y, in composite members is 460 MPa.

3.3 Structural Design

Structural system selection and initial proportioning of structural members is a crucial stage in structural design. A core wall and peripheral columns connected with flat plates are adequate for resisting lateral loads for RC buildings that are up to 30

stories tall [Colaco 2005]. Previous studies on tall buildings indicated that the slenderness ratio of the core wall (the ratio of the building height to the smaller plan dimension of the core wall) should be between 8 and 10. If alternative structural systems are employed such as connecting the core to the peripheral columns with outriggers, this ratio may be increased to 12–18 in taller buildings [Colaco 2005; Arup Inc. 2013; Choi 2009]. This high aspect ratio can be alleviated by introducing outriggers [Choi and Joseph 2012]. The slenderness ratio of the core wall in this 253 m tall building is 11. For carrying the gravity loads and satisfying the architectural requirements, flat plate floor systems were preferred in the building.

Wind tunnel tests are used for predicting the design wind loads on tall buildings. Accurate determination of wind loads are particularly important for comfort criteria evaluations and cladding design. Wind tunnel tests were performed on a 1/400-scale model of the building and its proximity, as shown in in Figure 3.4 [ASCE 2012; WTG 1996; CEN 2005]. Peak horizontal acceleration at the top floor under service-level wind loads, associated with a mean recurrence interval of 10 years, was determined as 0.021 g for 2.5% damping, which is below the occupant comfort limit of 0.025 g for office buildings. Design wind load distributions on the building, components and cladding were determined for 5% damping for a mean recurrence interval of 50 years.

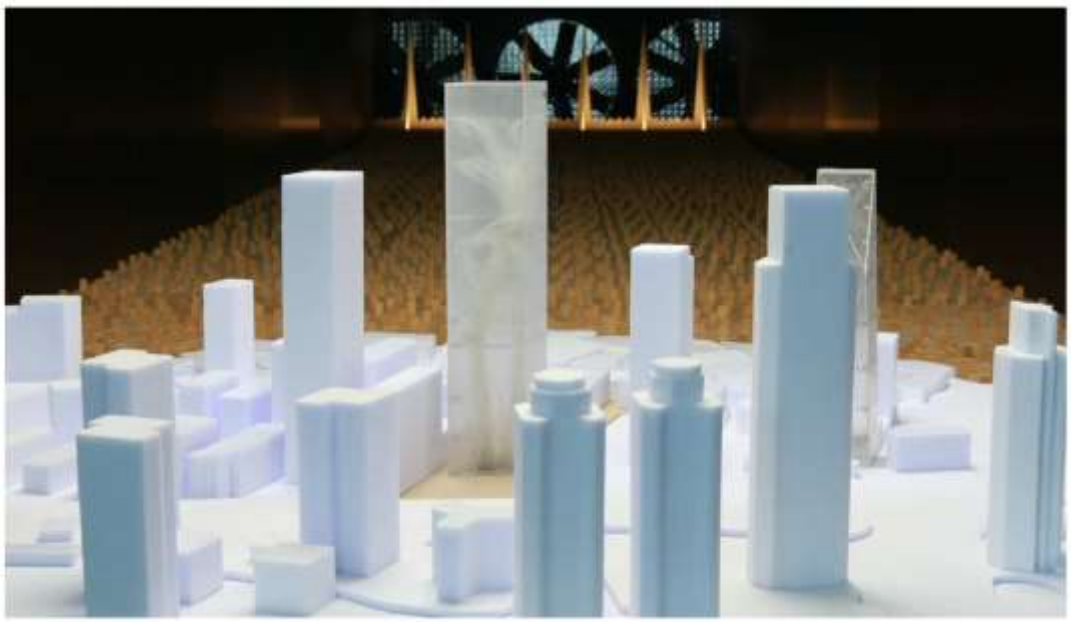

Figure 3.4 1/400-scale wind tunnel model of the building and its proximity.

Seismic design was based on state-of-the-art guidelines and practices prevailing during the planning stage of the project in 2016 [Budak et al. 2018] and was peer reviewed. Current practices employed in the seismic design of tall buildings are assessed in view of this building. Seismic performance evaluation in tall building design is carried out for two performance objectives: evaluation for serviceability performance under an earthquake with a return period of 43 years (defined as service-level earthquake; SLE) through a linear elastic response spectrum analysis, and evaluation for collapse prevention performance under the selected 2475-year earthquake (defined as MCE) ground motions through nonlinear response history analyses. The main factors considered during the design and seismic performance assessment of the building are the seismic load requirements, force/stress/reinforcement limitations imposed on different members, and the associated performance limits enforced under the SLE and MCE. Design is deemed satisfactory if all target performance objectives are met [AFAD 2018a; LATBSDC 2020; PEER 2017].

3.3.1 Design earthquake and seismic design approach

Structural design and detailing were based on response spectrum analysis under the SLE. Capacity shears were employed in the shear design of ductile members. The dominant design load combination that includes seismic action for the SLE is

$$D + 0.25L + E_h \tag{3.1}$$

where D is the dead load, L is the live load and E_h is the horizontal design earthquake load ($E_h = \pm E_X \pm 0.3\, E_Y$); E_X and E_Y are the earthquake actions obtained from response spectrum analysis along the X and Y directions, respectively.

3.3.2 Base shear force and axial load limits

Minimum base shear force is $V_b = 0.015W$ (W is the effective seismic weight of the building) according to the AFAD [2018a] although it is not mandated in the other design guidelines [LATBSDC 2020; PEER 2017]. Maximum permitted normalized compressive stresses acting on RC members are $N_d/A_c f_{ck} < 0.40$ for concrete columns and $N_d/A_c f_{ck} < 0.25$ for shear walls, where N_d is the axial load demand calculated under the design load combination in Eq. 3.1 and A_c is the gross area of the concrete cross section. These limits were set by the review team. For composite columns, the maximum value of the axial load is $N_d < 0.4N_{ro}$ when N_d is calculated from the $1.2D + L + E_h$ load combination [MPWS 2007], and is $N_d < 0.8N_r$ when N_d is calculated from the $1.4D + 1.6L$ combination [TSI 2000], where N_{ro} and N_r are the axial load capacities of the composite columns calculated using

$$N_{ro} = 0.85A_{co}f_{ck} + A_s f_{yk} + A_a f_y \tag{3.2}$$

$$N_r = 0.85A_{co}\, f_{ck}/1.5 + A_s\, f_{yk}/1.15 + A_a\, f_y/1.1 \tag{3.3}$$

where A_{co} is the net concrete area, A_s is the longitudinal reinforcement area and A_a is the area of the steel section.

3.3.3 Reinforcement limitations

Limitations on reinforcement are dictated by the existing design codes [MPWS 2007; TSI 2000; ACI 2014]. Longitudinal reinforcement ratio ρ for RC columns is $0.01 < \rho < 0.04$. For composite columns, the area of the steel section should exceed $\rho_s = 0.04$ times the gross section area. In the case of diagonal outrigger members, which are primarily subjected to axial forces, $\rho < 0.05$. This limit was set by the peer review team.

In the web region of shear walls, $\rho > 0.0025$ of the web cross-sectional area, whereas in the confined end regions of shear walls, $\rho > 0.0020$ of the total wall area within the critical height region and $\rho > 0.0010$ above the critical height.

For beams, the longitudinal tensile reinforcement ratio ρ should satisfy $0.6\, f_{ctk}/f_{yk} < \rho < 0.02$ as well as $\rho < 0.85\rho_b$. Here, f_{ctk} is the characteristic tensile strength of concrete and ρ_b is the balanced tensile reinforcement ratio.

Transverse (horizontal) reinforcement ratio ρ_v conforms to the enforced concrete design codes [MPWS 2007]. In the web region of shear walls, $\rho_v > 0.0025$ of the web cross-sectional area, whereas in the confined end regions of shear walls, the spacing of confinement reinforcement is between 50 and 100 mm along the critical height region, and less than 25 times the confinement reinforcement diameter above the critical height region.

Further detailing requirements are not repeated here as they are common in the existing design codes.

3.3.4 Flexural design

Design bending moments for columns, core walls and beams were determined from the response spectrum analysis under the load combination in Eq. 3.1. Design bending moment distributions for the core walls were modified to consider dynamic amplification [AFAD 2018a; Moehle et al. 2012] in order to ensure that plastic

hinging only occurs at the designated critical sections of the walls. Critical wall sections in this building, where maximum bending moments develop, are at the base of the ground story and above the podium floor.

3.3.5 Shear design

Design shear forces for beams and columns are the capacity shear forces, which are based on the flexural strength at the end sections. Design shear forces in core walls at any section were calculated as

$$V_e = \left(M_{p,t}/M_{d,t}\right)V_d \tag{3.4}$$

where $M_{p,t}$ is the moment capacity at the critical section of the core wall, and $M_{d,t}$ is the bending moment and V_d is the shear force calculated at the critical section under the SLE. However, these forces should not exceed $3.5V_d$. Critical wall height is 1/6 of the total wall height above the critical section [MPWS 2007].

3.4 Performance Objectives

3.4.1 Performance limits under SLE and wind

Core wall, column, outrigger and beam moment demand-to-capacity ratios (DCRs) for deformation-controlled actions should not exceed 1.5 under the design load combination given in Eq. 3.1. Similarly, shear DCRs of these members should not exceed 0.7 in order to suppress the shear mode of failure. Expected material strengths were employed for calculating the capacities, which are $1.3f_{ck}$, $1.17f_{yk}$ and $1.1f_y$ for concrete, reinforcing steel and structural steel, respectively [LATBSDC 2015]. With these limits, the objective is to have the structural members remain essentially elastic. Minor post-yield deformations are permitted for ductile structural elements.

IDR is limited to 0.5% under the SLE [PEER 2017; LATBSDC 2020] to ensure that the building remains essentially linear elastic. Furthermore, IDR is limited to 0.2% under 50-year wind load [Smith 2011; Arup Inc. 2013].

3.4.2 Performance limits under MCE

Mean maximum transient IDR obtained under the MCE ground motion ensemble and the maximum IDR under each ground motion in the ensemble are limited to 3.0% and 4.5%, respectively [PEER 2010; LATBSDC 2020]. The mean shear DCRs in all members should not exceed 1.0 under the MCE ground motions. Performance of the building is deemed satisfactory if the calculated compressive strains for confined concrete are less than 0.010 and reinforcing steel tensile strains are less than 0.030 for columns, core wall segments, beams and coupling beams [PEER 2010]. For outrigger components, strain limit for concrete in compression is 0.02, and 0.08 for steel in tension. With these limits, the objective is to prevent the collapse of the building. Limited damage in specified locations is permitted.

3.5 Analytical Models

In this section, both linear elastic and nonlinear finite element models of the building were developed for use in ambient vibration testing, seismic design and performance review, and seismic fragility analysis of the building presented subsequently.

3.5.1 Linear elastic finite element model

A 3-D linear elastic finite element structural model of the building was developed using ETABS [CSI 2020] as shown in Figure 3.5 to calculate the design forces and deformations under the load combination in Eq. 3.1 and to reproduce the in-situ natural vibration periods and mode shapes identified from temporary monitoring of the building. Thin shell elements were used for the shear wall and slab members,

whereas frame elements with rigid end offsets were used for the column and beam members, based on centerline dimensions. P-delta effects were considered in the analysis. The other modeling aspects of the linear elastic finite element model, such as cracked section properties and modulus of elasticity for concrete, will be explained in Chapter 4.

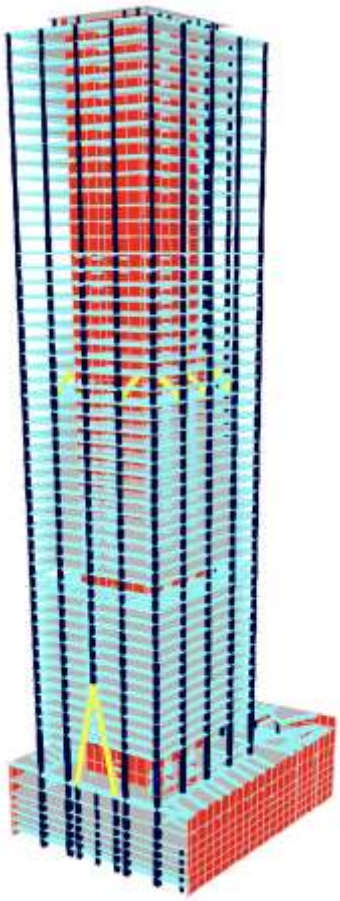

Figure 3.5 3-D finite element structural model of the building.

3.5.2 Nonlinear finite element model

Various parameters need to be considered when developing an appropriate nonlinear model. The degree of idealization, the types of structural members, the material properties, the component models, the dominant behavior that will be captured, the unknowns and uncertainties in inelastic behavior, the analysis objectives, the

demand parameters, the computer software that will be used, and the time and effort required for the analysis should all be considered [PEER 2010].

Nonlinear structural models can be mainly classified into three groups depending on the degree of idealization in the model. The term "degree of idealization" indicates where and how inelastic response is modeled in a member, such as integrated inelastic behavior of a member idealized at a point (lumped plasticity model) or a zone (fiber model) or distributed by a specific characteristic length over the entire length (continuum finite element model) [PEER 2010; NEHRP 2013].

The first type of nonlinear model is the continuum finite element model. The essential parameters of this model are the basic material properties and a characteristic finite mesh size. Depending on the idealization of the model, uniaxial, biaxial or triaxial material properties for concrete and reinforcing steel are employed. Continuum finite element models mesh a RC member with explicit longitudinal and transverse reinforcement over the entire cross-section.

The second type of nonlinear model is the fiber model, which may be defined as a simple form of the continuum finite element model. The modeling parameters of the fiber model are similar to the continuum finite element model but simpler. In fiber and continuum finite element models, expected inelastic behavior of the member is captured explicitly by the inelastic behavior of the material that constitutes the members. Whereas continuum finite element model is based on more complex material constitutive relationships, fiber model is based on simpler basic uniaxial material properties to capture the overall response of the structure. Fiber models divide cross section of the member into sufficient number of concrete and steel fibers by a simple way with characterized element length over the entire height. But using adequate number of fibers along the cross section and adequate number of elements over the length of the member is crucial to capture the overall member behavior [Budak and Sucuoglu 2016].

The last type of inelastic model is the concentrated hinge model based on the overall response of prismatic components. Concentrated hinge model consists of quasi-

elastic element implicitly accounting for concrete cracking, bond slip, etc. with concentrated plastic hinges where they represent the integrated effects of distributed inelastic response.

The 3-D simulation of the nonlinear behavior of a tall building is a hard task, which needs explicit solution techniques. There is very few commercial software to simulate 3-D nonlinear dynamic analysis of tall buildings. On the other hand, the capability of these software is also limited (e.g., idealized multi-piece linear moment-curvature was used for beams, shear-flexural interaction was ignored). In addition, the simplified 2-D models of tall buildings such as planar systems are not appropriate to simulate possible assessment of tall buildings.

Fiber-type shell elements and lumped plasticity models are commonly employed for shear wall members and frame type members, respectively, responding beyond the linear elastic range [PEER 2010; Wallace 2007; Zekioglu et al. 2007]. There are two main reasons of using concentrated hinge model for frame members. First, it is not practical to use fiber models in the modeling of frame members due to excessive computational demand (time and capacity). Second, current analytical models and acceptance criteria that are specified in codes for frame type members are based on lumped plasticity (concentrated hinge) models. On the other hand, fiber models can be generally used for shear wall elements. The main reason using fiber model for shear wall elements is that this modeling approach represents the behavior of shear walls more accurately than other approaches [PEER 2010].

A 3-D nonlinear finite element structural model of the building was developed using Perform3D [CSI 2020] to calculate the inelastic design forces and deformations under the load combination in Eq. 3.1. Nonlinear modeling of all structural members will be presented in the following.

3.5.2.1 Nonlinear modeling of shear walls

Fiber-type shell elements, which are displacement-based four node macro elements with three translational and three rotational degrees of freedom per node, were used for modeling the shear walls [Lowes et al. 2016]. This model formulation compounds three response models: (1) a fiber type section model, which consists of idealized multi-linear inelastic concrete and steel fibers, simulating the in-plane flexural response, (2) a uniform shear layer, with a 1-D linear or nonlinear shear response model, simulating the in-plane shear response and (3) a uniform linear elastic plate bending model simulating the out-of-plane response.

In fiber-type shell element model, stiffness, strength and deformation response parameters of the members under gravity and dynamic loads are derived from directly material stress-strain relationships. Hence, efficient and reliable hysteresis material models are required to model shear wall members. In literature, various studies have been employed on the modeling of concrete and steel material models from the simple and efficient to quite sophisticated and complicated models. The studies in this area are quite widespread but the scope of material models in this study is limited to uniaxial material stress-strain relationship for fiber models and its implementations in the current commercial software for the buildings.

Confined and unconfined concrete material models

In fiber models, a shear wall member consists of a number of wall elements, and each wall element consists of a number of steel and confined and unconfined concrete fibers (see Figure 3.6). The fiber-type section is utilized to simulate the nonlinear flexural response of the wall cross section. Uniaxial material stress-strain relationship is assigned to each fiber to simulate the flexural response of the wall under gravity and dynamic loadings.

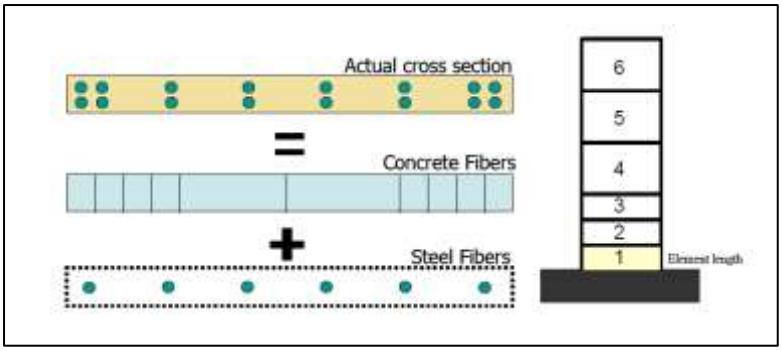

Figure 3.6 Idealized cross section for fiber model and elevation of shear.

Figure 3.7 presents the backbone curve for the idealized multi-linear action-deformation material response in Perform3D, called as "YULRX". The aim of this backbone action-deformation relationship, with points Y, U, L, R and X is to capture the fundamental properties of the behavior namely the initial stiffness, strain hardening, ultimate strength and strength loss, where Y is the first yield point, U is the ultimate strength point, L is the ductile limit point, R is the residual strength point and X is a deformation point for terminating the analysis. The idealized material stress-strain relationships can have either an elastic-perfectly plastic or multi-linear piece, with optional strength loss. The hysteresis loop for the inelastic material varies to account for stiffness degradation. Almost all of the nonlinear components use this backbone curve in the software.

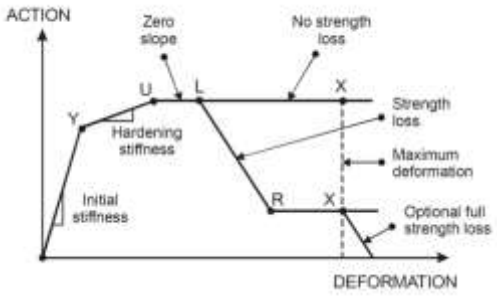

Figure 3.7 Typical action-deformation material response model in Perform3D [CSI 2020].

Previous studies show that the use of typical concrete material models (e.g., Mander et al. [1988]; Saatcioglu et al. [1998]) in modeling shear walls lead to inaccurate

simulation of cyclic responses and drift capacities when compared with the experimental counterparts [Pugh et al. 2015; Lowes et al. 2016]. Hence, regularized concrete material response, modifying post peak stress-strain response based on concrete fracture energy, developed by these researchers, was used for the fiber-type shell elements in order to capture the cyclic responses and drift capacities accurately. Moreover, using a simplified confined concrete model for wall boundaries and unconfined concrete models for wall web is sufficient in order to predict building behavior more rational under cycling loading when comparing test results [PEER 2010; Budak and Sucuoglu 2016]. Table 3.2 lists the stress and strain values used to define the YULRX backbone curve for confined and unconfined concrete in compression response, where f'_{cc} and f'_c are confined and unconfined concrete strength, respectively, ε_{occ} and ε_o are the compressive strain at maximum confined and unconfined concrete strength defined by Saatcioglu et al. [1998]. ε_R and ε_{Rcc} obtained in Eqs. 3.5 and 3.6 are the strain at crushing point for unconfined and confined concrete, respectively, where E_c is the concrete elastic modulus, G_{fcc}, G_{fc} are the confined and unconfined concrete crushing energy found in Eqs. 3.7 and 3.8 and h_{elem} is the height of the wall element. Idealized multi-linear confined concrete for shear walls boundaries and unconfined concrete for shear walls web in accordance with the regularized material models were used in the modeling of the shear wall members. Figure 3.8a presents comparison typical modeling confined and unconfined concrete material with regularized concrete model with respect to concrete fracture energy [Lowes et al. 2016].

Table 3.2 Properties of confined and unconfined concrete stress-strain material model parameters in compression.

	FY	FU	FR/FU	DL	DR	DX
Unconfined C.	$0.75f'_c$	f'_c	$0.85\varepsilon_o$	$1.15\varepsilon_o$	ε_R	$1.15\varepsilon_R$
Confined C.	$0.75f'_{cc}$	f'_{cc}	$0.85\varepsilon_{occ}$	$1.15\varepsilon_{occ}$	ε_{Rcc}	$1.15\varepsilon_{Rcc}$

$$\varepsilon_R = \varepsilon_o - \frac{f_c'}{E_c} + \frac{2G_{fc}}{f_c' \times h_{elem}} \tag{3.5}$$

$$\varepsilon_{Rcc} = \varepsilon_{occ} - \frac{0.8f_{cc}'}{E_c} + \frac{10G_{fcc}}{3h_{elem} \times f_c'} \tag{3.6}$$

$$G_{fc} = 87.6\frac{\text{N}}{\text{mm}} \tag{3.7}$$

$$G_{fcc} = 87.6 < 2.5\left(\frac{f_{cc}'}{f_c'} - 0.85\right) < 220\frac{\text{N}}{\text{mm}} \tag{3.8}$$

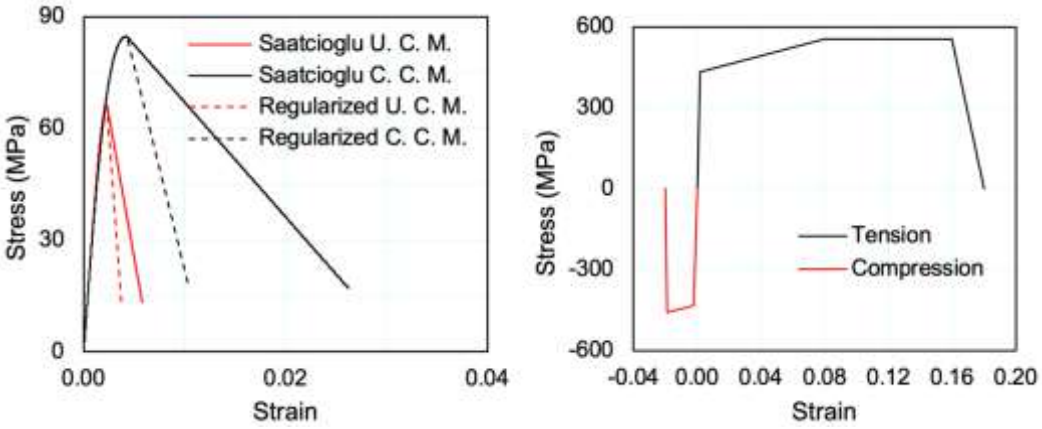

(a) (b)

Figure 3.8 (a) Comparison of the response of the concrete material response (b) typical reinforcing steel material response.

Perform3D allows users to calibrate the concrete cyclic response history in compression. Table 3.3 provides proposed energy dissipation values for concrete material states. The results show that the proposed model provides a good representation of the measured strain at onset of reloading and reloading stiffness [Lowes et al. 2016]. In addition, the tensile strength of concrete is neglected.

Table 3.3 Concrete energy dissipation factors.

Material State	Y (Yield)	U (Ultimate)	L (Loss)	R (Residual)	X (Rupture)
Energy Factor	1.0	0.4	0.4	0.1	0.1

Reinforcing steel material model

Idealized multi-linear inelastic steel material model is employed to model reinforcement steel [Lowes et al. 2016]. Similar to concrete models, a single YULRX monotonic stress-strain relationship was used to define the envelope stress-strain in tension and compression for reinforcement steel, presented in Figure 3.8b. 1.0% strain hardening was assumed. The simple buckling model proposed by Pugh et al. [2015] and Lowes et al. [2016] for use in simulation of wall response was employed. This model assumes that when concrete has reached residual compressive strength, there is minimal restraint of bar buckling and reinforcing steel loses compressive capacity.

Perform3D software allows users to calibrate the reinforcing steel cyclic response history in tension and compression. For reinforcing steel material, unloading and reloading stiffnesses are defined by the energy dissipation factor and the stiffness factor. The energy dissipation factor defines the extent to which stiffness loss reduces energy dissipation; it equals the ratio of the energy dissipated during a stress-strain cycle for the material with stiffness loss to the energy dissipated without stiffness loss. Table 3.4 provides proposed energy dissipation values for reinforcing steel material states. The results show that the proposed model provides a good representation of the measured strain at onset of reloading and reloading stiffness [Lowes et al. 2016].

Table 3.4 Reinforcing steel energy dissipation factors.

Material State	Y (Yield)	U (Ultimate)	L (Loss)	R (Residual)	X (Rupture)	Stiffness F.
Energy Factor	0.75	0.75	0.75	0.75	0.75	0.50

Mesh refinement

A single shear wall element, presented in 2.6 simulates constant curvature, and so a linear vertical strain distribution, along the in-plan length of the wall. However, the studies show that the actual vertical strain distribution in a planar wall to be nonlinear when nonlinear action occurs. Based on the studies carried out by Lowes et al. [2016] minimum four shear wall elements should be used along the length of the wall with minimum one element used to model each boundary element and minimum two elements used for the interior web region. Similarly, a single shear wall element simulates a constant vertical strain over the height of the element. However, if recommendations proposed in the new modeling techniques is employed, vertical mesh size does not affect to determine simulated deformation capacity. In this study, these proposed suggestions, presented above, are considered when nonlinear modeling of shear wall in this study.

3.5.2.2 Nonlinear modeling of coupling beams and peripheral beams

RC coupling beams can be modeled as either fiber model or lumped plasticity model with slip extension or lumped plasticity or shear displacement hinge model. Current analytical models and acceptance criteria that are specified in codes and related documents for coupling beams are based on rigid plasticity model or shear displacement hinge model [Naish et al. 2009].

In this study, conventional coupling beams were utilized in the design stage. Nonlinear validation of nonlinear modeling of coupling beams was carried out according to Naish et al. [2009]. For validation of the modeling of coupling beams, two different nonlinear models were generated using the properties of the FB33 test specimen were given in Naish et al. [2009]. In the first model, idealized multi-piece linear moment curvature relationship was defined according to FEMA-356. In addition, plastic hinge length was assumed as one half of the section depth. The yield and plastic rotation of the section are determined by using the equations:

$$\theta_y = \frac{M_y}{EI_{ef}} \times l_p \tag{3.9}$$

$$\theta_p = \left(\emptyset_i - \emptyset_y\right) \times l_p \tag{3.10}$$

Where θ_y is yield rotation, $M_y$is yield moment, EI_{ef} is effective flexural stiffness, l_p is plastic hinge length, $\emptyset_y$ is idealized yield curvature and $\emptyset_i$ is plastic curvature. In the second model, idealized multi-piece linear moment-rotation plastic hinges was defined, where moment force obtained from idealized moment-curvature relationship (section analysis), illustrated in Figure 3.9a, and plastic rotation values of the section were directly taken from test report. Figures 3.9a and 3.9b present the idealized moment curvature relationship and the comparison of developed analytical model results with test results, respectively. The calibration parameters (strength loss interaction parameter, the factors related to hysteresis loop and unloading stiffness factor) are presented in Figure 3.10. The results show that both models give close to each other and give reasonable results. Idealized multi-piece moment curvature hinge are utilized in modeling of the building based on these results. Nonlinear modeling of peripheral beams is also performed similar to coupling beams.

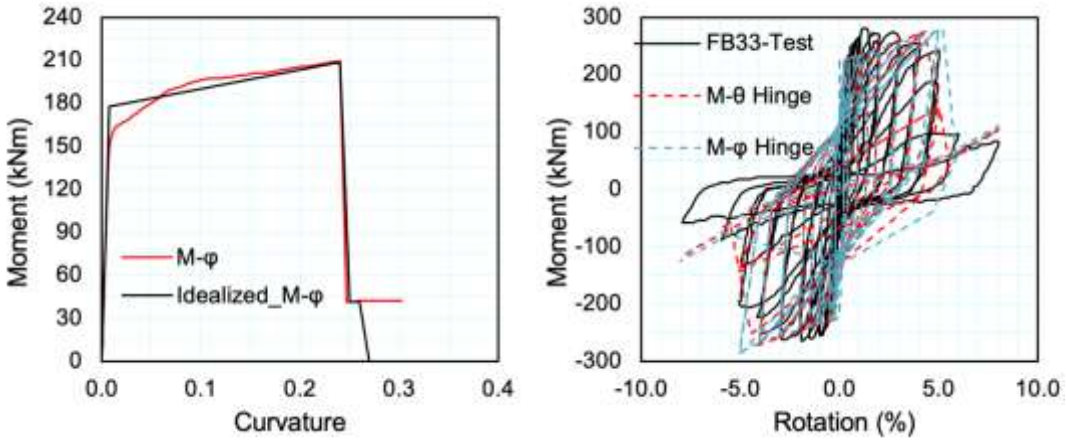

(3) (b)

Figure 3.9 Idealized moment-curvature and (b) comparison of test result with the analytical moment curvature and rotation hinge results in Perform3D.

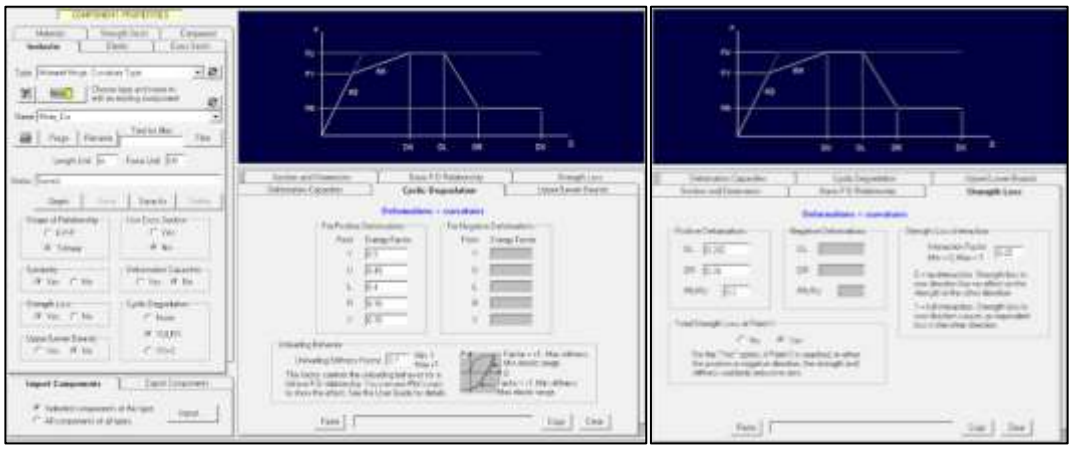

Figure 3.10 Strength loss interaction factor and hysteresis parameters of coupling beams in Perform3D.

For calculating the effective flexural stiffness of quasi-elastic sections, gross section properties were reduced by effective section stiffness multipliers for the SLE loading: 0.2 for coupling beams and 0.7 for the peripheral beams and for the MCE loading: 0.15 for coupling beams and 0.35 for the peripheral beams. Shear deformation is ignored [Naish et al. 2009].

3.5.2.3 Nonlinear modeling of diagonal outrigger members

The diagonal outrigger members are tension-compression members; hence, the nonlinear model of diagonal outrigger members is idealized by a concrete strut in compression and by a steel bar in tension. Idealized material backbone curves of outrigger members in compression and tension are presented in Figures 3.11 and 3.12.

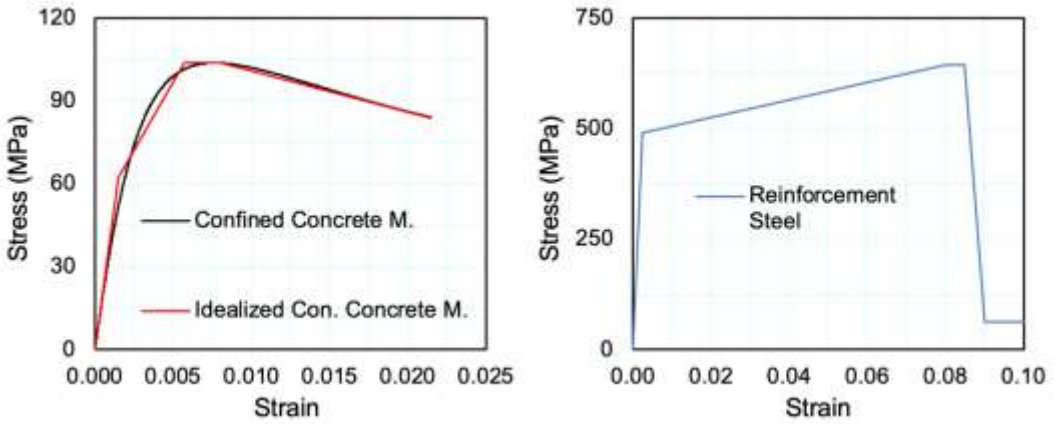

(3) (b)

Figure 3.11 (a) Confined concrete (b) reinforcement steel stress-strain properties of outrigger member materials.

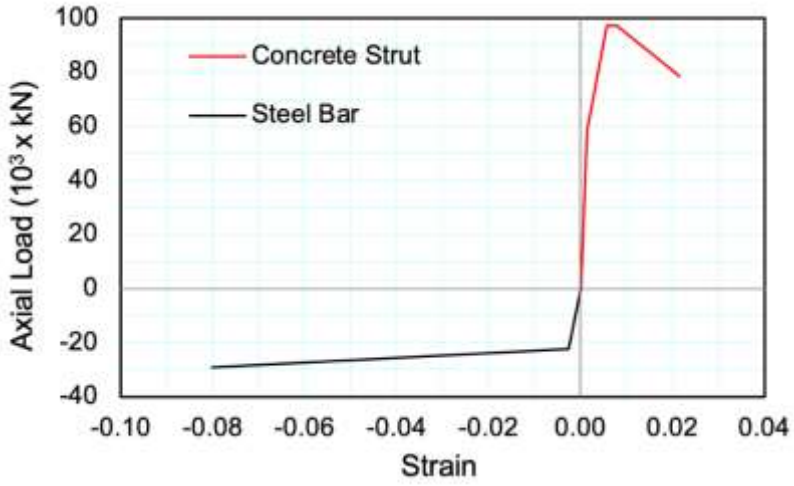

Figure 3.12 The Idealized force deformation relationship concrete strut and steel bar.

3.5.2.4 Nonlinear modeling of columns

Column frame members are modeled with the 3-D interaction (yield) surface of P-M2-M3 hinges with considering biaxial bending and axial force [El-Tawil and Deierlein 2001a; 2001b]. No strength deterioration model is utilized. In this regard, plastic hinge lengths which are assumed as one half of the section depth are defined

at both ends of all columns. For calculating the effective flexural stiffness of quasi-elastic sections, gross section properties are reduced by effective section stiffness multipliers for the SLE and MCE loading: 0.9 and 0.7, respectively. Shear rigidity is taken as GA and G is taken as 0.4E.

3.6 Probabilistic Seismic Hazard Analysis and Strong Ground Motions

A site-specific probabilistic seismic hazard analysis (PSHA) was performed to develop the response spectra for hazard levels of 50% probability of exceedance (PE) in 30 years, 10% PE in 50 years and 2% PE in 50 years, which respectively correspond to mean recurrence intervals of 43, 475 and 2475 years, i.e. the SLE, the design basis earthquake (DBE) and the MCE. The PSHA methodology relies on the historical and recorded seismicity as well as neotectonics faulting structure of the Istanbul region and ground motion modeling [Akkar 2014].

Figure 3.13 presents the $\xi = 2.5\%$ damped site-specific acceleration response spectrum for the SLE and 5% damped spectra for the DBE and MCE hazard levels. Viscous damping ratio is taken as 2.5% rather than the conventional 5% in obtaining the SLE spectrum, because very limited concrete cracking is expected under the SLE excitation [PEER 2017]. The SLE, DBE and MCE spectra are employed as target spectra in selecting and scaling the SLE, DBE and MCE ground motion pairs, respectively.

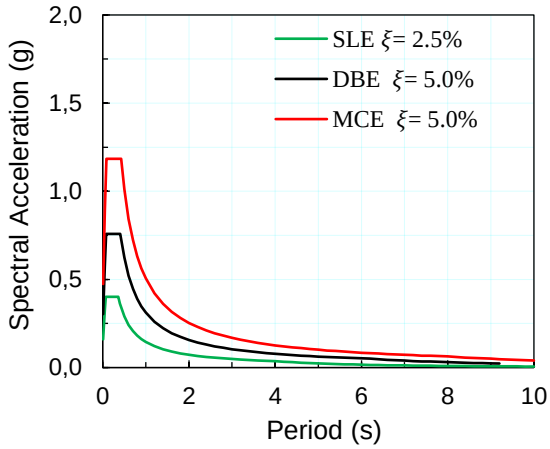

Figure 3.13 Site-specific SLE, DBE and MCE response spectra.

Four different ground motion record sets were selected and scaled for the performance evaluation and seismic fragility analysis of the building. The first strong ground motion record set, referred to as set #1 hereafter, were selected and scaled for the MCE hazard level [ASCE 2017a; Akkar 2014]. This ground motion set, which consists of seven ground motion pairs, was utilized to evaluate the collapse prevention performance level of the building under MCE ground motions during the design stage of the building. The second, third and fourth ground motion record sets, referred to as set #2, set #3 and set #4, respectively, were selected and scaled for the MCE, DBE and SLE hazard levels, respectively, for use in deriving seismic fragility curves. Sets #2 and #3 consist of 18 ground motion pairs and set #4 consists of 30 ground motion pairs.

Deaggregation for the MCE hazard yielded the earthquakes that contribute most significantly as moment magnitude (M_w) 7.5 earthquakes occurring at epicentral distances (R_{JB}) 26–49 km. Accordingly, the ground motions were selected from the PEER NGA Database [PEER 2022] with the following constraints pertaining to the construction site: $6.0 \leq M_w \leq 8.0$, $0\ \text{km} \leq R_{JB} \leq 50\ \text{km}$, and $300\ \text{m/s} \leq V_{s30} \leq 700\ \text{m/s}$. Then, ground motion amplitude scaling was carried out according to ASCE 7-16 [ASCE 2017a]. The seismological properties and scale factors (SFs) of the ground motion sets #1, #2, #3 and #4 are given in Tables 3.5–3.8, respectively. Selected ground motion pairs of set #2 were also used for set #3 by using different

SFs. Figures 3.14a and 3.14b present the response spectra of near fault ground motions in sets #1 and #2 that were scaled to match the target MCE spectrum. Figure 3.14c and 3.14d present the response spectra of ground motions in sets #3 and #4 that were scaled to match the target DBE and SLE spectra, respectively.

Table 3.5 Selected acceleration records, their seismological features and scale factors for set #1.

#	Event	Record	Station	M_w	R_{JB} (km)	V_{s30} (m/s)	SF
1	Imperial Valley 1979	RSN0164	Cerro Prieto	6.5	15.2	660	6.38
2	Landers 1992	RSN0838	Barstow	7.3	34.9	371	2.19
3	Landers 1992	RSN0900	Yermo Fire Station	7.3	23.6	354	1.89
4	Gulf of Aqaba 1995	RSN1144	Eilat	7.2	43.3	356	9.75
5	Kocaeli 1999	RSN1164	Istanbul	7.5	49.7	425	3.25
6	Duzce 1999	RSN1619	Mudurnu	7.1	34.3	660	4.06
7	Sitka, Alaska 1972	RSN1626	Sitka Observatory	7.7	34.6	660	7.22

Table 3.6 Selected acceleration records, their seismological features and scale factors for set #2.

#	Event	Record	Station	M_w	R_{JB} (km)	V_{s30} (m/s)	SF
1	Landers 1992	RSN0838	Barstow	7.3	15.2	660	2.19
2	Kocaeli 1999	RSN1164	Istanbul	7.5	49.7	425	3.25
3	Landers 1992	RSN0900	Yermo Fire Station	7.3	23.6	354	1.89
4	Chi-Chi 1999	RSN1534	TCU107	7.6	16.0	409	1.11
5	Chi-Chi 1999	RSN1535	TCU109	7.6	13.1	535	0.90
6	Chi-Chi 1999	RSN1541	TCU116	7.6	12.4	493	1.26
7	Chi-Chi 1999	RSN1545	TCU120	7.6	7.4	459	1.25
8	Chi-Chi 1999	RSN1546	TCU122	7.6	9.3	476	1.21
9	Chi-Chi 1999	RSN1549	TCU129	7.6	1.8	511	1.20
10	Chi-Chi 1999	RSN1551	TCU138	7.6	9.8	653	1.32
11	Duzce 1999	RSN1611	Lamont 1058	7.1	0.2	529	3.03
12	Hector Mine 1999	RSN1762	Amboy	7.1	41.8	383	1.68
13	Chi-Chi 1999	RSN2704	CHY029	6.2	25.8	545	2.99
14	Chi-Chi 1999	RSN2708	CHY034	6.2	28.5	379	3.68
15	Chi-Chi 1999	RSN2888	TCU116	6.2	28.7	493	3.23
16	Chi-Chi 1999	RSN2893	TCU122	6.2	23.1	476	3.94
17	Cape Mendocino 1992	RSN3750	Loleta Fire Station	7.0	23.5	516	1.66
18	Chuetsu-oki 2007	RSN4848	Joetsu Ogataku	6.8	16.8	414	1.99

Table 3.7 Selected acceleration records, their seismological features and scale factors for set #3.

#	Event	Record	Station	M_w	R_{JB} (km)	V_{s30} (m/s)	SF
1	Landers 1992	RSN0838	Barstow	7.3	15.2	660	1.48
2	Kocaeli 1999	RSN1164	Istanbul	7.5	49.7	425	2.08
3	Landers 1992	RSN0900	Yermo Fire Station	7.3	23.6	354	1.21
4	Chi-Chi 1999	RSN1534	TCU107	7.6	16.0	409	0.72
5	Chi-Chi 1999	RSN1535	TCU109	7.6	13.1	535	0.58
6	Chi-Chi 1999	RSN1541	TCU116	7.6	12.4	493	0.81
7	Chi-Chi 1999	RSN1545	TCU120	7.6	7.4	459	0.80
8	Chi-Chi 1999	RSN1546	TCU122	7.6	9.3	476	0.77
9	Chi-Chi 1999	RSN1549	TCU129	7.6	1.8	511	0.77
10	Chi-Chi 1999	RSN1551	TCU138	7.6	9.8	653	0.84
11	Duzce 1999	RSN1611	Lamont 1058	7.1	0.2	529	1.94
12	Hector Mine 1999	RSN1762	Amboy	7.1	41.8	383	1.08
13	Chi-Chi 1999	RSN2704	CHY029	6.2	25.8	545	1.92
14	Chi-Chi 1999	RSN2708	CHY034	6.2	28.5	379	2.36
15	Chi-Chi 1999	RSN2888	TCU116	6.2	28.7	493	2.07
16	Chi-Chi 1999	RSN2893	TCU122	6.2	23.1	476	2.52
17	Cape Mendocino 1992	RSN3750	Loleta Fire Station	7.0	23.5	516	1.06
18	Chuetsu-oki 2007	RSN4848	Joetsu Ogataku	6.8	16.8	414	1.27

Table 3.8 Selected acceleration records, their seismological features and scale factors for set #4.

#	Event	Record	Station	M_w	R_{JB} (km)	V_{s30} (m/s)	SF
1	Duzce 1999	RSN1611	Lamont 1058	7.14	0.2	529	1.01
2	Duzce 1999	RSN1614	Lamont 1061	7.14	11.5	481	1.97
3	Duzce 1999	RSN1616	Lamont 362	7.14	23.4	517	1.97
4	Duzce 1999	RSN1618	Lamont 531	7.14	8.0	638	1.95
5	Sitka Alaska 1972	RSN1626	Sitka Observatory	7.68	34.6	650	1.99
6	Hector Mine 1999	RSN1794	Joshua Tree	7.13	31.1	379	0.65
7	Hector Mine 1999	RSN1795	Joshua T. N. M.K.	7.13	50.4	686	1.93
8	Hector Mine 1999	RSN1836	Twenty nine Palms	7.13	42.1	635	1.94
9	Denali Alaska 2002	RSN2107	Carlo (temp)	7.90	49.9	399	1.25
10	Chi-Chi 1999	RSN2704	CHY029	6.20	25.8	545	0.64
11	Chi-Chi 1999	RSN2708	CHY034	6.20	28.5	379	0.77
12	Chi-Chi 1999	RSN2712	CHY042	6.20	34.1	665	1.47
13	Chi-Chi 1999	RSN2739	CHY080	6.20	12.4	496	0.84
14	Chi-Chi 1999	RSN2742	CHY086	6.20	33.6	665	1.40
15	Chi-Chi 1999	RSN2865	TCU061	6.20	56.7	380	1.53
16	Chi-Chi 1999	RSN2888	TCU116	6.20	28.7	493	0.68
17	Chi-Chi 1999	RSN2892	TCU120	6.20	38.3	459	0.87
18	Chi-Chi 1999	RSN2917	TTN023	6.20	57.4	528	1.97
19	Chi-Chi 1999	RSN3854	CHY010	6.20	31.6	539	1.34
20	Tottori 2000	RSN3943	SMN015	6.61	9.1	617	0.75
21	Bam 2003	RSN4054	M. A. Madkoon	6.60	46.2	575	1.25
22	Parkfield-02 2004	RSN4141	Parkfield U05	6.00	9.1	441	1.26
23	Parkfield-02 2004	RSN4142	PARKFIELD U06	6.00	9.1	441	1.42
24	Parkfield-02 2004	RSN4144	PARKFIELD U08	6.00	8.9	441	1.48
25	Parkfield-02 2004	RSN4148	PARKFIELD U12	6.00	9.0	466	1.30
26	Parkfield-02 2004	RSN4149	PARKFIELD U13	6.00	9.0	466	1.11
27	El Mayor-Cucapah 2010	RSN5842	Anza Borrego S.P.	7.20	57.9	585	1.80
28	Darfield 2010	RSN6891	CSHS	7.00	43.6	638	1.11
29	Darfield 2010	RSN6948	OXZ	7.00	30.6	482	1.42
30	Darfield 2010	RSN6971	SPFS	7.00	29.9	390	0.60

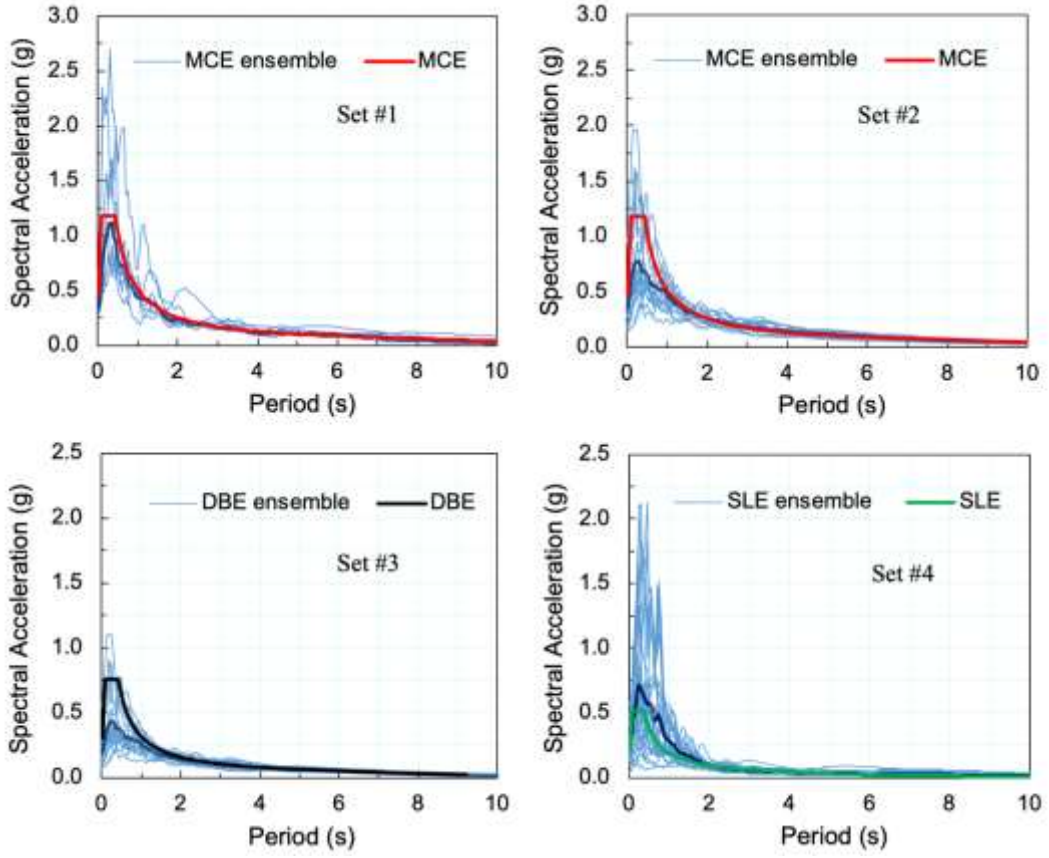

Figure 3.14 Acceleration response spectra of ground motions scaled to (a) the MCE response spectrum for set #1, (b) the MCE response spectrum for set #2, (c) the DBE response spectrum for set #3 and (d) the SLE response spectrum for set #4.

3.7 Summary

Structural system of the case study building was introduced. Performance-based structural design was presented with reference to the requirements of the design guidelines at the time. 3-D linear elastic and nonlinear finite element models of the building were developed. Strong earthquake ground motion record sets were selected for seismic performance review and fragility analysis in subsequent chapters.

CHAPTER 4

TEMPORARY MONITORING OF THE BUILDING

4.1 Introduction

Performance-based design guidelines that have been developed for tall buildings in recent years define two seismic performance objectives. Tall buildings are expected to meet the serviceability performance level when subjected to frequent earthquake ground motions and the collapse prevention performance level when subjected to very rare earthquake ground motions [LATBSDC 2020; AFAD 2018a]. Both performance evaluations call for reliable 3-D dynamic response analysis. It is imperative to simulate the dynamic properties of the structural system accurately. In-situ dynamic testing and structural health monitoring (SHM) help accumulate knowledge on dynamic properties of different structural systems used in tall buildings [Kijewski et al. 2006, Celebi et al. 2013]. Knowing the dynamic properties sheds light on finite element modeling (FEM) of these structural systems. In this regard, a unique opportunity has arisen to perform a dynamic test on the case study building. The identified dynamic properties for the building are valid for low-amplitude shaking as building vibrations were recorded during ambient conditions. They serve as baseline properties and can be used in validating the linear elastic structural model for service-level evaluations. Building response records under strong earthquakes are needed for validating the evaluations under high-amplitude shaking. For this purpose, real-time monitoring of the structural response of buildings of earthquake design class 1 and 2 in Turkey (i.e., design earthquake spectral acceleration parameter at short periods, $S_{DS} \geq 0.50$) that are taller than 105 m is now made mandatory by the new TBEC [AFAD 2018a]. This testing campaign albeit a temporary monitoring study was used in developing the SHM guidelines for tall buildings in Turkey [AFAD 2020].

In the finite element models that are developed to simulate the behavior of buildings under prescribed wind and earthquake loads in design provisions, damping ratios are required as input since damping cannot be computed directly from structural material properties. Under wind loads, damping ratios are taken as 1–1.5% for serviceability and 1.5–2% for strength limit states in RC building design [PEER 2010]. Under earthquake loads, LATBSDC [2020] recommends damping ratios not to exceed

$$\zeta = 0.20/\sqrt{H} \tag{4.1}$$

where H is the roof height above grade (in m), which gives 1.3% for the test building in this study, for service-level evaluations. Equation 4.1 can be also used for collapse-level evaluations but damping ratios are recommended to be taken at least 2.5%. Hence, the dependency of damping on the response amplitude [Celik and Gulkan 2021b] is implemented in the current design provisions. Damping in tall buildings is apparently less than those in low-rise buildings [PEER 2010; Bernal et al. 2015; Cruz and Miranda 2017].

This chapter presents the temporary monitoring scheme of the building, identification of its dynamic characteristics, including damping properties for service loads, from the recorded ambient vibration responses, comparisons of in-situ natural vibration periods and mode shapes with those from its finite element structural model developed, and the simulated floor accelerations when subjected to the 2019 M_w 5.8 Marmara Sea earthquake ground motions. FEM also provides insight into the dynamic properties for the service-level and design-level states of the building prescribed in design provisions. Crucial damping ratio statistics are provided for service-level evaluations.

4.2 SHM system

The authorization for testing the building was for a duration of five days. During this tight schedule, the building was extensively instrumented with two SHM systems consisting of 92 channels of accelerometers deployed on 20 different floors as shown

in Figure 4.1. Table 4.1 provides the accelerometer/channel numbering. Exact locations of the accelerometers marked on structural drawings are given in Appendix A. This instrumentation scheme places this building among one of the most densely instrumented buildings [Todorovska et al. 2020].

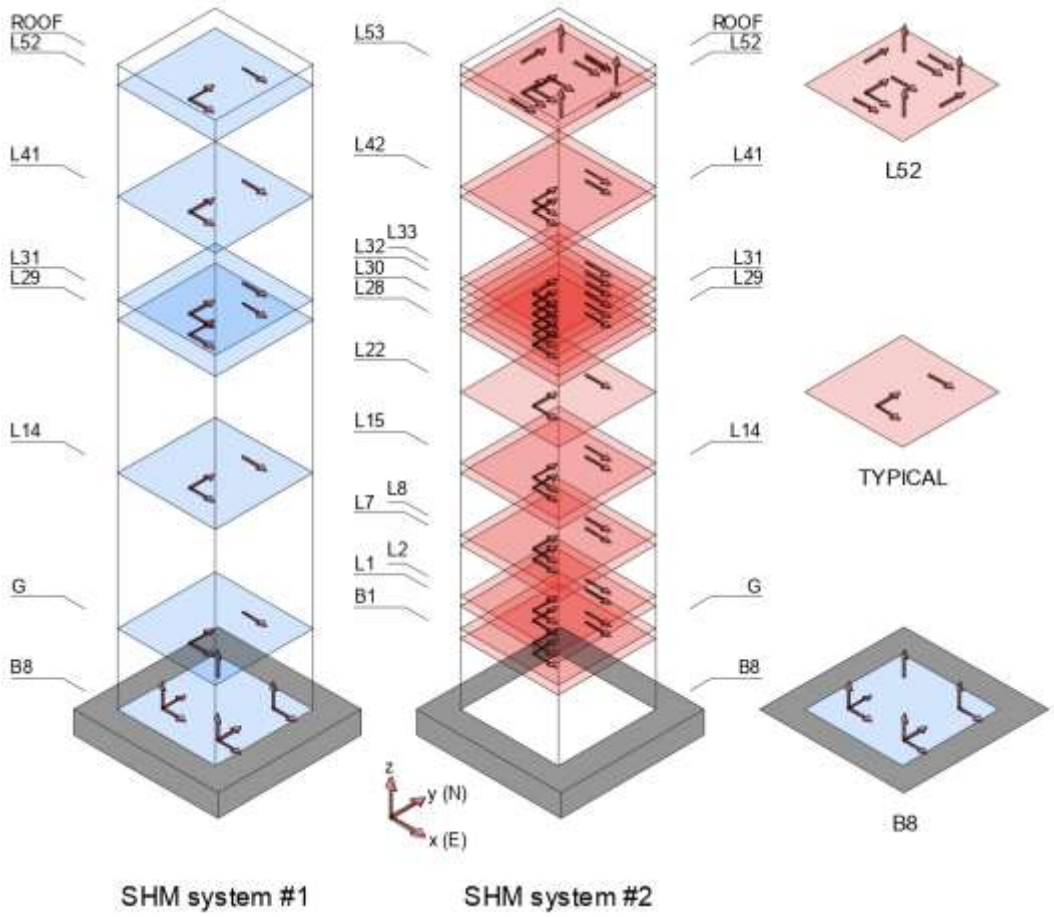

Figure 4.1 Instrumentation scheme.

SHM system #1 consisted of 24 uniaxial accelerometers and one triaxial accelerometer (all 24-bit force balance type with a bandwidth of DC to 200 Hz) [Sara, 2022], eight three-channel digital recorders (24-bit) [Sara 2022], one time-synchronization unit (i.e., network time protocol (NTP) server) and one GPS antenna. Accelerometers were placed on seven different floors: L52 (level 52), L41, L31, L29, L14, G (ground) and B8 (basement 8). Two uniaxial accelerometers parallel in the E-W direction and one in the N-S direction were placed around the

edges of the building core on each of these floors except floor B8; this three-accelerometer scheme on a single floor is the typical floor instrumentation. Floor B8 was instrumented by one triaxial accelerometer at one corner, three uniaxial accelerometers, one in the E-W, one in the N-S and one in the vertical directions, at another corner, two uniaxial accelerometers, one in the E-W and one in the vertical directions, at a third corner, and one uniaxial accelerometer in the vertical direction at a fourth corner, as illustrated in Figure 4.2a. This instrumentation scheme enables

Table 4.1 Accelerometer/channel numbering.

		SHM system #1			SHM system #2		
		Direction			Direction		
Floor	Elevation (m)	x (E)	y (N)	z	x (E)	y (N)	z
L53	217.35				G1, G3	G2	
L52	213.35	S1, S3	S2		G4, G6–9	G5, G10–11	G12–14
L42	173.35				G15, G17	G16	
L41	169.35	S4, S6	S5		G18, G20	G19	
L33	137.35				G21, G23	G22	
L32	133.35				G24, G26	G25	
L31	129.35	S7, S9	S8		G27, G29	G28	
L30	125.35				G30, G32	G31	
L29	121.35	S10, S12	S11		G33, G35	G34	
L28	117.35				G36, G38	G37	
L22	93.35				G39, G41	G40	
L15	65.35				G42, G44	G43	
L14	61.35	S13, S15	S14		G45, G47	G46	
L8	37.35				G48, G50	G49	
L7	33.35				G51, G53	G52	
L2	13.35				G54, G56	G55	
L1	9.35				G57, G59	G58	
G	0.60	S16, S18	S17		G60, G62	G61	
B1	–3.40				G63, G65	G64	
B8	–31.15	S19, S21, S27	S20, S26	S22–24			

recording the translational and torsional responses of the building base, ground level and five other floors, which include the outrigger floors and a top floor (two floors below the roof), and the rocking responses of the building in both the N-S and E-W planes. This 27-channel SHM system satisfies the minimum requirements set forth by the new TBEC for the SHM systems on tall buildings [AFAD 2020].

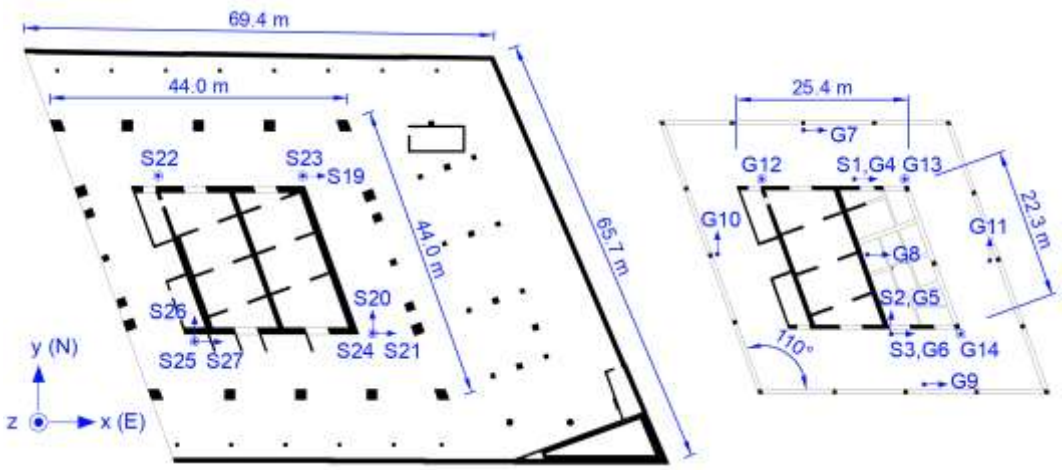

(a) (b)

Figure 4.2 Instrumentation of floors (a) B8 and (b) L52.

SHM system #2 was set up to gather more detailed information about the dynamic characteristics of the building. It consisted of 12 uniaxial accelerometers (24-bit force balance type with a bandwidth of DC to 100 Hz) [Guralp 2013], two six-channel digital recorders (24-bit) [Guralp 2009] and two GPS antennas. Three accelerometers were placed on floor L52 adjacent to those of SHM system #1. They were used as backup accelerometers for SHM system #1 and reference accelerometers for SHM system #2. Furthermore, they were used for checking time synchronization between two SHM systems. Remaining accelerometers of SHM system #2 were roved across 19 different floors in 12 test setups. For setup #1, floor L52 was further instrumented with four accelerometers along the floor edges, one accelerometer at the floor center in the E-W direction and three vertical accelerometers at three corners of the building core, as illustrated in Figure 4.2b. This setup enables checking the rigid floor diaphragm assumption, which is

commonly used in analyzing the recorded responses, and computing the rocking responses in N-S and E-W planes. For setup #2, two accelerometers in the E-W direction (G7 and G9) and an additional accelerometer were roved to floor L53. For setup #3, three vertical accelerometers (G12, G13 and G14) were roved to floor L53. Hence, typical floor instrumentation was also set up for floor L53. These setups enable the computation of interstory drift between floors L52 and L53. Likewise, for setups 4–12, six accelerometers were successively roved to lower floors: L42, L41, L33, L32, L31, L30, L29, L28, L22, L15, L14, L8, L7, L2, L1, G and B1, three on each consecutive floor, to enable the computation of interstory drifts and recording of responses at other intermediate floors while keeping the typical instrumentation on both floors L52 and L53. Consequently, SHM system #2 served as a 65-channel system.

Both SHM systems recorded the ambient vibration responses continuously at 100 samples per second for about four days from each channel. The only exceptions were the roving accelerometers; records were taken typically for one hour before roving them to their next locations.

4.3 In-Situ Natural Vibration Frequencies and Mode Shapes

Signal processing of the acceleration records is presented in the following. First, the recorded signals by three uniaxial accelerometers of SHM system #1 (S1, S2 and S3) that were placed adjacent to three uniaxial accelerometers of SHM system #2 (G4, G5 and G6) on floor L52 (see Figure 4.2b) were processed. Figure 4.3 compares the 0.05–3 Hz (a range that includes the first 12 natural vibration frequencies of the building as presented subsequently) band-pass filtered acceleration time histories. The records are identical, which indicates successful recording and time synchronization for both SHM systems.

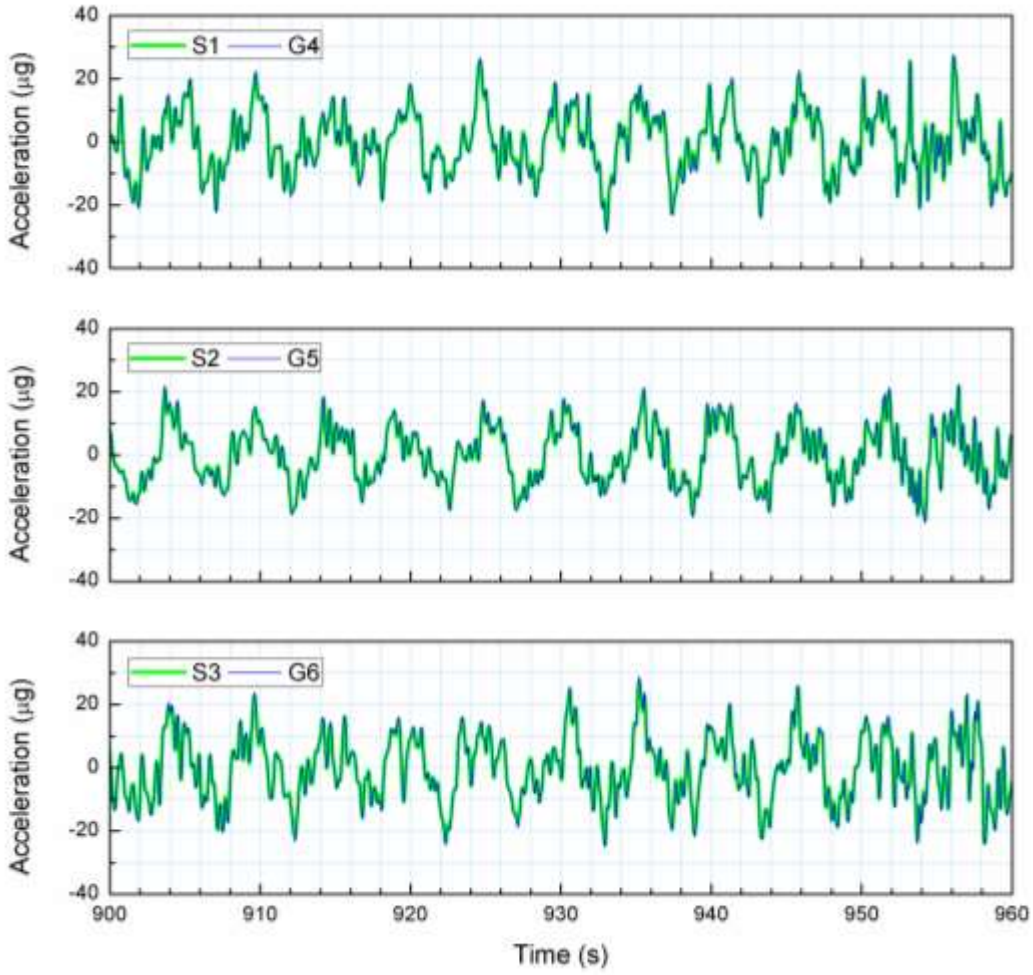

Figure 4.3 Comparisons of floor L52 acceleration time histories from both SHM system: 12.09.2018 10:00:00 GMT.

Next, the rigid floor diaphragm assumption was checked. If holds, it is possible to determine the translational and torsional floor responses by only three horizontal accelerometers placed on a floor, i.e., the typical floor instrumentation. Figure 4.4 compares the 0.05–3 Hz band-pass filtered torsional response of floor L52 computed from the translational responses recorded by parallel accelerometers along the edges of the building core (G4 and G6) and building perimeter (G7 and G9; G10 and G11). The records are identical; hence, the rigid floor diaphragm assumption is verified for both inside and outside the core and the use of the typical floor instrumentation is justified.

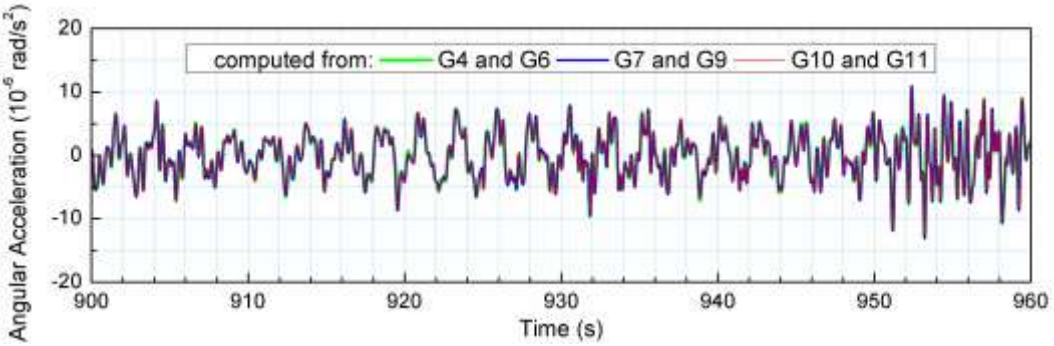

Figure 4.4 Torsional response of floor L52: 12.09.2018 10:00:00 GMT.

Then, E-W translational (x), N-S translational (y) and torsional (θ) floor accelerations were computed at the floor geometric center based on the rigid diaphragm assumption [Celik and Gulkan 2021a]. Figure 4.5 shows a sample of the 0.05–3 Hz band-pass filtered accelerations from hour-long records of SHM system #1. Mean Fourier amplitude spectra of the floor accelerations, computed using a moving Hanning window of 240 s with 50% overlap [Bindi et al. 2015; Welch 1967], are shown in Figure 4.6. The first 12 natural vibration frequencies of the building were identified from the frequencies at peak Fourier amplitudes. Note that the translational modes in the E-W and N-S directions are coupled due to parallelogram floor plan of the building as evidenced by the natural vibration mode shapes presented subsequently. Figure 4.7 shows that the identified frequencies from records of roving accelerometers of SHM system #2 are independent of the floor. The identified frequencies from hour-long floor response records of SHM system #1 with the maximum modal amplitudes do not show significant variations either during the day as shown in Figure 4.8 for a duration of two days.

Natural vibration mode shapes, determined from the Fourier amplitudes of the recorded responses at identified frequencies, which can also be determined from narrow band-pass filtered (centered around identified frequencies) responses in time domain (see Appendix B; see Figure 4.9 for the first two translational mode floor accelerations), are presented in Figure 4.10. The amplitudes of the roving accelerometers were first normalized with those from the reference accelerometers of the same setup and then scaled with respect to those of setup #3. Mode shapes

determined from the finite element model of the building, which is described subsequently, are also shown in Figure 4.10.

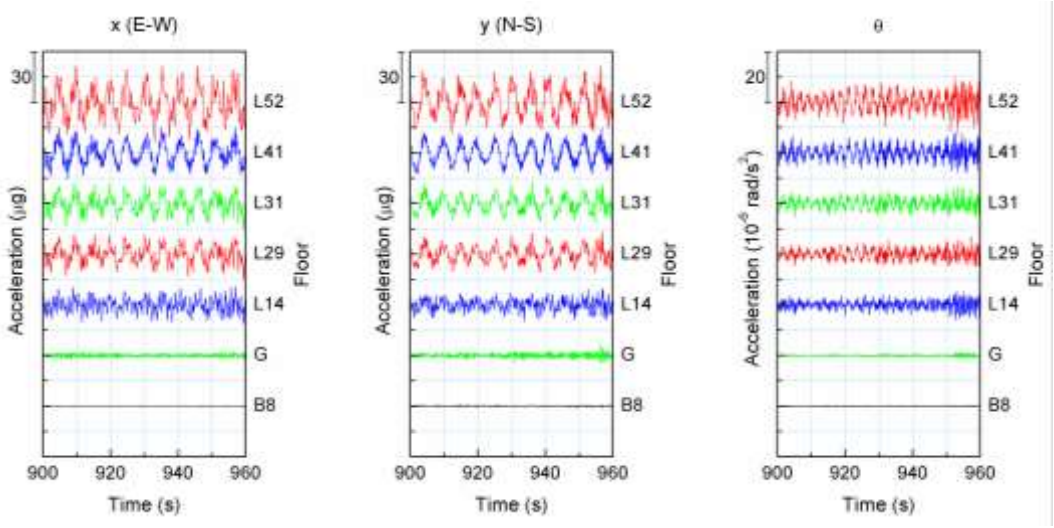

Figure 4.5 Floor acceleration time histories: 12.09.2018 10:00:00 GMT.

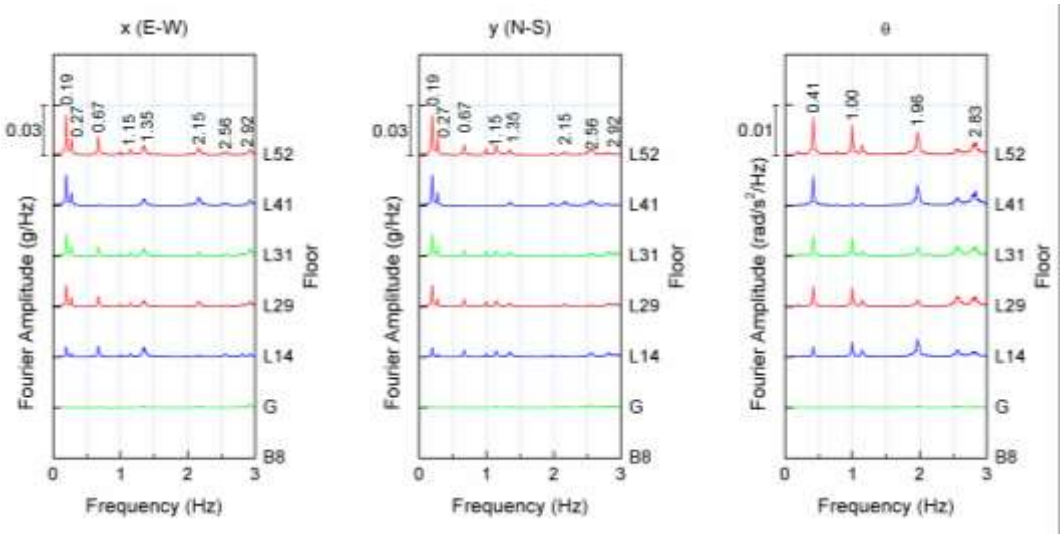

Figure 4.6 Fourier amplitude spectra of the floor accelerations: 12.09.2018 10:00:00 GMT.

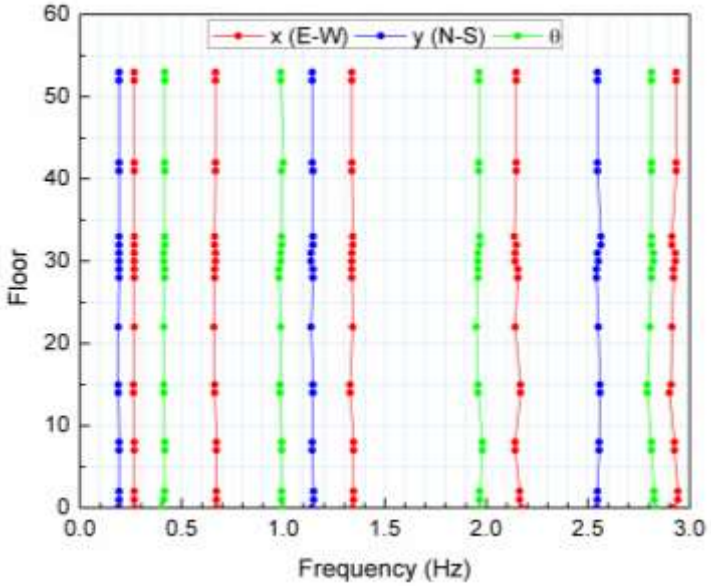

Figure 4.7 Natural vibration frequencies identified from floor responses: 12.09.2018 10:00:00 GMT.

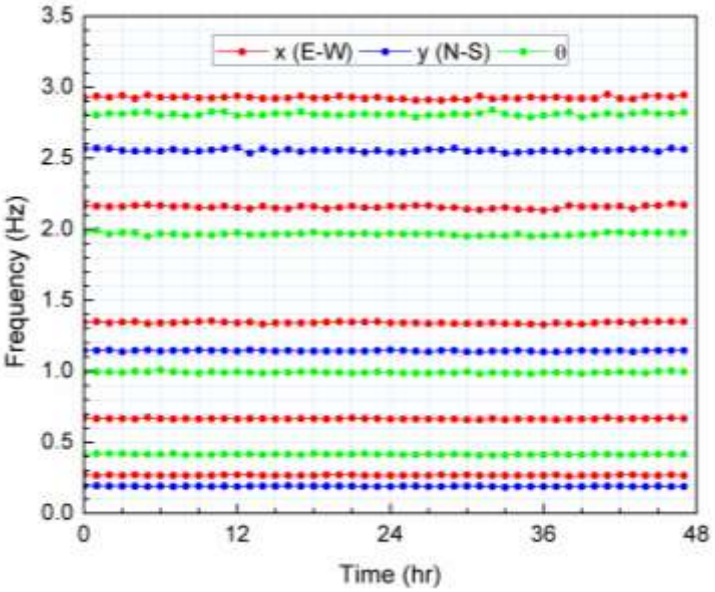

Figure 4.8 Natural vibration frequencies over two days: 12.09.2018 00:00:00–13.09.2018 23:00:00 GMT.

The contribution of rocking of the building to the horizontal floor accelerations is not significant. Figure 4.11 compares the 0.05–3 Hz band-pass filtered recorded response of floor L52 with the rocking-free response. Also shown in the figure is the

rocking contribution, which was computed by multiplying the rocking rotation determined from the vertical accelerometers at the corners of the building basement (S22, S23 and S24; see Figure 4.2a) [Celik and Gulkan 2021a] by the elevation difference between floors B8 and L52 [Celebi and Safak 1991].

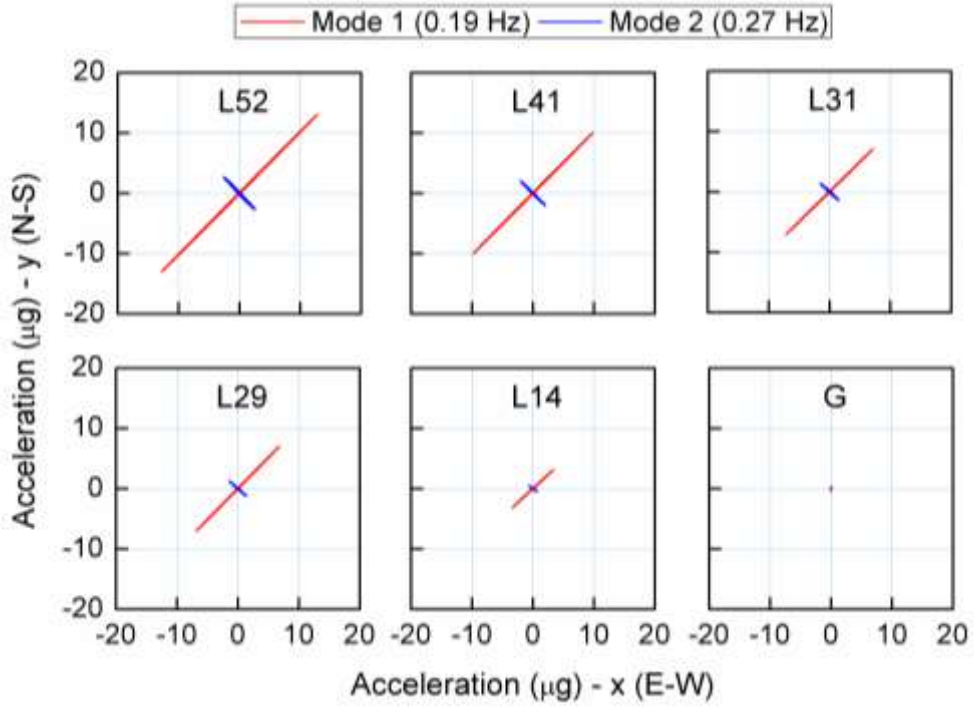

Figure 4.9 Instrumentation scheme First two translational mode floor accelerations: 12.09.2018 10:00:00 GMT.

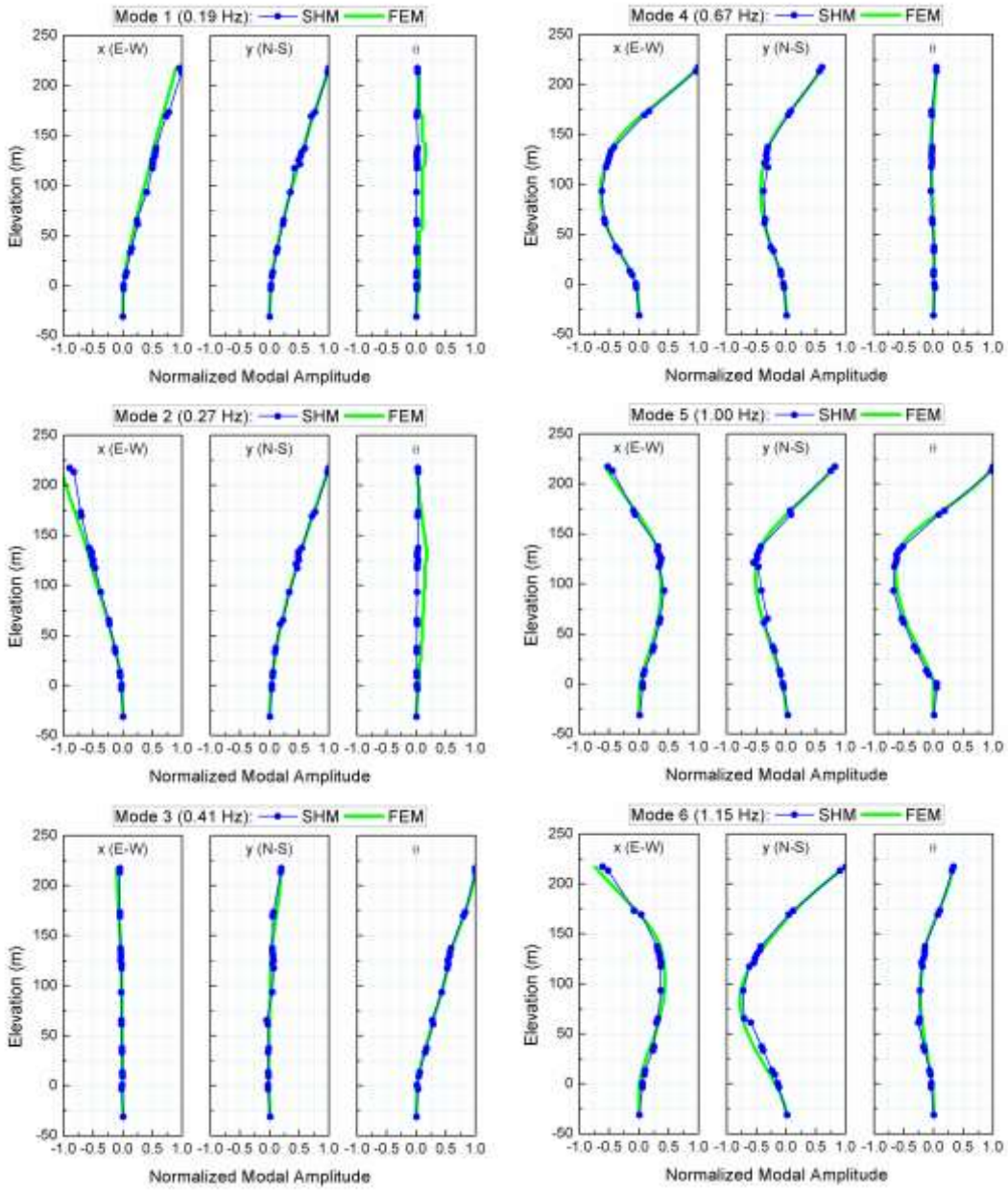

Figure 4.10 Natural vibration mode shapes.

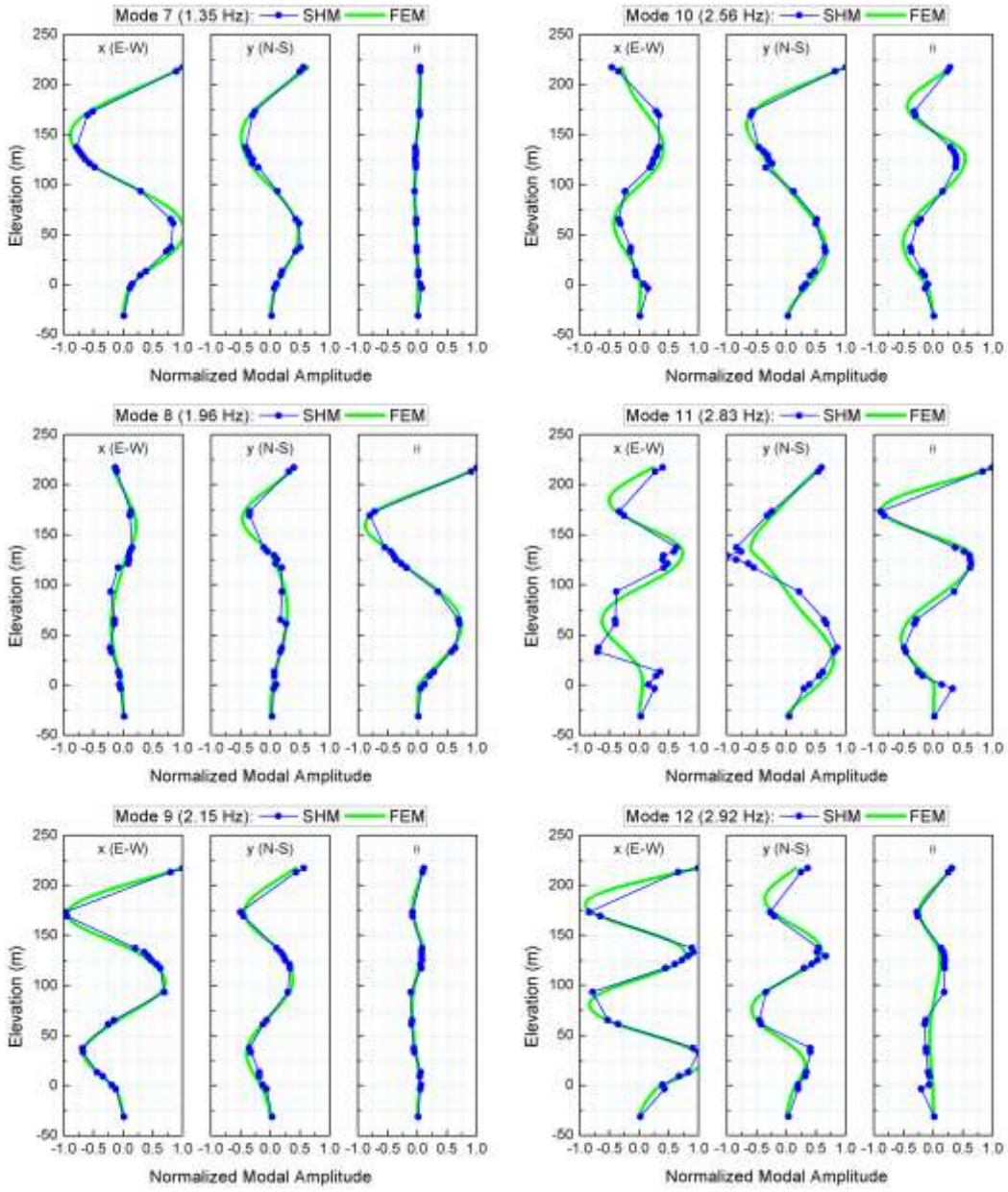

Figure 4.10 Natural vibration mode shapes (continued).

4.4 Dynamic Properties from the Finite Element Structural Model

A 3-D linear elastic finite element structural model of the building was developed using ETABS [CSI 2020] as shown in Figure 3.5. Four different variations of the model were considered for the eigenvalue analysis:

- Model #1 reflects the state of the building at the time of the testing campaign, when the building was vacant and there were no non-structural elements such as floor covering or partition walls. Hence, no superimposed dead loads or live loads were defined. The only exception was the superimposed dead loads defined for the facade elements, which were installed at the time. Gross section properties were used for all structural members. The model was validated subsequently using the identified dynamic properties of the building.
- Model #2a reflects the state of the building when in use. Superimposed dead loads and live loads were defined for the gravity load combination $1.0D + 0.25L$. Under gravity loads, flexural tensile strength can be exceeded in slabs; hence, Model #2b also incorporated cracked section properties for the slabs.
- Models #3 and #4 were developed for use in service-level and design-level evaluations, respectively. Code-prescribed cracked section properties were used in all RC members.

In the structural models, rigid diaphragms were defined at all floors as slabs were rigid in their own plane (see Figure 4.4) and fixed support conditions were employed as rocking of the foundation was insignificant (see Figure 4.11)

The moduli of elasticity for concrete were computed using

$$E_c = 5000\sqrt{f_{ck}} \tag{4.2}$$

which gives 38,700 MPa for the core shear walls, coupling beams and tower columns and 31,600 MPa for the other members [AFAD 2018a] and the Poisson's ratio for concrete was taken as 0.2 [TSI 2000]. The modulus of elasticity for structural steel was taken as 210,000 MPa.

Cracked section properties for RC members were defined by the effective section stiffness multipliers prescribed in [AFAD 2018a] separately for service-level and design-level evaluations, which are presented in Table 4.2.

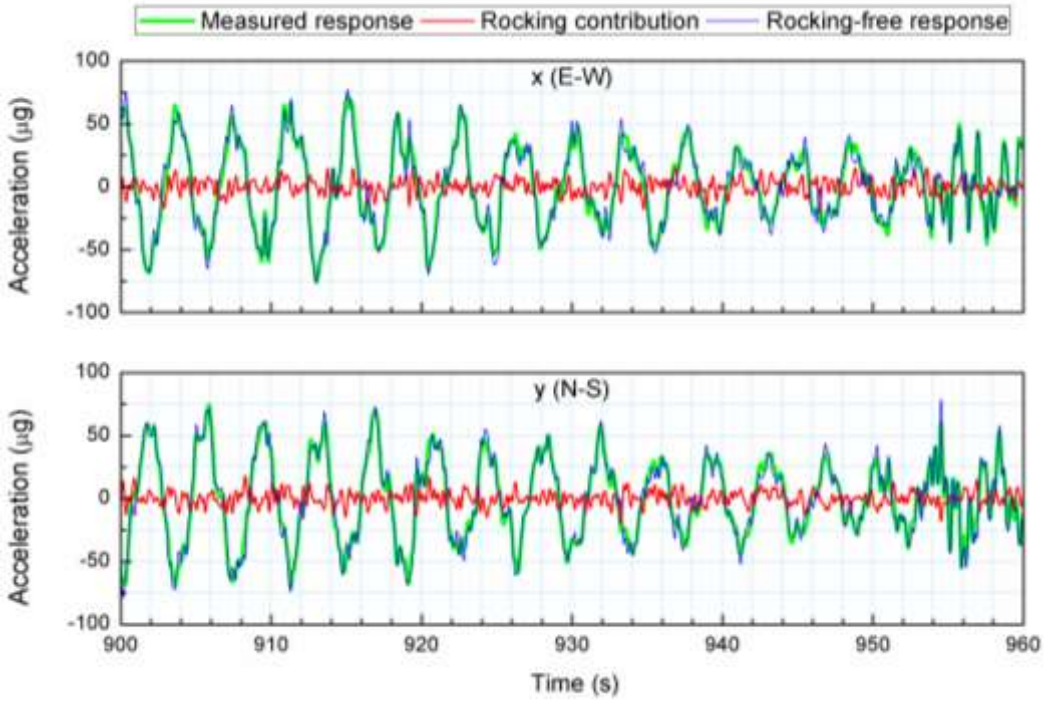

Figure 4.11 Rocking contribution to floor L52 acceleration time histories: 12.09.2018 06:00:00 GMT.

Table 4.2 Effective section stiffness multipliers for RC members.

	Service-Level Evaluation			Design-Level Evaluation		
Member	Axial	Flexural	Shear	Axial	Flexural	Shear
Shear wall (in-plane)	0.75	-	1.00	0.50	-	0.50
Basement shear wall (in-plane)	1.00	-	1.00	0.80	-	0.50
Slab (in-plane)	0.50	-	0.80	0.25	-	0.25
Shear wall (out-of-plane)	-	1.00	1.00	-	0.25	1.00
Basement shear wall (out-of-plane)	-	1.00	1.00	-	0.50	1.00
Slab (out-of-plane)	-	0.50	1.00	-	0.25	1.00
Column	-	0.90	1.00	-	0.70	1.00
Beam	-	0.70	1.00	-	0.35	1.00
Coupling beam	-	0.30	1.00	-	0.15	1.00

The unit weights of concrete and structural steel were taken as 24.5 kN/m^3 and 77 kN/m^3, respectively. Superimposed dead loads were defined as 1.5–2.5 kN/m^2 area

loads, whereas those for the facade elements were defined as 4.0 kN/m line loads. Live loads were 3.5 kN/m^2 at the tower floors and 5.0 kN/m^2 at the corridors and podium floors, whereas they were 7.5 kN/m^2 at some parts of the podium floors and 10–15 kN/m^2 at the mechanical floors.

Natural vibration frequencies (and periods) that were identified from the ambient vibration records and those determined from the finite element structural models are presented in Table 4.3 for the first 12 vibration modes of the building, together with the modal mass participation ratios. The frequencies determined from model #1, which reflects the state of the building at the time of testing, are almost identical to the in-situ frequencies, except for some higher modes but do not differ more than 4% on average or 8% at most. Natural vibration mode shapes from the finite element model are also almost perfectly matching with the in-situ mode shapes as illustrated in Figure 4.10. Hence, the use of moduli of elasticity for concrete given by Eq. 4.2 and gross section properties in model #1 successfully reproduces the test results. No updating in the finite element model is required. The frequencies from model #2a, which was developed for the building in use, are also close to the identified frequencies; the match is even better for higher modes. Slab cracking results in slight changes in frequencies, which are about 1% less in model #2b. Cracked section properties prescribed for the service-level and design-level evaluations (see Table 4.2) when incorporated in models #3 and #4, frequencies reduce about 10% and 30% on average, respectively. The fundamental period of the building identified at the time of testing, 5.3 s, is expected to lengthen to 5.9 s and 7.8 s upon cracking in structural members for the projected service-level and design-level states of the building, respectively.

Table 4.3 Natural vibration frequencies and periods, and modal mass participation ratios.

	Frequencies (Hz)						Periods (s)						Modal Mass		
		Model						Model					Participation (%)*		
Mode	SHM	#1	#2a	#2b	#3	#4	SHM	#1	#2a	#2b	#3	#4	E-W	N-S	θ
1	0.19	0.19	0.18	0.18	0.17	0.13	5.33	5.27	5.44	5.51	5.88	7.80	22	28	1
2	0.27	0.26	0.26	0.25	0.25	0.18	3.75	3.78	3.91	3.96	4.05	5.45	29	22	1
3	0.41	0.43	0.42	0.41	0.31	0.24	2.42	2.32	2.40	2.42	3.22	4.11	0	0	33
4	0.67	0.69	0.67	0.66	0.59	0.45	1.50	1.44	1.49	1.51	1.70	2.21	8	5	0
5	1.00	1.05	1.01	1.00	0.82	0.64	1.00	0.95	0.99	1.00	1.22	1.56	2	4	3
6	1.15	1.16	1.12	1.11	1.08	0.78	0.87	0.86	0.89	0.90	0.93	1.28	2	8	3
7	1.35	1.41	1.37	1.35	1.18	0.90	0.74	0.71	0.73	0.74	0.85	1.11	4	1	0
8	1.96	2.08	2.01	1.99	1.72	1.30	0.51	0.48	0.50	0.50	0.58	0.77	0	0	2
9	2.15	2.33	2.26	2.23	1.95	1.48	0.46	0.43	0.44	0.45	0.51	0.67	2	1	0
10	2.56	2.58	2.51	2.49	2.35	1.73	0.39	0.39	0.40	0.40	0.43	0.58	1	5	1
11	2.83	2.97	2.87	2.85	2.60	1.92	0.35	0.34	0.35	0.35	0.38	0.52	0	2	1
12	2.92	3.13	3.04	3.01	2.71	2.04	0.34	0.32	0.33	0.33	0.37	0.49	3	0	0

* For model #1

The modulus of elasticity for concrete in [LATBSDC 2020]:

$$E_c = 5400\sqrt{f_{ck}} \tag{4.3}$$

is 8% greater than that given by Eq. 4.2 and hence, if used in the finite element model, will lead to 4% shorter natural vibration periods. E_c, originally defined as a function of expected concrete strength to provide realistic estimates of stiffness in structural models, is presented as a function of f_{ck} as in Eq. 4.2 to facilitate the comparison. Expected strength is taken as 30% greater than f_{ck} to alleviate the conservatism in nominal or specified strength. In the previous editions, e.g., [LATBSDC 2015], expected strength was not explicitly reflected in the equation for E_c:

$$E_c = 4700\sqrt{f_{ck}} \tag{4.4}$$

If this equation is used in lieu of Eq. 4.2, natural vibration periods determined from the finite element model will be 3% longer. $E_c$in concrete design codes, TS 500 [TSI 2000] and Eurocode 2 [CEN 2004]:

$$E_c = 3250\sqrt{f_{ck}} + 14000 \tag{4.5}$$

$$E_c = 22000(0.1f_{ck} + 0.8)^{0.3} \tag{4.6}$$

respectively, are similar in values. They are 1% greater for the 60 MPa concrete used in the core shear walls, coupling beams and tower columns and about 10% greater for the 40 MPa concrete used in the other members, than those given by Eq. 4.2. The equation for E_c in ACI 318 is the same as Eq. 4.4 and it is noted that in-situ $E_c$values can range from 80% to 120% of the computed values [ACI, 2014]. Notwithstanding that all E_c values computed using Eqs. 4.2–4.6 fall within this range, the finite element model that used E_c in [AFAD 2018a] reproduce the in-situ natural vibration periods without a need for model updating.

4.5 Damping Ratios from the Random Decrement Technique

Random decrement technique, which was developed by Cole [1973] for damage detection and damping computation in aerospace structures from ambient vibration response records, has found wide use in civil engineering structures [Rodrigues and Brinker 2005; Zhou and Li 2021]. On the other hand, damping ratios computed using the half-power bandwidth method from the mean Fourier amplitude spectra of the windowed segments of the ambient vibration response records (e.g., Figure 4.6) overestimate the actual damping due to factors such as smoothing [Kijewski and Kareem 2002; Rodrigues and Brincker 2005; Cruz and Miranda 2017]. Likewise, damping ratios computed using the logarithmic decrement method from the auto-correlation functions of the windowed segments of the ambient vibration response records are very sensitive to the parameters employed [Magalhaes et al. 2010].

Random decrement signature, which is representative of the free vibration response with an initial displacement, is extracted by averaging segments of ambient vibration records with the same initial (triggering) conditions. This ensemble average [Welch 1967] is proportional to the auto-correlation of the response for a linear time invariant system subjected to a zero-mean stationary Gaussian white noise process [Vandiver et al. 1982; Spanos and Zeldin 1998]. Random decrement signature converges to the free decay response with increasing number of segments as the response due to the random excitation vanishes with averaging [Rodriguez and Brincker 2005; Wen et al. 2018] as shown in Figure 4.12 for the first-mode N-S displacements of floor L52. Damping ratio is then computed using the logarithmic decrement method.

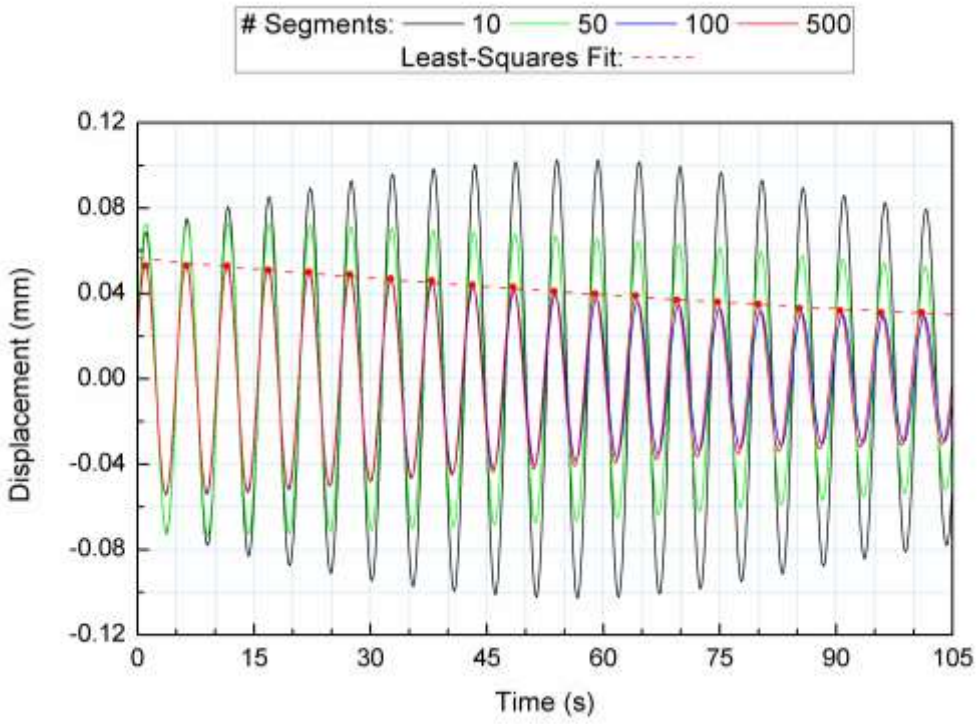

Figure 4.12 Random decrement signatures for the first-mode N-S displacement of floor L52 12.09.2018 10:00:00 GMT.

First, modal displacements are computed by narrow band-pass filtering (centered around identified frequencies) and double integrating the accelerations. The filter bandwidth is an important parameter in computing the modal damping ratios; too

narrow a filter results in underestimation of damping, whereas too wide a filter precludes extracting a single mode [Tamura et al. 2002]. Next, segments of displacement time histories are extracted with the same initial conditions, triggered when the amplitude is above a set threshold and the slope is positive [Rodriguez and Brincker 2005; Zhou and Li 2021]. The threshold value is typically set as a function of the standard deviation, σ, of the response time history, ranging from 0.2σ to 5σ [Zhou and Li 2021]. A high threshold reduces the noise effects but also reduces the number of segments as noted subsequently. The length of segments is another important parameter in computing the modal damping ratios and is chosen to include at least 5 to 20 vibration cycles [Zhou and Li 2021]. Then, the random decrement signature is computed by ensemble averaging. With limited amount of recording times, segment overlapping is allowed because the number of segments, another important parameter, is not adequate otherwise [Zhou et al. 2021]. Lastly, modal damping ratio is computed by fitting a line to the natural logarithms of the peaks of the random decrement signature in a least-squares sense (see Figure 4.12) [Safak and Cakti 2004].

Repetition of the above procedure leads to the following optimum values for the random decrement technique parameters: the threshold value was set to 0.5σ, the number of segments was set to 500, the length of segments was set to include 20 vibration cycles and the filter bandwidth was set to $0.20f_n$ (f_n is the modal frequency), which are used as the basis for the subsequent comparisons. Figure 4.13a shows the variation of the first mode damping ratio, computed from hour-long records of floor L52, over two days for four different threshold values: 0.2σ, 0.5σ, 1.0σ and 1.5σ. Damping values computed using the same hour-long records do not differ significantly as compared to the change in damping at different hours. However, no functional relationship for the dependency of damping on the response amplitude [Tamura and Suganuma 1996; Satake et al. 2003] is observed at the recorded vibration levels. For higher threshold values, it is not possible to include 500 segments from an-hour-long record into the random decrement signature; e.g., the number of segments is around 400 for a threshold set to 1.0σ, whereas 200 for

1.5σ. Figure 4.13b shows the comparisons for four different numbers of segments: 100, 250, 500 and around 600. Damping values converge as the number of segments used in the computation increases. The number of segments can be increased beyond 600 if two-hour-long records are used; however, the variation in damping at different hours can be overlooked in that case. Figures 4.13c and 4.13d show the comparisons for four different segment lengths that include 5, 10, 15 and 20 vibration cycles and four different filter bandwidth values of $0.05f_n$, $0.10f_n$, $0.15f_n$ and $0.20f_n$, respectively. The use of a segment length including more than 10 cycles and a filter bandwidth wider than $0.10f_n$ results in consistent damping values at each hour.

Figure 4.14 shows the variations of the damping ratios, computed using the optimum values mentioned above, over two days for the first six vibration modes. The histograms of modal damping ratios are given in Figure 4.15. The median damping ratios are 0.6% for all the modes except for the second mode, which is 0.5%. The coefficients of variation are in the order of 0.3–0.4. These damping ratios can be considered as lower-bound values for service-level evaluations prescribed in design provisions [LATBSDC 2020; PEER 2010].

The impact of damping ratios on the structural response was examined by simulating the building response to an earthquake ground motion for three damping levels: 0.6% (median in-situ damping), 1.3% (upper-bound value for service-level evaluation in [LATBSDC 2020]; Eq. 4.1) and 2.5% (specified value for both service-level and collapse-level evaluations in AFAD [2018a]; lower-bound value for collapse-level evaluation in LATBSDC [2020]). On September 26, 2019, Istanbul region was hit by a M_w 5.8 earthquake that occurred 8 km deep in the Marmara Sea, with epicenter 70 km away from the building [AFAD 2022]. Station #3407 of National Strong Motion Network of Turkey, which is 3 km away from the building and 70 km from the epicenter, where V_{s30} is 595 m/s, similar to that at the building site, recorded the acceleration time histories that are presented in Figure 4.16.

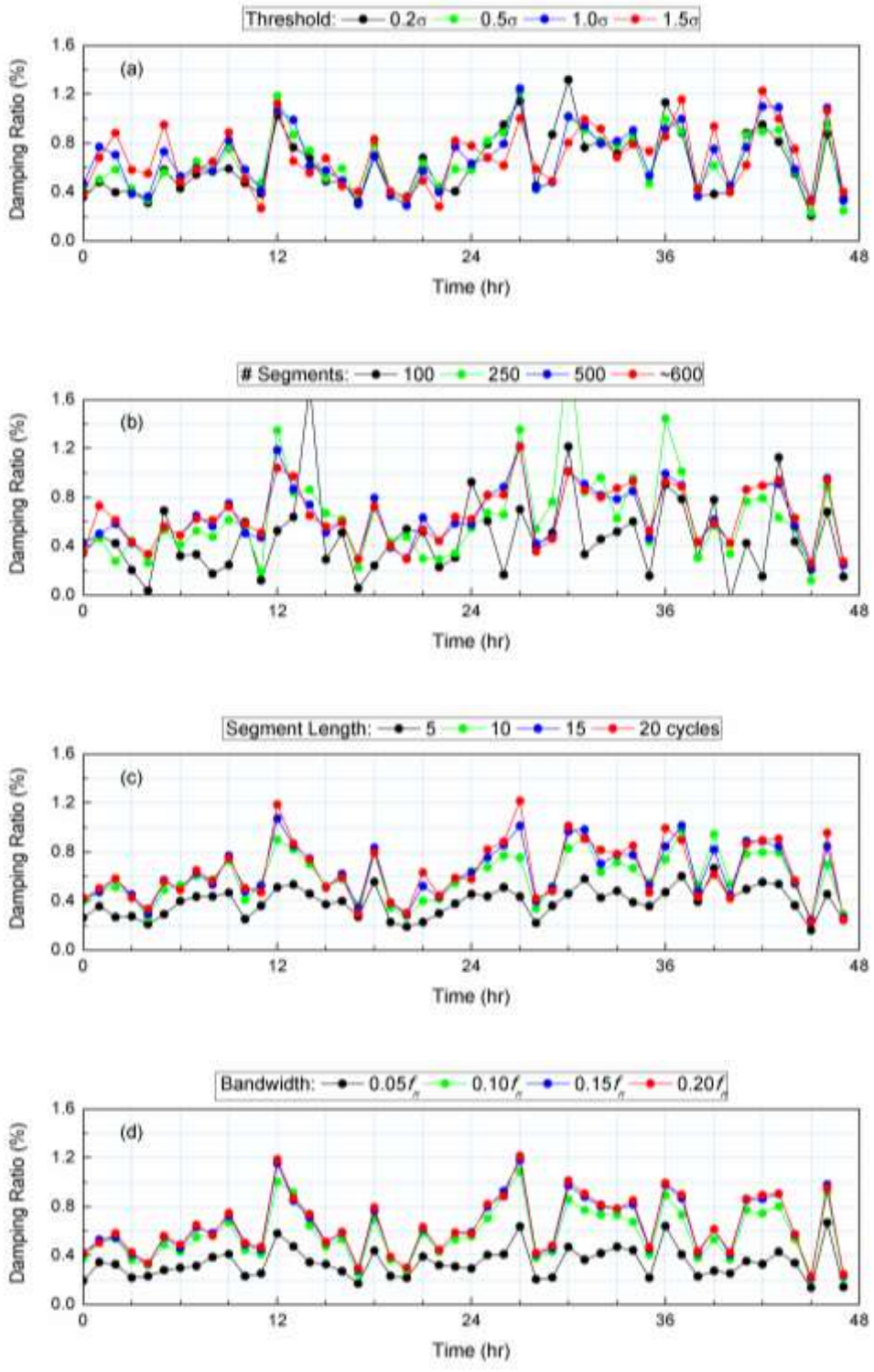

Figure 4.13 First mode damping ratio ever two days as a function of random decrement technique parameters: 12.09.2018–00:00:00 13.09.2018 23:00:00 GMT.

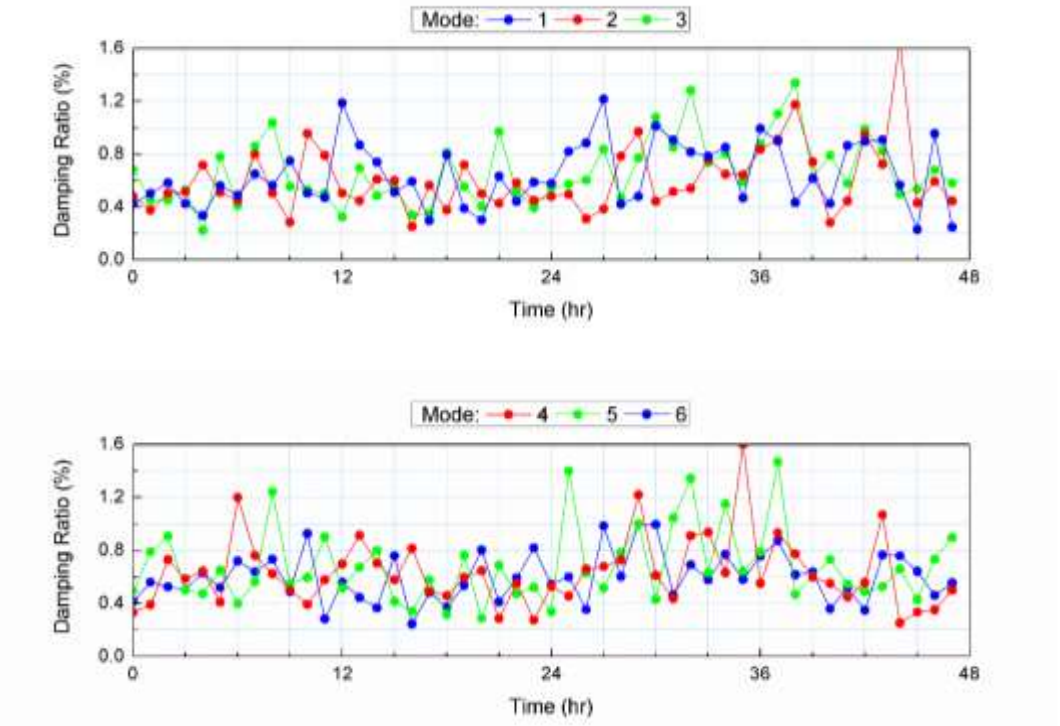

Figure 4.13 Damping ratios over two days for the six vibration modes: 12.09.2018 00:00:00–13.09.2018 23:00:00 GMT.

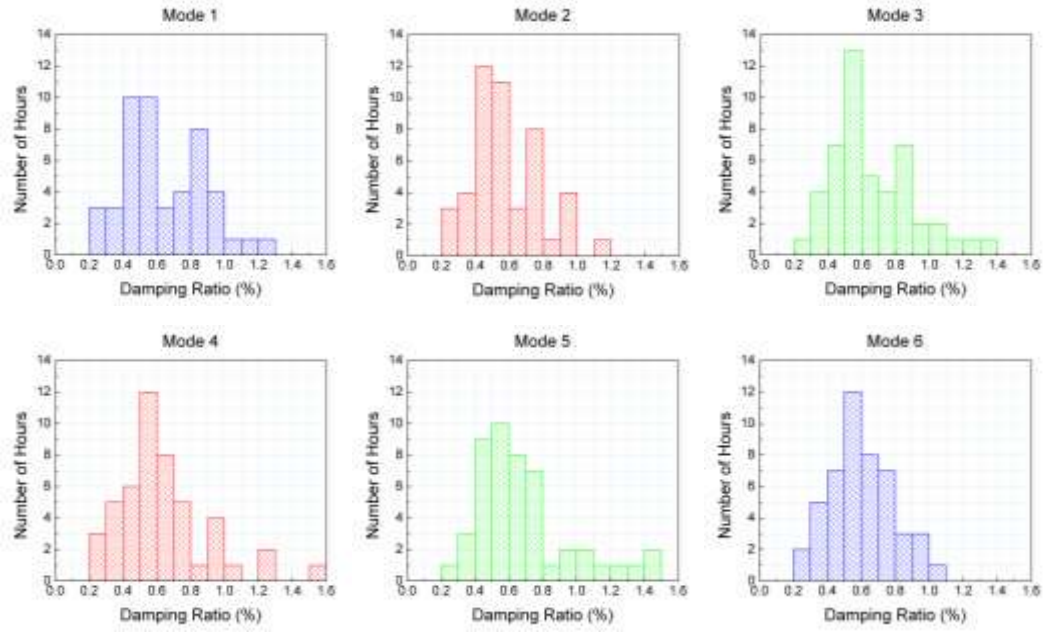

Figure 4.14 Histogram of modal damping ratios over two days: 12.09.2018 00:00:00–13.09.2018 23:00:00 GMT.

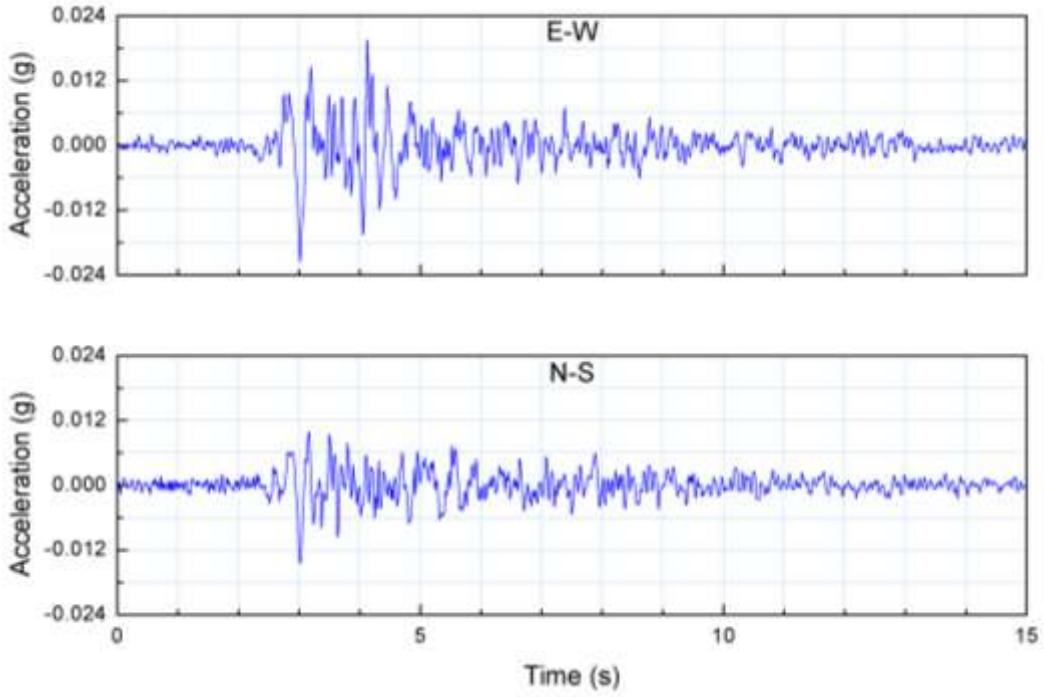

Figure 4.15 2019 M_w 5.8 Marmara Sea earthquake ground motion records (station #3407).

The intensity of the 2019 M_w 5.8 Marmara Sea earthquake at this site, where the peak ground acceleration (PGA) is 0.022 g along the E-W direction, is well below the SLE intensity for the building. Hence, linear time history analysis of the building was performed using the recorded earthquake ground motions, rotated to the building axes. Peak floor accelerations (PFAs) computed from model #3 using 0.6%, 1.3% and 2.5% Rayleigh damping ratios for the first and sixth modes are presented in Figure 4.17, which shows that the responses are highly dependent on the damping values. Accordingly, the need for accurate damping values is highlighted. In any case, the in-structure amplification factor in ASCE 7-16 [2017a]:

$$PFA/PGA = 1 + 2(z/H) \tag{4.7}$$

where z is the height of the floor of interest with respect to the base, does not consider damping ratio, which is challenged by the results in Figure 4.17. PFAs are taken equal to PGA for the floors buried in the ground below the base, which is the case for this building for the podium floors below zero elevation in Figure 4.17. Hence,

Eq. 4.7 with this modification is represented by the bi-linear envelope in Figure 4.17. Apparently, Eq. 4.7 highly overestimates the responses at the upper floors when compared with PFAs computed using the suggested 1.3% damping ratio, consistent with the criticism of previous studies [Reinoso and Miranda 2005; Anajafi and Medina 2018] and underestimates the responses at the lower floors. Seemingly, the PFAs at the podium floors buried at three sides under the base (see Figure 3.5) are not equal to PGA; PGA is amplified significantly.

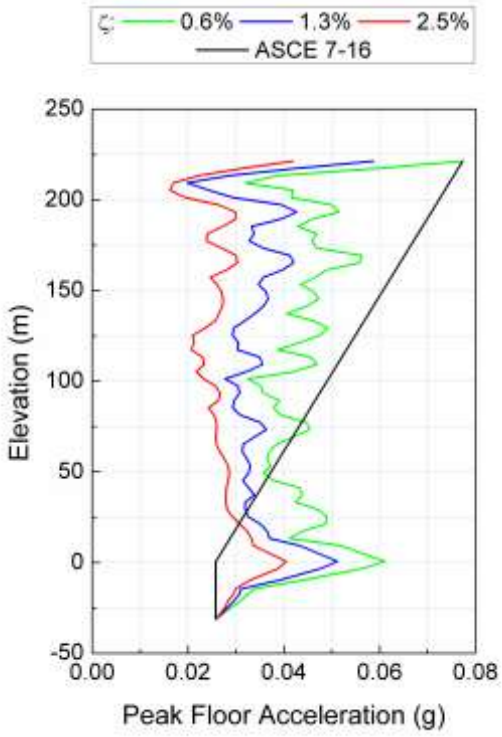

Figure 4.16 Simulated PFAs.

4.6 Summary

An ambient vibration survey was performed on a 253 m tall RC building in Istanbul, whose structural system consists of outriggers connecting the core walls to the peripheral composite columns, designed according to performance-based seismic design principles. During the five-day testing campaign, the 62-story building was instrumented with a monitoring array of 92 channels of accelerometers deployed on

20 different floors to identify its dynamic characteristics. Natural periods (and frequencies) of the building were identified for the first 12 vibration modes. Translational modes are coupled due to the skew geometry of the building in plan. No significant changes were observed in the modal period values during the day, which can mostly be attributed to the building being vacant at the time. Otherwise, the changes are typically attributed to factors such as live load and temperature variations.

The identified natural vibration periods and mode shapes were used in validating the 3-D finite element structural model developed for the state of the building at the time of testing. It is shown that no finite element model updating is required when gross section properties with moduli of elasticity for concrete per [AFAD 2018a] were used in the structural model. Upon successfully reproducing the test results, natural vibration periods were then predicted for the building in use by incorporating the superimposed dead loads and live loads in the structural model. Periods were also predicted for service-level and design-level states of the building by using the prescribed cracked section properties in all structural members [AFAD 2018a]. The in-situ fundamental period at the time of testing, 5.3 s, is predicted to increase to 5.9 s and 7.8 s for the projected service-level and design-level evaluations, respectively.

Both performance evaluations also call for accurate damping properties to reliably predict the demands on tall buildings. Random decrement technique was used to investigate the modal damping ratios. Statistical analysis using the random decrement technique essentially yielded median damping ratios of 0.6% with coefficients of variation in the order of 0.3–0.4 for the first six vibration modes, which can be considered as lower-bound values for service-level evaluations prescribed in design provisions [LATBSDC 2020; PEER 2010]. These low damping values observed in tall buildings [Bernal et al. 2015; Cruz and Miranda 2017] need to be considered in service-level evaluations.

The simulated response of the building to the 2019 M_w 5.8 Marmara Sea earthquake ground motions, recorded at a strong ground motion station in close proximity to the

building, using the median in-situ damping ratios shows that the PFAs under this SLE exceed the ASCE 7-16 [ASCE 2017a] in-structure amplifications at the lower floors and do not reach to those values at the upper floors.

Permanent instrumentation can provide more insights into the dynamic behavior of tall buildings when structural responses under design-level wind loads and earthquake ground motions are recorded. Reliable 3-D dynamic response analysis of tall buildings requires knowledge of structural dynamic properties; hence, those identified for the 253 m tall office building in Istanbul in this study contribute to the existing database of dynamic properties of tall buildings.

CHAPTER 5

SEISMIC DESIGN AND PERFORMANCE REVIEW

5.1 Introduction

In conventional seismic design of RC buildings, design loads are calculated from a load combination that includes the prevailing earthquake loads, structural analysis is performed under these loads to determine the internal design forces, and required strengths are assigned to members by proper reinforcement placing and detailing. Then, several checks are performed for satisfying the force-controlled and deformation-controlled performance requirements. If some of these requirements are not satisfied, the design is revised, which is usually undertaken by changing the member sizes and reinforcement, and seldom by changing the structural system.

Primary factors that control the seismic design of tall buildings can be classified as structure-related global factors and member-related local factors. Structure-related factors are simply the lateral loads that control the design (design earthquake or wind), minimum base shear requirements under the SLE, interstory drift limitations under the SLE, 50-year wind and the MCE, and floor acceleration limitations under the 10-year (or 2- to 5-year) wind. Member-related factors, on the other hand, are reinforcement limits, moment and shear DCR limits and axial stress limits for force-controlled response under the design load combination in Eq. 3.1, and concrete and steel strain limits for deformation-controlled response under the MCE.

This chapter discusses the primary factors that control the seismic design of the building; presents the response parameters that control the service and safety performance levels under the SLE and MCE, respectively, and the response parameters that control the collapse performance; and predicts the partial collapse spectrum from the MCE spectrum.

5.2 Factors Controlling Seismic Design

This section evaluates the seismic performance of the building under the seismic and wind loads that were determined at the planning stage of the building design in 2016. In the nonlinear analysis presented, ground motions pairs in set #1 were used.

5.2.1 Structure-related global factors

5.2.1.1 Base shear force and story shear forces

The base shear forces determined under the SLE and 50-year wind loads are compared with the minimum base shear force in Table 5.1. Due to close-coupled modal responses, base shear forces under the SLE spectrum were calculated using complete quadratic combination (CQC). Table 5.1 indicates that the base shear forces obtained under the SLE spectrum governs the design base shear force. Note that the effective seismic weight of the building is 2,128,000 kN, which is the combination of the dead load and 25% of the total live load.

Table 5.1 Comparison of base shear forces.

Loading	**Base Shear**		
Direction	**Minimum**	**SLE**	**Wind**
X	0.015*W*	0.035*W*	0.011*W*
Y	0.015*W*	0.043*W*	0.011*W*

Story shear forces under the SLE and 50-year wind loads are presented in Figure 5.1a in both orthogonal directions. Wind loads were the envelope of 48 combinations of two translational components and one torsional component from the wind tunnel tests. They act at the centroids of the above ground floors. It is evident that the story shears and accordingly the internal shear design forces are controlled by the SLE.

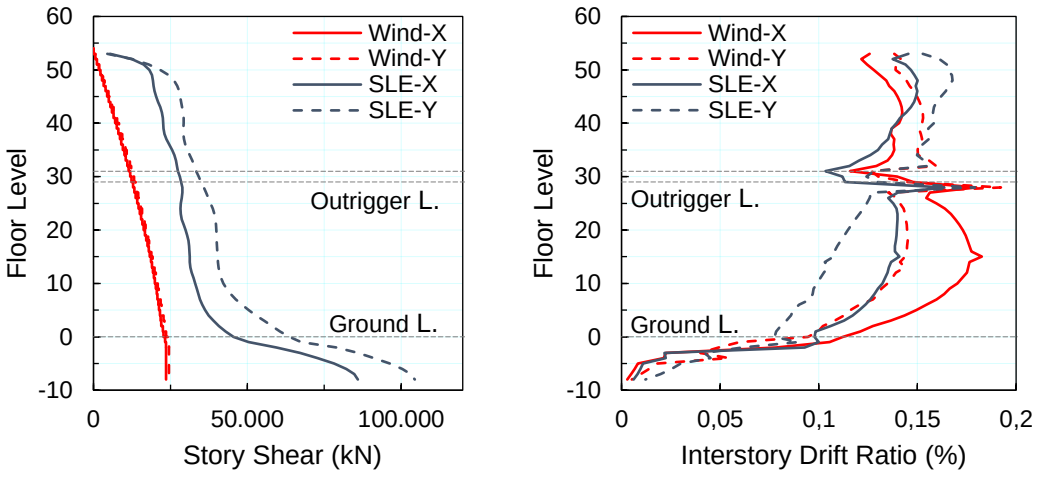

(a) (b)

Figure 5.1 (a) Story shear forces and (b) interstory drift ratios under SLE spectrum and 50-year wind loads.

5.2.1.2 IDRs under service level loading: SLE and 50-year wind

IDRs determined under the SLE and 50-year wind loads are shown in Figure 5.1b. Drifts are presented for the maximum interstory drift in a story in each orthogonal direction. The torsion component of the 50-year wind does not contribute to story shear, but significantly contributes to the maximum interstory drift in a story. Hence, although story shears under the wind loads are less, wind loads produce larger interstory drifts at lower stories compared to the SLE excitation.

The wind forces control interstory drifts up to floor 30 (below the outrigger level) and the earthquake forces control above floor 30. However, IDRs are significantly below the 0.5% limit under the SLE, and reasonably below the 0.2% limit under the 50-year wind. Accordingly, drift limits under service level loading conditions do not control the design of this building. More stringent drift limits may have been enforced by the codes however for further limiting the costly in-plane non-structural damage under service level loads.

5.2.1.3 IDRs under MCE

IDRs were determined by NTHA under seven pairs of ground motions (set #1) where each pair acts simultaneously in both orthogonal directions, combined with the seismic weight of the building. Figure 5.2 shows the IDRs in both orthogonal directions, calculated for the maximum drift at the associated edge for each story. IDRs under the MCE ground motions satisfy the design limits comfortably. They do not control the building design. This result indicates significant overdesign, which deserves further discussion in view of the overall building performance.

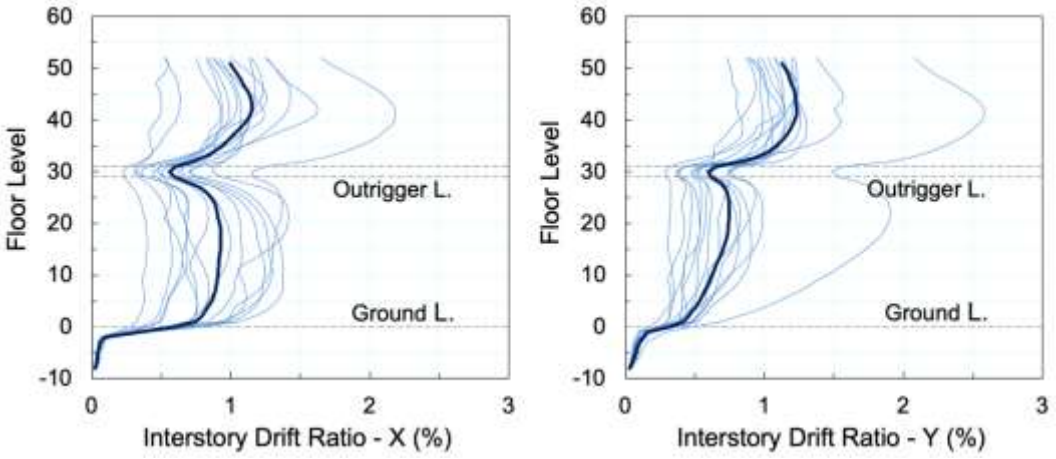

(a) (b)

Figure 5.2 Interstory drift ratios in (a) X and (b) Y directions under MCE ground motions.

5.2.2 Member-related local factors

Core walls, coupling beams, outriggers, perimeter columns and perimeter beams are discussed separately in the following.

5.2.2.1 Core walls

Core walls are the components that dominate the seismic performance of tall buildings. Basic factors that control core wall design are axial stress limits, minimum flexure and shear reinforcement ratios, DCR limits and axial strain limits under the SLE and MCE excitations.

Axial stress limit

The normalized compressive stresses of several wall segments under the design load combination in Eq. 3.1 are shown in Figure 5.3. The axial stress limit is specified as 0.35 in AFAD [2018a], but dictated as 0.25 by the peer review members. It is evident that the thicknesses of the exterior and interior segments at the ground story and stories below are controlled by the normalized axial stress limit of 0.25. This limit does not control the thicknesses of wall segments at stories above. Although the thicknesses of these segments may seem conservative, they were not reduced in proportion to the axial stress demands in order to avoid stiffness discontinuity under the MCE excitations. Hence, the sizes of the core wall segments are controlled by the axial stress limit.

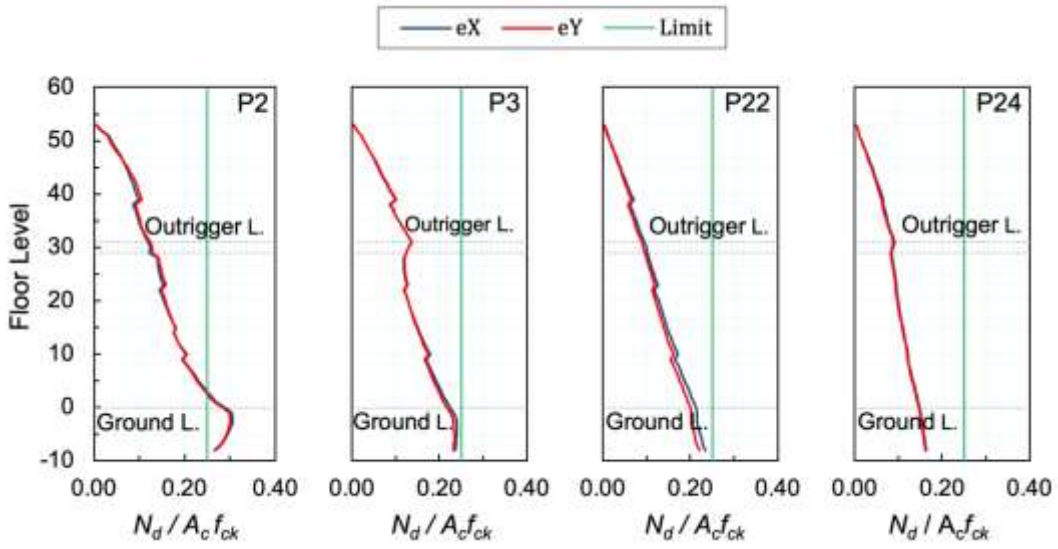

Figure 5.3 Normalized compressive stresses in core wall segments ($e_X =$ envelope$(D + 0.25L \pm E_X \pm 0.3E_Y)$, $e_Y =$ envelope$(D + 0.25L \pm E_Y \pm 0.3E_X)$).

Longitudinal and transverse reinforcement limits

In general, longitudinal reinforcement limits do not govern the flexural design of wall segments. The required reinforcement ratios are always within the specified reinforcement limits, both at the unconfined middle regions and the confined end regions. Hence, the flexural design of core wall segments is controlled by the SLE.

The shear design of core wall segments is controlled by the MCE. It was required to increase the horizontal shear reinforcement ratio from the minimum of 0.0025 to about 0.005–0.01. Shear forces determined from the response spectrum analysis under the SLE and mean shear forces determined from time history analysis under the MCE ground motions are compared with the provided shear capacities V_r in Figure 5.4 for the wall segments P3 and P24. The horizontal reinforcement ratios in P3 and P24 were increased to 0.0051 and 0.0063 on average, respectively. Shear forces that are developed at the podium level due to the backstay effect and at the outrigger level under the MCE control the shear reinforcement. Horizontal reinforcement ratio was not reduced at the other elevations in order to avoid shear strength discontinuity.

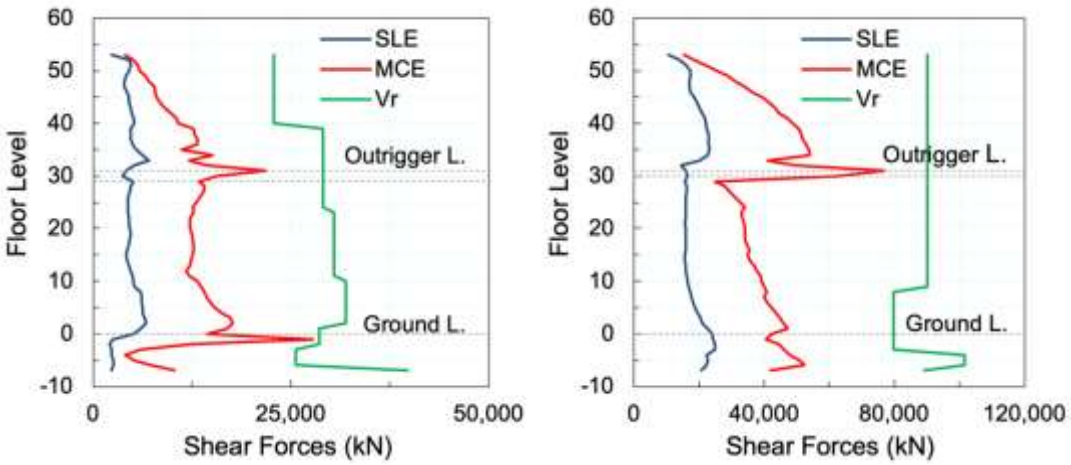

(a) (b)

Figure 5.4 Shear forces and shear capacities of wall segments: (a) P3 and (b) P24.

DCR limits

Moment and shear DCRs calculated under the SLE are presented in Figure 5.5 The provided longitudinal reinforcement satisfies the flexural DCR limit of 1.5 and the shear design summarized above satisfies the shear DCR limit of 0.7 in all wall segments.

Mean shear DCRs under the MCE ground motions obtained from NTHA are compared with the DCR limit of 1.0 in Figure 5.6. The shear design satisfies the DCR limit at all levels, but with small margins at the ground and outrigger levels. Therefore, moment and shear DCR limits under both the SLE and MCE do not have any control on the core wall design

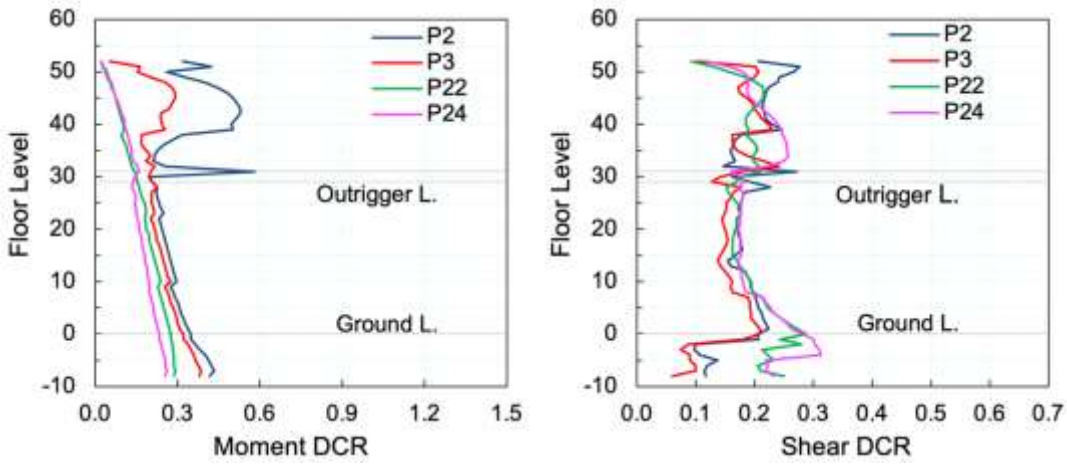

(a) (b)

Figure 5.5 (a) Moment and (b) shear DCRs of wall segments under SLE spectrum.

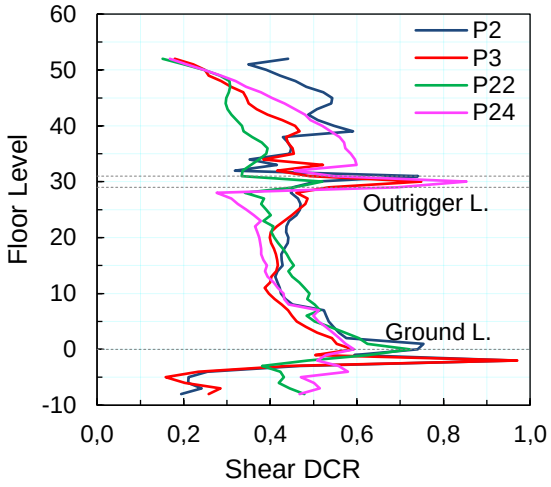

Figure 5.6 Mean shear DCRs of wall segments under MCE ground motions.

Axial strain limits under MCE

Axial strains calculated under seven pairs of MCE ground motions are presented in Figure 5.7 for four wall segments. Steel yielding is observed only at the ground and outrigger levels as expected; however, steel strains are much lower than the collapse prevention (CP) limit of 0.03. Concrete compressive strains are also much lower than the CP limit of 0.01; they do not even reach the strain at peak stress (ε_{c0}). The strains presented in Figure 5.7 indicate that the flexural response of the core wall segments under the MCE ground motions is essentially linear elastic, with slight yielding at two critical locations. This is a further indication of overdesign. Maximum strains in longitudinal reinforcement do not control the flexural design of the core walls in this building.

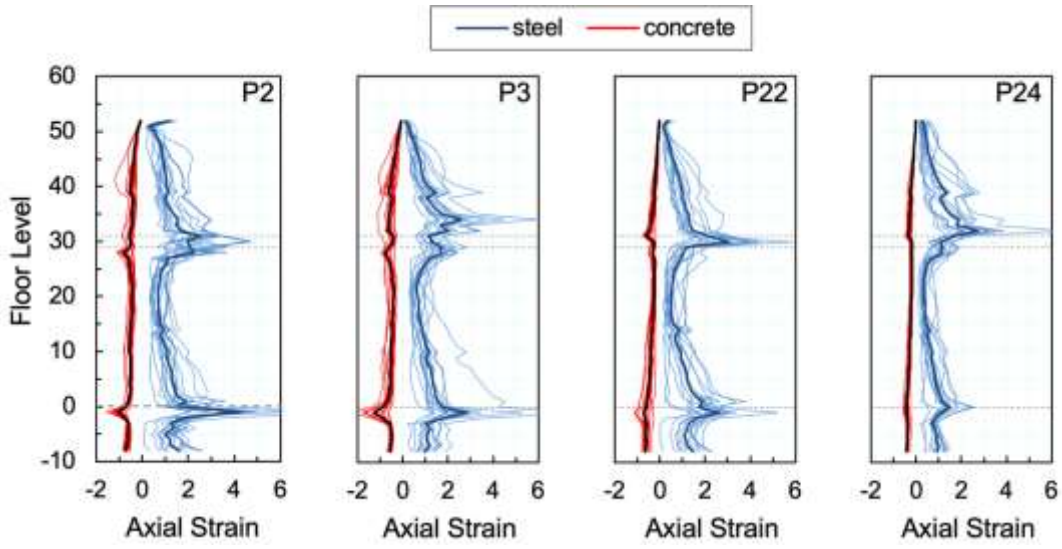

Figure 5.7 Axial strains of wall segments under MCE ground motions ($\times 10^{-3}$).

5.2.2.2 Coupling beams

There are two types of coupling beams at each story, both in the same transverse direction (see Figure 3.2). The first type is shorter, 2.2 m long and 0.85 m deep, and the second type is longer, 3.3 m long and 1.12 m deep. The clear span-to-depth ratios are 2.6 and 2.9, respectively. Their thicknesses conform to the thickness of adjacent walls. Standard flexural design procedure was used in the design of coupling beams under the internal forces from the load combination in Eq. 3.1. Shear design was based on capacity shear. Diagonal reinforcement was not considered in design. The results are presented for the longer coupling beams (CB2; see Figure 3.2) only.

Longitudinal and transverse reinforcement limits

The longitudinal and transverse reinforcement ratios of the longer coupling beams are shown in Figure 5.8. Longitudinal reinforcement is symmetrical at the top and bottom since the distributed vertical loads on the beams are negligible, and the transverse reinforcement ratio does not vary along the beam span. The longitudinal and transverse reinforcement limits of the coupling beams have no control on their design. Concrete compressive stresses along the diagonal struts are below the code limits [AFAD 2018a; ACI 2014].

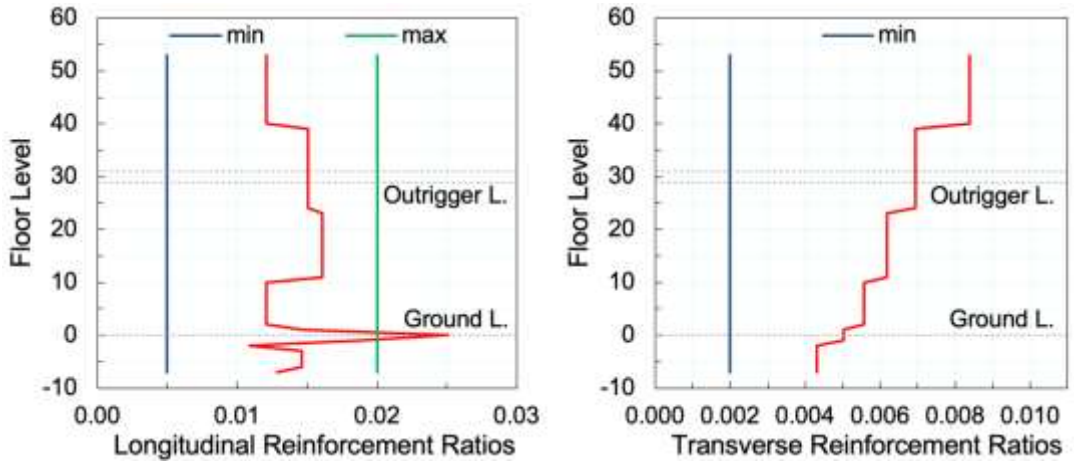

(a) (b)

Figure 5.8 (a) Longitudinal and (b) transverse reinforcement ratios of coupling beams.

DCR limits

The moment and shear DCRs under the SLE and the shear DCRs under the MCE are safely below the associated DCR limits. They do not control the design and are not presented herein.

Axial strain limits under MCE

Curvatures, and mean concrete and steel strains under the MCE ground motions are presented in Figure 5.9. Although there is significant yielding at all stories, material strains are well below the specified limits. Hence, the design of coupling beams is only controlled by the internal forces under the SLE.

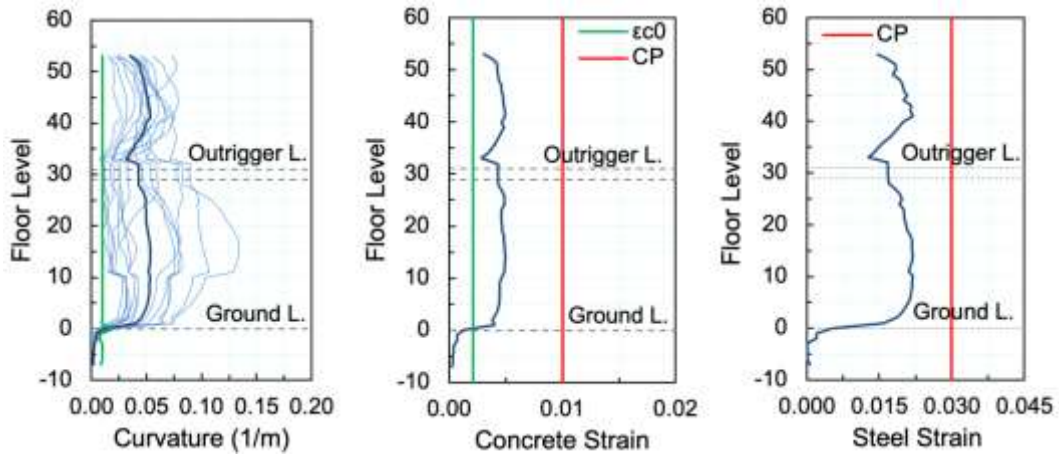

(a) (b) (c)

Figure 5.9 (a) Curvatures, (b) mean concrete strains and (c) mean steel strains in coupling beams under MCE ground motions.

5.2.2.3 Outriggers

The outrigger diagonal members were initially designed for the internal forces solely obtained under the SLE spectrum. The load combination in Eq. 3.1 was not used because the outriggers were connected to the structural system after the dead loads had been imposed on the core walls and columns. Only the superimposed dead loads and live loads were included in the design earthquake load combination. The sizes of outrigger members are simply determined in order to satisfy $\rho < 0.05$.

There are no specific design limitations for outrigger members. Categorically, they should remain linear elastic under the SLE and should not lose their axial capacity under the MCE.

Longitudinal and transverse reinforcement limits

Longitudinal reinforcement ratio of the diagonal members was limited to 0.05 to satisfy the tensile forces developed under the SLE. The maximum tensile force demand is 17,600 kN, whereas the tensile capacity of the diagonal members with 5% longitudinal reinforcement is 21,300 kN.

The longitudinal reinforcement ratios of the horizontal members of the outrigger truss system are 0.021 at the upper level (floor L31) and 0.043 at the lower level (floor L29). These horizontal members were considered as axial load resisting members rather than moment resisting members, because they receive significant amount of compression and tension transmitted from the diagonal members, whereas bending and shear actions were negligible in comparison.

Axial strain limits under MCE

The performance of the diagonal outrigger members under seven pairs of MCE ground motions is presented in Table 5.2, in terms of the mean maximum axial strain values. The maximum tensile steel strain is 0.012, which is significantly below the limiting steel strain of 0.08. The maximum compressive concrete strain is 0.0023, which is also well below the limiting value 0.020, but close to the strain at peak stress of unconfined concrete, i.e. 0.0021. These values indicate a safe design for all diagonal members.

Table 5.2 Mean maximum axial strains in diagonal outrigger members under MCE ground motions.

Outrigger	Axial Strain	
	Tension	Compression
X1-W	0.0094	-0.0021
X2-W	0.0061	-0.0014
X1-E	0.0093	-0.0012
X2-E	0.0116	-0.0017
Y1-S	0.0091	-0.0019
Y2-S	0.0097	-0.0016
Y3-S	0.0110	-0.0019
Y1-N	0.0098	-0.0023
Y2-N	0.0098	-0.0017
Y3-N	0.0099	-0.0014

Axial strains in the horizontal members of the outrigger truss system are significantly lower than the strain limits for collapse safety.

These results reveal that the SLE controls the design of the outrigger truss system. Although the maximum compressive force demand on the diagonal members is 59,100 kN under one MCE ground motion pair, it is less than the corresponding compressive load capacity of 62,500 kN. The critical buckling load is 88,700 kN.

5.2.2.4 Perimeters beams

Perimeter beams can be considered as secondary members in a tall building, which serve for a uniform distribution of the horizontal inertial forces developing in the slabs to the perimeter columns. Only limited inelastic response is expected under the MCE excitations.

Longitudinal and transverse reinforcement limits and DCR limits

The longitudinal reinforcement ratios are 0.0088 at the top and 0.0077 at the bottom, both exceeding the minimum reinforcement ratio of 0.0041. Beams remain essentially elastic under the SLE. Capacity shear controls the shear design.

Moment and shear DCRs are all below the flexural DCR limit of 1.0 and shear DCR limit of 0.7.

Axial strain limits under MCE

Curvature, tensile steel strain and compressive concrete strains under the MCE ground motions are presented in Figure 5.10, where each dot represents the maximum demand at a beam end. Although all beam ends yield, steel and concrete strains are well below the respective strain limits of 0.040 and 0.010 for collapse safety. Further, shear DCRs are all below the limiting value of 1.0. Therefore, internal forces from the SLE govern the design of perimeter beams.

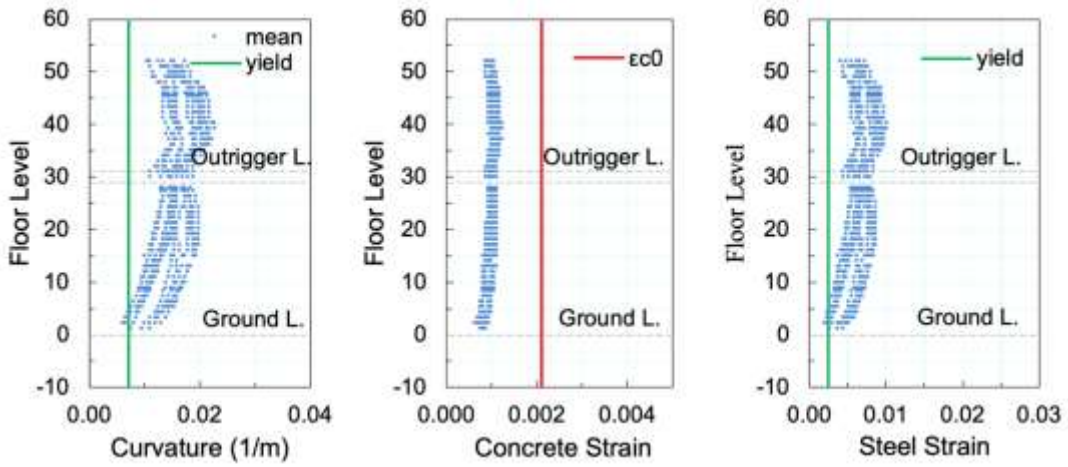

(a) (b) (c)

Figure 5.10 (a) Curvatures, (b) concrete strains and (c) steel strains in perimeter beams under MCE ground motions.

5.2.2.5 Perimeter columns

Perimeter tower columns are RC at the first seven podium stories, composite from the top podium story to the 26th story and RC again from 27th story to the top. Column design is evaluated for the column SG26 (see Figure 3.2), which receives internal design forces larger than the others.

Longitudinal and transverse reinforcement limits

The longitudinal reinforcement ratios for the column SG26 are shown in Figure 5.11a. Both the reinforcing steel in RC columns and the structural steel in composite columns satisfy the longitudinal reinforcement limits (see Section 3.3.3). The transverse reinforcement also satisfies the associated limits. Therefore, reinforcement limits do not control reinforcement design in columns.

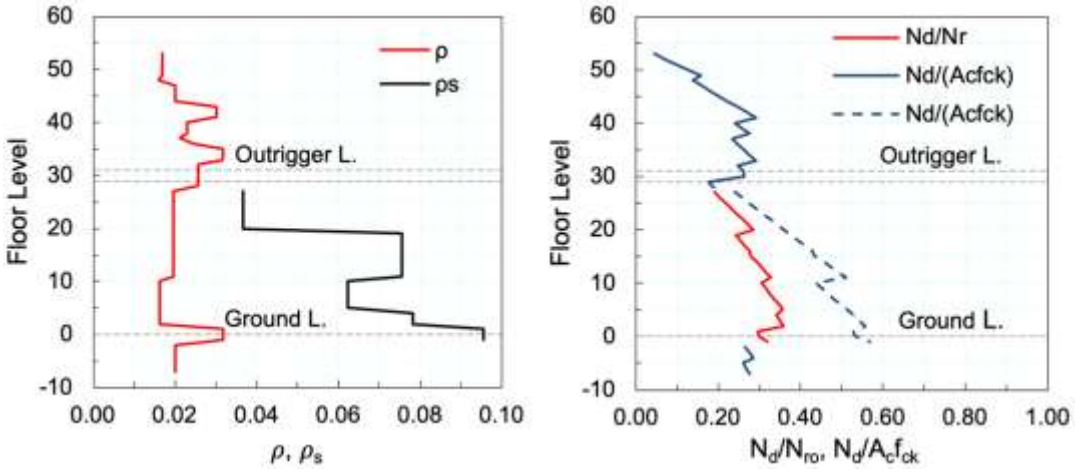

(a) (b)

Figure 5.11 (a) Reinforcement ratios and (b) axial stress ratios of column SG26.

Axial stress limits

The axial stresses developed under the design axial loads are presented in Figure 5.11b. The dashed blue line shows the axial stresses that would be developed if RC columns were used instead of composite columns at those particular stories. Hence, it is evident that the axial stress limit of 0.40 would be exceeded in the absence of composite columns at those stories. Apparently, axial stress limits control the sizes of the composite perimeter columns at the top podium story, ground story and the first floor, and their sizes were not reduced in proportion to their axial loads at the second to 26th stories. RC columns conform to the sizes of the composite columns at the lower and upper stories in order to avoid stiffness discontinuity.

DCR limits and strain limits under MCE

Moment and shear DCRs of the three columns under the SLE are shown in Figure 5.12. They satisfy the associated limits safely.

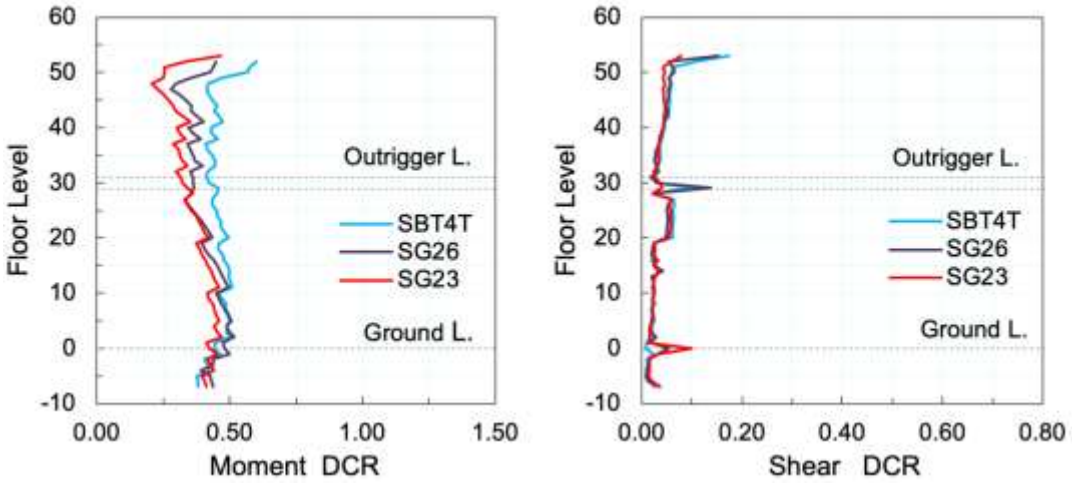

Figure 5.12 (a) Moment and (b) shear DCRs along selected columns under SLE spectrum.

Moreover, all perimeter columns in the building system remain linear elastic under the MCE ground motions. Hence, the concrete and the longitudinal steel in the perimeter columns safely satisfy the associated strain limits.

5.3 Response Parameters Controlling Seismic Performance

Following the completion of the design of the building, new seismic design codes or pertinent guidelines (e.g., LATBSDC [2020]; PEER [2017]) increased the minimum number of ground motions from seven to eleven that are used in the seismic performance evaluation of tall buildings. Moreover, ground motion pairs in set #1 would be scaled upward by large factors for the collapse analysis in incremental dynamic analysis (IDA). Hence, a new set of ground motion pairs (set #2) that were selected and scaled to match the MCE spectrum was used in the nonlinear dynamic analysis presented in this section. These new ground motion pairs were scaled upward by incrementally increasing their geometric mean spectra until collapse is achieved, which resulted in smaller SFs.

5.3.1 Service performance level under the SLE and wind

The target performance level for the building under the SLE and 50-year wind is "operational." Hence, the response should be essentially linear elastic. This is ensured by the performance limits stated in Section 3.4.1, in terms of IDRs and structural member DCRs.

As presented in Section 5.2, the wind forces control interstory drifts up to floor 30 (below the outrigger level) and the earthquake forces control above floor 30. However, IDRs are considerably below the 0.5% limit under the SLE, and reasonably below the 0.2% limit under the 50-year wind. All DCR values for the shear wall segments are well below the moment DCR limit of 1.5 and the shear DCR limit of 0.7. Respective DCR values for the peripheral columns are much lower, maximum moment DCRs around 0.6 and shear DCRs around 0.2.

A comparative graphical view of the maximum DCRs for each member type and maximum IDRs throughout the building height is presented in Figure 5.13 in a normalized form. The moment and shear DCRs are normalized with their respective limits of 1.5 and 0.7. Earthquake maximum IDRs are normalized with 0.5%, and wind maximum IDRs are normalized with 0.2%.

The response parameter that controls the service performance level of this building is apparently the maximum IDRs under the 50-year wind. On the other hand, in seismic regions with very low wind speeds, the service performance of a core wall building would be controlled by the moment and shear DCRs of the coupling beams.

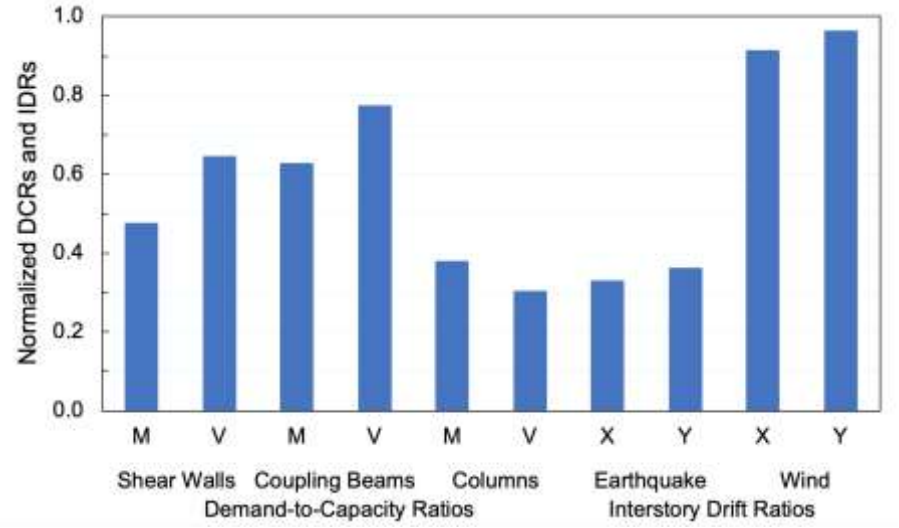

Figure 5.13 Maximum normalized DCRs (M: moment, V: shear), and IDRs under the SLE spectrum and 50-year wind loads for the most critical members.

Outriggers were employed in the investigated structural system mainly for reducing the IDRs under wind loads. However, the results displayed in Figure 5.14 indicate that this reduction is not significant. The 0.2% IDR limit for 50-year wind would have been satisfied without outriggers. This is perhaps due to the competent lateral stiffness of the core wall system, which is an outcome of imposing the stress limits indicated in Section 3.3.2. The role of outriggers might have been more prominent in the reduction of floor accelerations for comfort, but such a criterion is not imposed in tall building design [Smith 2011].

Peak horizontal acceleration at the top floor under service-level wind loads, associated with a mean recurrence interval of 10 years, was determined as 0.021 g for 2.5% damping, which is below the occupant comfort limit of 0.025 g for office buildings. In addition, according to wind tunnel test results, floor acceleration limits under the service-level wind loads would not be ensured without employing outriggers in this office building.

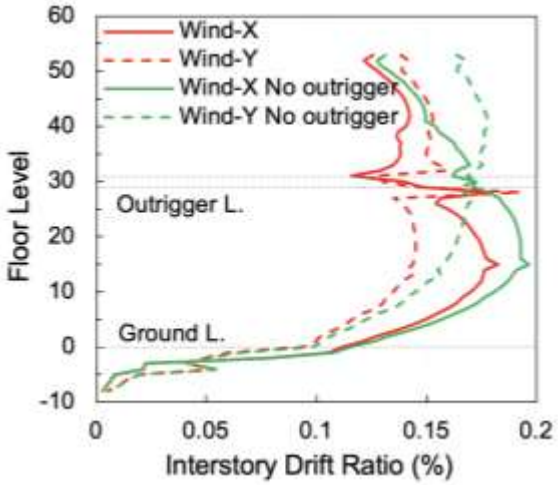

Figure 5.14 The effect of outriggers on IDRs under 50-year wind loads.

The maximum IDRs under the SLE are significantly lower than the IDR limits for service performance (Figures 5.1b and 5.13). Hence, imposing limits on IDRs is not effective at the service performance level of a tall concrete core wall system. IDR limits may be more effective on tall steel buildings.

5.3.2 Response parameters that control the safety performance level under the MCE

The target performance level under the MCE is "collapse prevention." Hence, the response under the MCE ground motions is expected to be inelastic. This target performance is satisfied if the performance limits stated in Section 3.4.2, in terms of IDRs and material strains of structural members, are not exceeded.

NTHAs were conducted under the set #2 pairs of ground motions scaled to the MCE spectrum. Damping matrix was constructed by using 2.5% Rayleigh damping ratios for the first and fifth modes. 2.5% rather than the conventional 5% damping was preferred in the NTHAs because damping matrix represents energy dissipation in linear elastic members, whereas hysteretic energy dissipation is inherently accounted by the inelastic member responses.

Figure 5.15 presents the normalized mean material strains in the most critical members and normalized IDRs at the most critical story under the MCE ground motion pairs. Mean concrete and steel strains, ε_c and ε_s, are normalized with the MCE limits of $\varepsilon_{c,\mathrm{MCE}}$ = 0.010 and $\varepsilon_{s,\mathrm{MCE}}$ = 0.030, respectively, whereas mean IDRs are normalized with 3.0%. It is worth noticing that the limiting concrete strain is equal to the ultimate strain calculated for the regularized concrete model given in Figure 3.8a. Figure 5.16 presents the normalized concrete and steel strains in shear wall segments determined under each MCE ground motion pair. Likewise, maximum IDRs can be seen in Figure 5.17, which shows the variation of maximum base shear forces (normalized with the building weight) against maximum IDRs in each direction, calculated under the SLE spectrum and MCE ground motions. Note that maximum base shear and IDR are not necessarily synchronous.

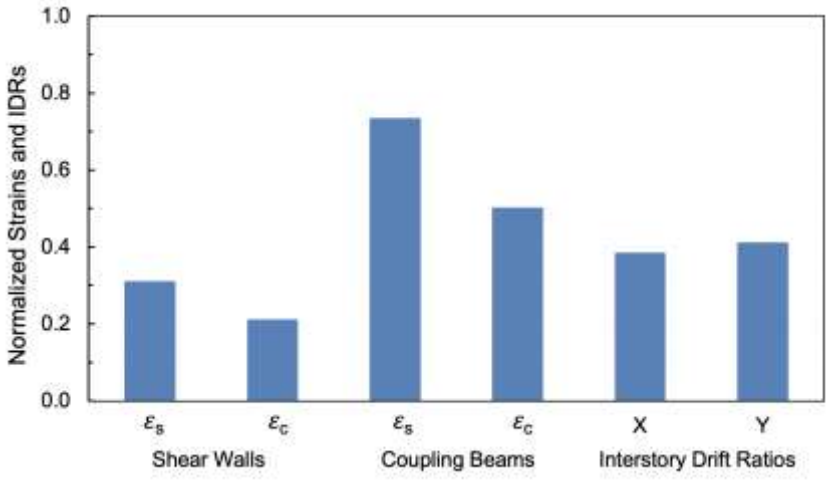

Figure 5.15 Normalized mean material strains for the most critical members and normalized IDRs under MCE ground motions.

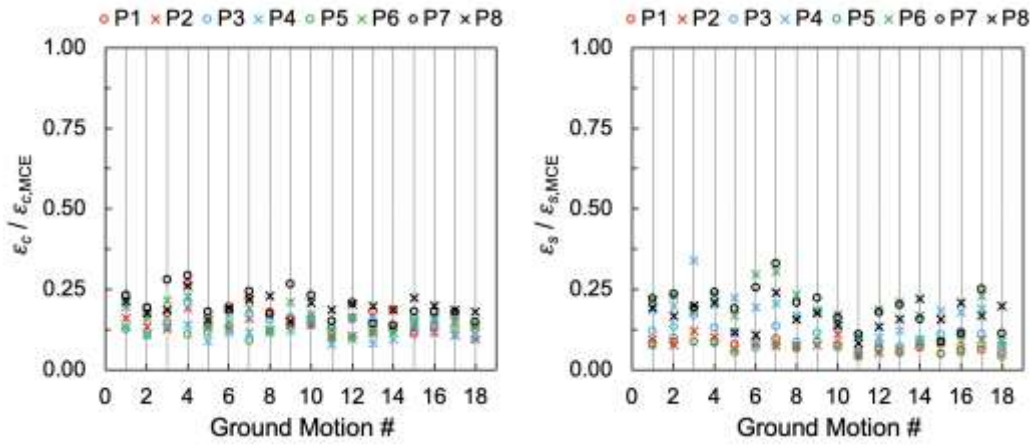

Figure 5.16 Maximum normalized concrete and steel strains in shear wall segments under MCE ground motions ($\varepsilon_{c,\mathrm{MCE}}$ = 0.010 and $\varepsilon_{s,\mathrm{MCE}}$ = 0.030).

The normalized mean material strains in shear wall segments shown in Figure 5.16 and IDRs in Figure 5.17 under the 18 MCE ground motion pairs (set #2) are quite low compared to the respective MCE limits. Shear walls are effectively at the incipient yielding state, whereas the coupling beams are purely in the yielding phase during their maximum responses under the MCE ground motions, as marked on the moment-curvature diagrams of the most critical members in Figure 5.18. The NTHAs also indicate that the peripheral columns remain linear elastic under the MCE ground motions. Therefore, Figures 5.15, 5.16 and 5.18 reveal that the safety performance level under the MCE is dominantly controlled by the tensile steel strains, and hence by the plastic curvatures of coupling beams. The mean tensile strain in the coupling beams is the product of normalized steel strain in coupling beams (0.72) from Figure 5.15 and the MCE limit for steel, $\varepsilon_{s,\mathrm{MCE}}$ = 0.030, which gives 0.022. This mean strain is about 10 times of the yield strain of S420 steel, i.e., 0.0021, which confirms that coupling beams are in the far inelastic stage under the MCE ground motions as clearly indicated in Figure 5.18b.

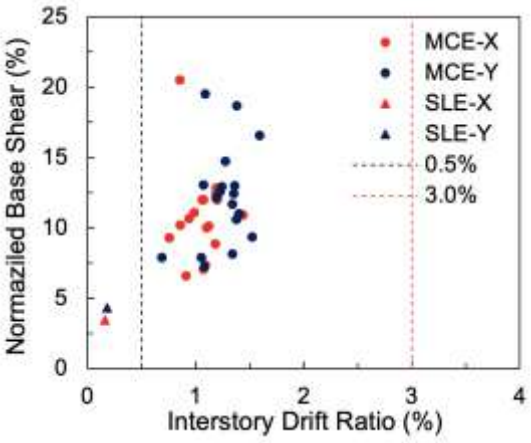

Figure 5.17 Base shear vs. maximum IDR under the SLE response spectrum and MCE ground motions.

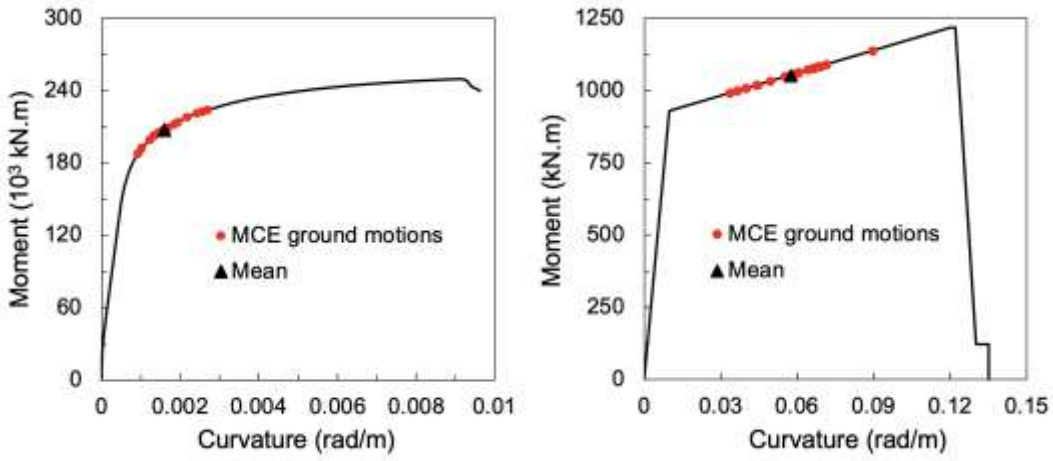

(a) (b)

Figure 5.18 Maximum curvatures at the most critical (a) shear wall (P7) and (b) coupling beam (CB2, floor 14) under MCE ground motions, marked on the moment-curvature diagrams of the respective shear wall and beam sections.

5.3.3 Response parameters that control the collapse performance

Each ground motion pair is scaled upward from the MCE level by incrementally increasing their geometric mean spectrum until collapse is achieved. Collapse occurs in two consecutive stages. In the first stage, a coupling beam fails when maximum curvature exceeds the ultimate curvature of the beam (e.g., 0.122/m for CB2 on floor 14; see Figure 5.18b). Concrete and steel strains in shear walls are far from critical

at this stage, as shown in Figure 5.19 Note that concrete and steel strains are now normalized with the ultimate limits, ε_{cu} = 0.010 and ε_{su} = 0.080, respectively. As upward scaling continues incrementally, almost all coupling beams fail before the commencement of concrete crushing at the critical shear wall fibers. The computer algorithm permits further analysis steps with zero stiffness and strength of the failed coupling beams. In the second stage, failure occurs when concrete strain at the most critical shear wall reaches the crushing strain of 0.01. Figure 5.20 shows the normalized concrete and steel strains in shear wall segments at this stage under each ground motion pair.

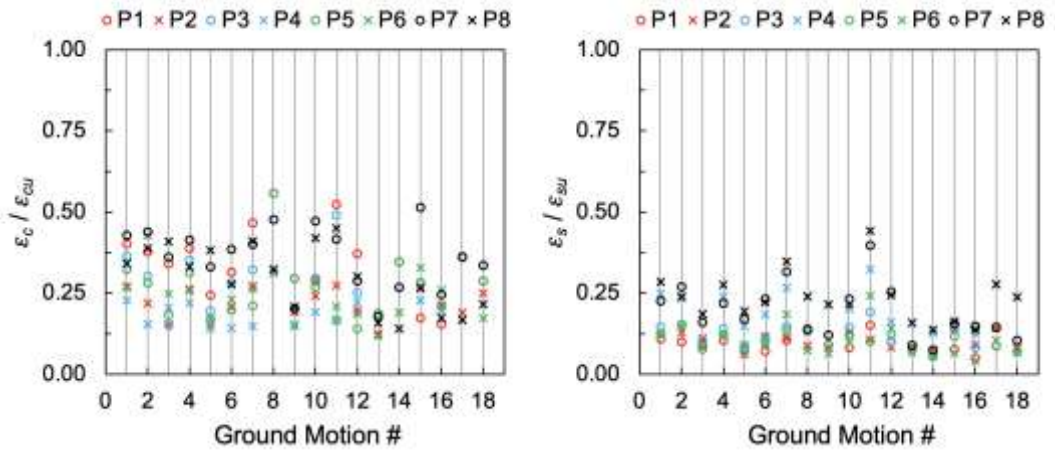

Figure 5.19 Maximum normalized concrete and steel strains in shear wall segments under 18 ground motion pairs at the instant of first coupling beam failure (ε_{cu} = 0.010 and ε_{su} = 0.080).

These two failure stages, identified with the first coupling beam failure and the first shear wall concrete crushing in Figures 5.19 and 5.20, are defined as *partial collapse* and *near collapse*, respectively. The response parameters that control these two collapse stages are the coupling beam ultimate curvatures (Figure 5.18b) or their corresponding tensile steel strains, and shear wall compressive concrete strains (Figure 5.20). The increase in concrete and steel strains from partial to near collapse states are clearly observed in Figures 5.19 and 5.20. Under each ground motion, the wall segment that reaches concrete crushing first controls ultimate failure. P1, P3 and P7 are the most controlling shear wall segments (see Figure 3.2). Along each

vertical ground motion line in Figure 5.20, as the critical wall segment approaches crushing along the degrading stress-strain segment in Figure 3.8a, the other wall segments do not follow the critical one closely, which can be attributed to the redistribution of internal stresses in the core wall.

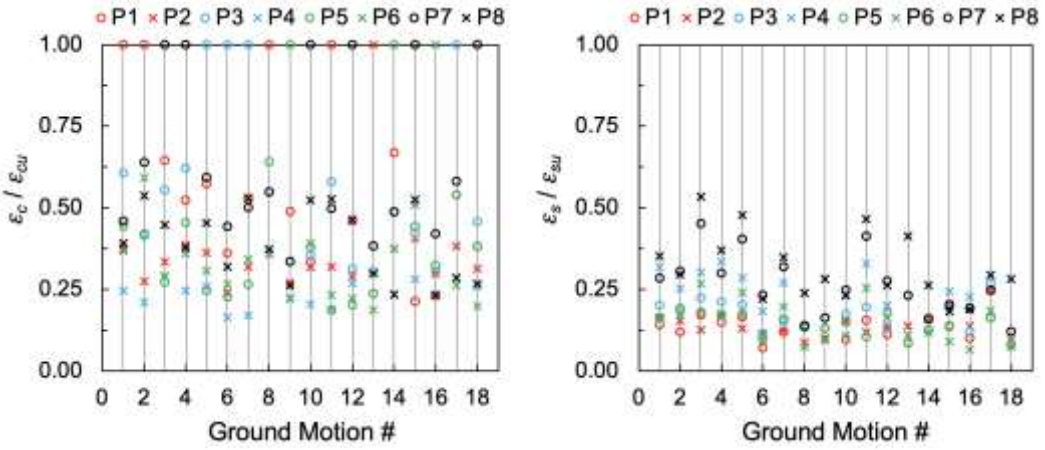

Figure 5.20 Maximum normalized concrete and steel strains in shear wall segments under 18 ground motion pairs at the instant of first shear wall failure (ε_{cu} = 0.010 and ε_{su} = 0.080).

Figure 5.21 presents the geometric mean acceleration response spectra of the ground motion pairs scaled to the first coupling beam failure (partial collapse) and first shear wall failure (near collapse) stages. Their mean spectra are named as the *partial collapse spectrum (PCS)* and *near collapse spectrum (NCS)*. Together with the mean spectrum of ground motions scaled to the MCE spectrum, they are compared in Figure 5.22a with the site specific uniform hazard spectra, which are standardized to the code spectrum format, for return periods of 43, 475 and 2475 years (i.e., the SLE, the DBE and the MCE, respectively).

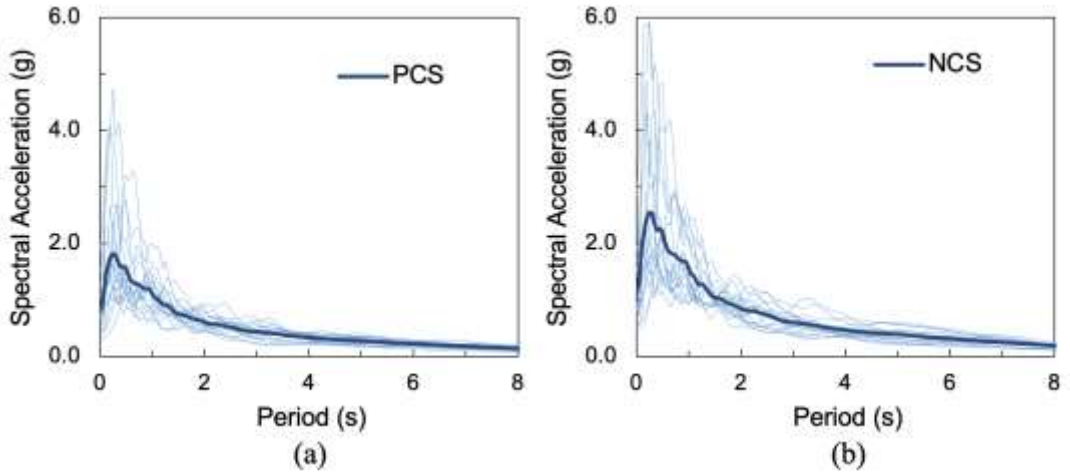

Figure 5.21 Acceleration response spectra of ground motions leading to (a**)** partial collapse and (b**)** near collapse.

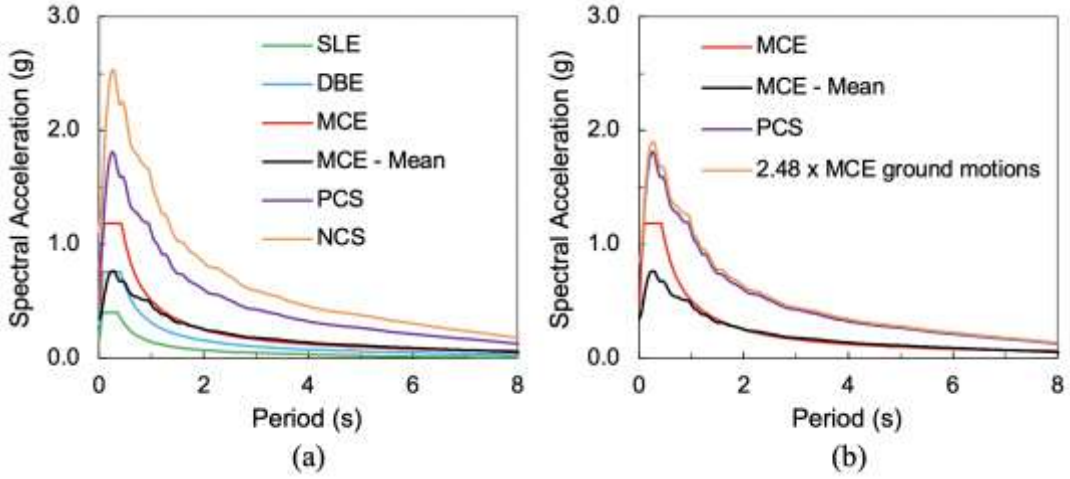

Figure 5.22 (a) Mean acceleration response spectra of MCE ground motions, partial collapse and near collapse spectra, and the standardized code spectra for 43, 475 and 2475 year return periods (b) comparison of the PCS with the scaled MCE spectrum.

5.3.4 Prediction of partial collapse spectrum from the MCE spectrum

Seismic codes and regulations for tall building design mandate NTHA under selected ground motion pairs scaled to the MCE spectrum. For the investigated tall concrete building, the moment-curvature response for the most critical coupling beam under each MCE scaled ground motion pair is readily available, as indicated in Figure

5.18b. Under the MCE ground motions, maximum curvatures are all located on the post-elastic linear segment of the moment-curvature diagram. As the intensity of each ground motion is incrementally increased, the associated curvature point moves away from the MCE point on the post elastic linear segment until it reaches the ultimate curvature capacity of the coupling beam. The inelastic mechanism of the building does not change between these two limit states, i.e., the critical coupling beam and all others are in the post-elastic "linear" state while the shear wall members are at the incipient inelastic response state (Figure 5.18a). This stable linearity from MCE to partial collapse under each ground motion for the most critical coupling beam, i.e., the one that reaches the failure state first, motivates searching for the similarity of the ratio of ground motion scale factors, and the ratio of absorbed plastic energies between the MCE and partial collapse states.

The ratio of PCS to MCE spectrum, both given in Figure 5.22b, is very stable along the period axis, with a mean value of 2.35 and almost with no dispersion. The ratio of absorbed plastic energies under the post-elastic linear moment-curvature segment in Figure 5.18b for a unit plastic hinge length, from yield to the MCE curvature and from yield to the end of the linear post-elastic segment, i.e., 0.122/m at incipient collapse, can be calculated for each ground motion. Their mean value is 2.48, which is sufficiently close to the spectrum scale factor 2.35 with a mere 5% difference. Consequently, if the MCE spectrum is scaled by 2.48, the PCS can be closely estimated without carrying out an incremental dynamic analysis for each ground motion. This is a significant economical saving in estimating collapse. The estimated PCS is displayed in Figure 5.22b and compared with the actual PCS.

It should be noted that a similar scaling cannot be applied to the MCE spectrum for obtaining the NCS, because the inelastic mechanism of the building changes significantly between the partial collapse state (coupling beam collapse) and the near collapse state (shear wall collapse).

Figure 5.23 shows the seismic hazard curve in terms of $S_a(T_1)$ that is constructed [Cornell et al. 2002] using the available hazard data for the building site (41.0812°N,

29.0096°E; Soil Group ZC; AFAD 2018b), which include hazard levels with mean recurrence intervals, T_r = 43, 72, 475 and 2475 years. Mean $S_a(T_1)$ for the ground motions that will lead to partial and near collapse of the building, i.e., 0.21g and 0.31g, respectively, cf. Figure 5.21, are entered into the constructed hazard curve. The return periods of the mean partial and near collapse ground motions are estimated as 12000 and 27000 years, respectively.

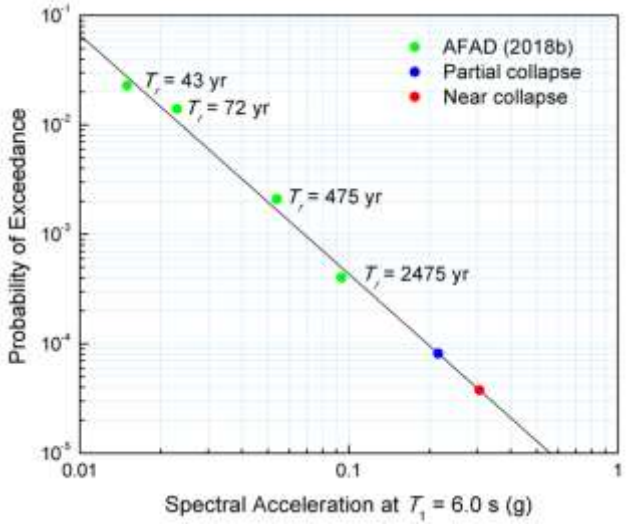

Figure 5.23 Seismic hazard curve for the building site.

5.4 Summary

Factors controlling the seismic design of a tall building system were identified by evaluating the results of rigorous analysis under the SLE and MCE load combinations, with due consideration of project specific design limits. These limits are:

- Maximum interstory drift limits under the SLE, wind and MCE
- Maximum DCR limits under the SLE and MCE
- Minimum reinforcement limits under the SLE
- Maximum axial stress limits under the SLE
- Maximum axial strain limits under the MCE

It has been observed that the structure-related factors, i.e. interstory drift limits under the SLE, wind and MCE, do not control the seismic design at all for a tall core wall building with outriggers. However, the role of outriggers is crucial in this outcome. The outrigger trusses employed for deformation control under wind loading also contribute to overstrength, although to a lesser extent. In addition, floor acceleration limits under the wind loads would not be satisfied without employing outriggers in this building. The axial load limit of 0.25 for the core walls would also not be satisfied without outriggers.

The role of member-related factors on the seismic design has been summarized in Table 5.3, for each member type separately. Apparently, the SLE dominates the seismic design. It should also be noted that the axial stress limits, which dominate the dimensions of vertical members, and capacity shear forces for the shear design of frame members are also determined under the SLE spectrum. The only exception is the shear design of the core walls, where the MCE excitations govern the design shear forces. The main reason for this exception is shear amplification. The term "architecture" in Table 5.3 implies that the widths of the coupling beams conform to the wall thickness, and their depths conform to the dimensions of the door openings in the wall. The widths of the perimeter beams conform to the column widths, whereas their depths are constant.

Table 5.3 Factors controlling seismic design of structural members.

Member Type	**Dimensions**	**Reinforcement**		
		Flexural	**Shear**	**Axial**
Core wall segments	Axial stress limit	SLE	MCE	-
Coupling beams	Architecture	SLE	Capacity shear	-
Outrigger members	SLE	-	-	SLE
RC columns	Axial stress limit	SLE	Capacity shear	-
Composite columns	Axial stress limit	SLE	Capacity shear	-
Perimeter beams	Architecture	SLE	Capacity shear	-

The investigated tall building displays remarkable performance under seismic actions. It remains linear elastic under the SLE and displays limited damage performance under the MCE ground motions. Significant inelastic actions occur only at the coupling beams and particular sections of the core walls where ductile flexural response is ensured. The core walls reach the yield state at two critical sections (Figure 5.7) and the coupling beams yield in flexure at several floors (Figure 5.9) under the MCE, which indicate that the seismic design is effective and efficient. Perimeter columns and outrigger struts do not undergo inelastic action under the SLE, which conform to the basic design objectives.

Safety and partial collapse limit states are controlled by the flexural response limits of coupling beams, whereas near collapse limit state is controlled by the concrete strain limits at the confined shear wall end regions.

The basic reason behind such favorable seismic performance is the overstrength in design from various sources. The variation of maximum base shear force against maximum interstory drift ratios are plotted in Figure 5.17 in each direction, calculated under both the SLE spectrum via response spectrum analysis and under the MCE ground motions through nonlinear response history analysis. Maximum base shear and interstory drift are not necessarily synchronous. An overstrength ratio can be defined in both directions, as the maximum ratio of the MCE to SLE base shear demands. These are 5.8 and 4.6 in the X and Y directions, respectively. Both factors are about twice the overstrength factors suggested in ASCE 7-16 [ASCE 2017a] for ordinary concrete buildings.

The main sources of overstrength in the seismic design of this tall concrete core wall building are simply,

- at the system level: employing outriggers for deformation control
- at the member level: axial stress limitations on vertical members

The inherent overstrength in seismic design reduces the damage risk and increases the seismic performance, which comes at a cost that can be considered negligible

when compared to the large investment cost of a tall building. It has to be considered that tall buildings, which are designed to meet the current performance based guidelines, have not yet been tested under extreme earthquake ground motions. Hence, the resulting overstrength cannot be regarded as the outcome of an over-conservative design.

The annual frequency of the mean earthquake ground motion that will lead to collapse reduces from the target value of $4 \cdot 10^{-4}$ (1/2475) defined for the MCE for ordinary buildings, to $8 \cdot 10^{-5}$ (1/12000) for partial collapse, and to $4 \cdot 10^{-5}$ (1/27000) for near collapse of the tall core wall building. However, this safety increase cannot be regarded as a waste of resources. It comes at a cost that can be considered negligible when compared to the large investment cost of a tall building. It has to be considered that tall buildings, which are designed to meet the current performance based guidelines, have not yet been tested under extreme earthquake ground motions.

A modest contribution of this chapter is the direct estimation of ground motions leading to partial collapse from the MCE ground motions through a simple scaling procedure introduced herein for tall RC buildings. The primary lateral load resisting system of tall RC buildings is a core wall composed of wall segments connected with coupling beams. The introduced procedure utilizes the segmental linearity of the moment-curvature response of coupling beams along the post-yield branch. As the intensity of ground motions increase during incremental dynamic analysis, plastic curvatures of coupling beam plastic hinges increase linearly from the MCE level to the upward-scaled intensity of the MCE ground motion until the collapse of the most critical coupling beam occurs (partial collapse state). Accordingly, the SF for each ground motion leading to partial collapse can be obtained as the ratio of the absorbed plastic energies under the moment-curvature backbone curve at the ultimate curvature state and that at the MCE curvature state. Such scaling eliminates the need for conducting many NTHAs for establishing partial collapse depicted by the failure of coupling beams.

CHAPTER 6

SEISMIC FRAGILITY ANALYSIS

6.1 Introduction

This chapter derives structure-specific and member-specific seismic fragility curves for different limit states of the building and investigates the effect of ASI on structural response and seismic fragilities. Three different sets of seismic fragility curves are derived for structural and non-structural components of the building. IDR_{max} of the building and maximum plastic rotation ($\theta_{p,max}$) of the most critical coupling beam were selected as the demand measures for the fragilities for structural components, whereas maximum PFA (PFA_{max}) was selected as the demand measure for the fragilities for non-structural components. The seismic IM was selected as the first mode geometric mean spectral acceleration, $S_{a,gm}(T_1 = 6.0\text{ s})$, where T_1 was based on the linear elastic finite element model of the building. Finally, the effect of ASI on the seismic fragility curves was examined when IDR_{max} was the structural demand measure.

That the case study building in this study is an existing building with a parallelogram footprint, its dynamic properties were determined from an in-situ ambient vibration test and these dynamic properties were reproduced with the 3-D linear elastic finite element model of the building, which was the basis for its 3-D nonlinear finite element model, distinguishes this study from previous studies on seismic fragility analysis of tall buildings.

6.2 Seismic Fragility Formulation and Framework

Seismic fragility is defined as the probability of reaching limit states or performance levels as a function of a seismic IM. Seismic fragility is the conditional probability that the structural capacity, C, fails to resist the structural demand, D, given the seismic intensity, SI, and is computed using a lognormal CDF [Ellingwood et al. 2007]:

$$P[C < D|SI = x] = 1 - \Phi\left[\frac{ln(\hat{C}/\hat{D})}{\sqrt{\beta_{D|SI}^2 + \beta_C^2 + \beta_M^2}}\right] \quad (6.1)$$

where $\hat{C}$ is the median structural capacity related to the limit state, $\hat{D}$ is the median structural demand, $\beta_{D|SI}$ is the aleatoric uncertainty in demand (due to record-to-record variability), β_C is the aleatoric uncertainty in capacity and β_M is the epistemic (modeling) uncertainty.

Aleatoric uncertainties are based on factors that are inherently random in nature and cannot be reduced by improving the available approaches. Epistemic uncertainties, on the other hand, are knowledge-based, stemming from the lack of knowledge in the analysis of the system, and can be reduced with additional information or more comprehensive analysis [Celik and Ellingwood, 2010b].

β_M varies from 0.1 to 0.3 for tall buildings in the literature. Zhang and He [2020] determined β_M as 0.11 in seismic collapse risk assessment of a 118-story super-tall building. Mwaft [2012] assumed β_M as 0.3. β_M was assumed as 0.2 in this study based on the assumption that the developed model yields a prediction of the structural response that, with 90% confidence, is within $\pm 30\%$ of the actual value [Wen et al. 2004; Celik and Ellingwood 2010b; Jayaram et al. 2012; Shome et al. 2015].

Figure 6.1 shows the key steps in deriving the seismic fragilities for structural when IDR is used as the structural demand measure, which are presented subsequently in

this chapter. In structural analyses, material properties were considered as deterministic, hence their mean values were used.

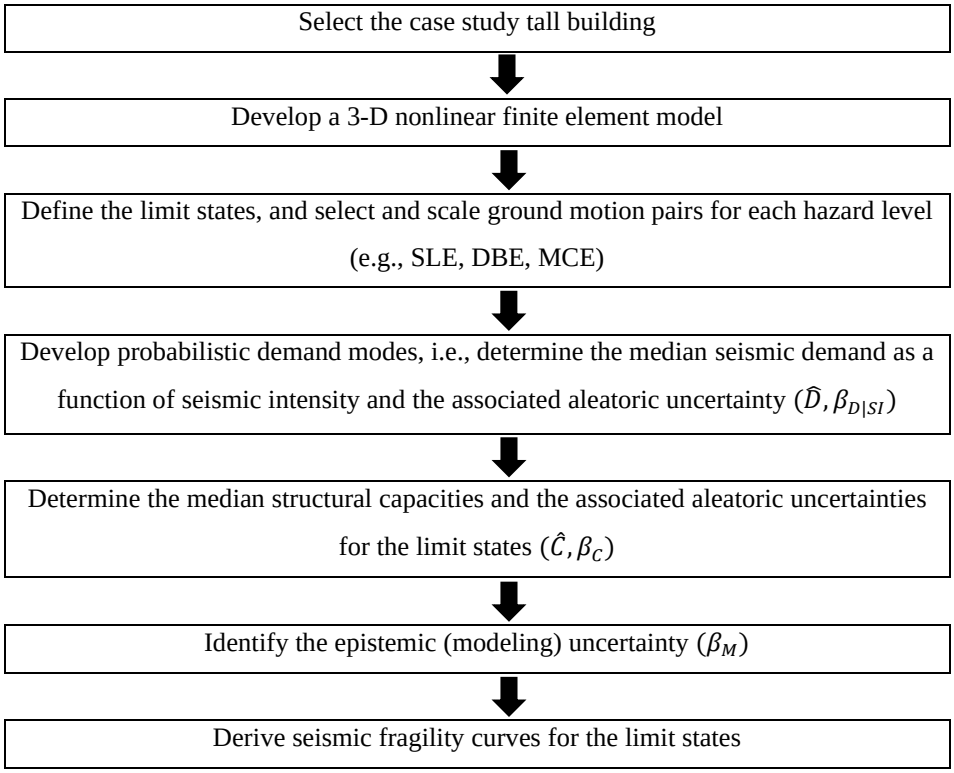

Figure 6.1 Seismic fragility framework.

6.2.1 Probabilistic seismic demand model

Structural demand versus seismic intensity relationship can be determined by either stripe or cloud analysis. In stripe analysis, NTHAs are performed only at some specific hazard levels (e.g., SLE, DBE and MCE hazard levels) by scaling selected ground motions to those intensity levels to determine the seismic demand. The demand is represented by a separate lognormal probability density function at each hazard level. On the other hand, in cloud analysis, NTHAs are performed for all selected ground motions to determine the seismic demand over a range of seismic intensity levels. The median demand is represented by a log-linear function of seismic intensity. The demand is considered to be distributed lognormally about the median with constant logarithmic standard deviation.

In this study, the seismic performance of the building was evaluated through NTHAs using the selected SLE, DBE and MCE ground motion pairs presented in Chapter 3 (sets #1–4). Cloud analysis was used to develop the probabilistic seismic demand models, which represent D as a function of SI [Cornell et al. 2002]:

$$D = aSI^b\varepsilon \tag{6.2}$$

where ε is a lognormal random variable with median 1.0 and logarithmic standard deviation $\sigma_{ln\varepsilon} = \beta_{D|SI}$ depicting the uncertainty in the dependence of D on SI [Celik 2007]. The parameters a and b were determined by linear regression of $\ln(D)$ on $\ln(SI)$ obtained from NTHAs, while $\beta_{D|SI}$ was calculated by

$$\beta_{D|SI} = \sqrt{\frac{1}{n-2}\sum_{i=1}^{n}[\ln(D_i) - \ln(aSI_i^b)]^2} \tag{6.3}$$

where n is the number of (D, SI) data points.

6.2.2 Limit States

The seismic fragility curves were derived for four limit states in this study: Immediate Occupancy (IO), Life Safety (LS), Partial Collapse Prevention (PCP) and Near Collapse Prevention (NCP). The IO limit state is identified by the limit below which the building can be occupied safely without significant damage. Chapters devoted particularly to tall buildings in seismic design codes [AFAD 2018a], or pertinent guidelines (e.g., LATBSDC [2020], PEER [2017]) also specified the IO limit state such that the structural and non-structural elements of the building must continue their general functionality. Minor post-yield deformations are permitted for ductile structural elements. Accordingly, the IO limit state was defined as the instant when the first coupling beam (or a group of coupling beams) starts to undergo inelastic response in IDA. The LS limit state was defined such that the building can sustain moderate damage but still remains in safe zone against collapse. PCP and

NCP limit states were defined by the first coupling beam (or a group of coupling beams) failure and the first shear wall concrete crushing, respectively. Their limit values were determined from the statistical analyses of the results of IDA, which used MCE ground motions pairs (set #2) incrementally scaled upward until collapse was achieved. $\hat{C}$ and β_C values associated with the limit states were calculated by using statistical analyses employing the rank-ordering method.

6.3 IDR-Based Seismic Fragility Curves for Structural Components

Due to the parallelogram floor plans of the building, the IDRs in the Y′ direction (parallel to the local axis of the structural and non-structural walls in that direction), not the Y direction, were calculated together with the IDRs in the X direction.

6.3.1 Probabilistic seismic demand models

Figure 6.2 presents the seismic demands in terms of $IDR_{\max}$, which are given in the X and Y′ directions, respectively, by the probabilistic demand models:

$$IDR_{max} = 5.7S_{a,gm}^{0.76}, \beta_{D|SI} = 0.41 \quad (6.4)$$

$$IDR_{max} = 6.3S_{a,gm}^{0.75}, \beta_{D|SI} = 0.43 \quad (6.5)$$

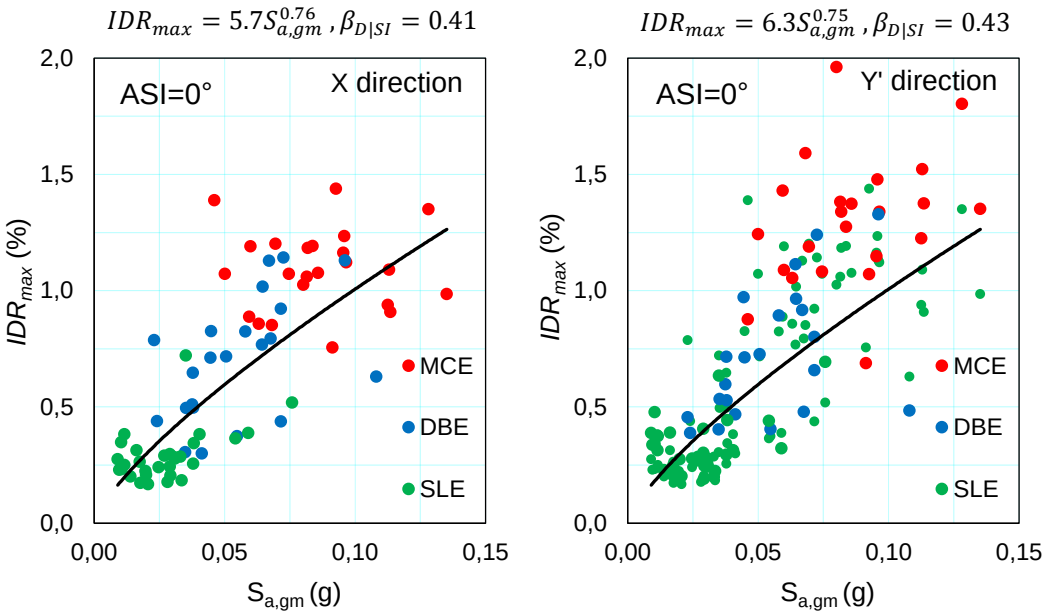

(a) (b)

Figure 6.2 Seismic demands in the (a) X and (b) Y′ directions.

6.3.2 Structural capacity models

The IO limit state was defined by the IDR_{max} values prior or subsequent to yielding of a coupling beam (or a group of coupling beams) for each ground motion pair in the IDAs. $\hat{C}$ and β_C values are calculated from statistical analysis of these IDR_{max} values using the rank-ordering method. It is assumed that IDR_{max} values are lognormally distributed, which is consistent with the fragility formulation. Figure 6.3 presents the statistical analysis of the yield drift limit data, where $\phi^{-1}(i/N + 1)$ is the inverse standard normal CDF evaluated at the cumulative probability of the ith ranked yield drift limit out of N such drift limits. The ordinate of the linear regression line when $\phi^{-1}(\,)$ is zero is the natural logarithm of $\hat{C}$, while the slope is its β_C (the aleatoric uncertainty in capacity) [Celik 2007]. $\hat{C}$ and β_C values are calculated as 0.44% and 0.22 in the X direction, and 0.51% and 0.21 in the Y′ direction, respectively.

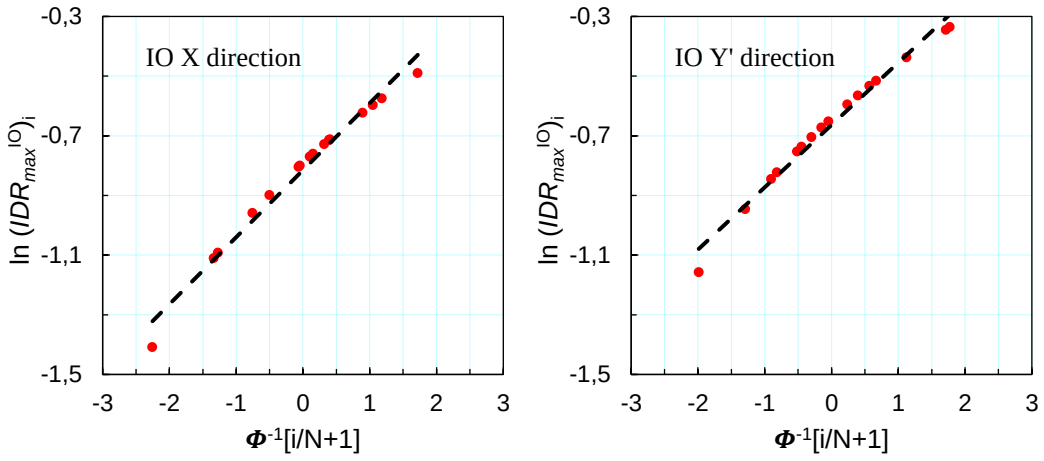

(a) (b)

Figure 6.3 The rank-ordering method for the IO limit states in the (a) X and (b) Y′ directions.

Limiting IDR_{max} values for the LS limit state are not specified for tall buildings in seismic codes and pertinent guidelines [AFAD 2018a; PEER 2017; LATBSDC 2020]. $\hat{C}$ associated with the LS limit state was assumed as 2% IDR_{max} [MPWS 2007; FEMA 2000] and β_C as 0.30 [Wen et al. 2004] in this study.

$\hat{C}$ and β_C values associated with the PCP limit state are calculated as 2.4% and 0.20 in the X direction, and 2.8% and 0.21 in the Y′ direction, respectively (see Figure 6.4).

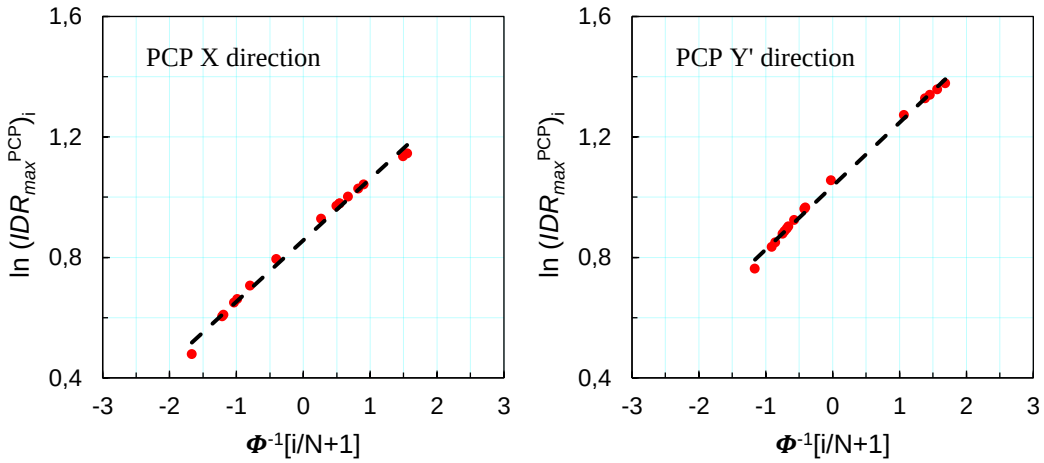

(a) (b)

Figure 6.4 The rank-ordering method for the PCP limit states in the (a) X and (b) Y′ directions.

$\hat{C}$ and β_C values associated with the NCP limit state are calculated as 3.0% and 0.20 in the X direction, and 3.4% and 0.24 in the Y′ direction, respectively (see Figure 6.5).

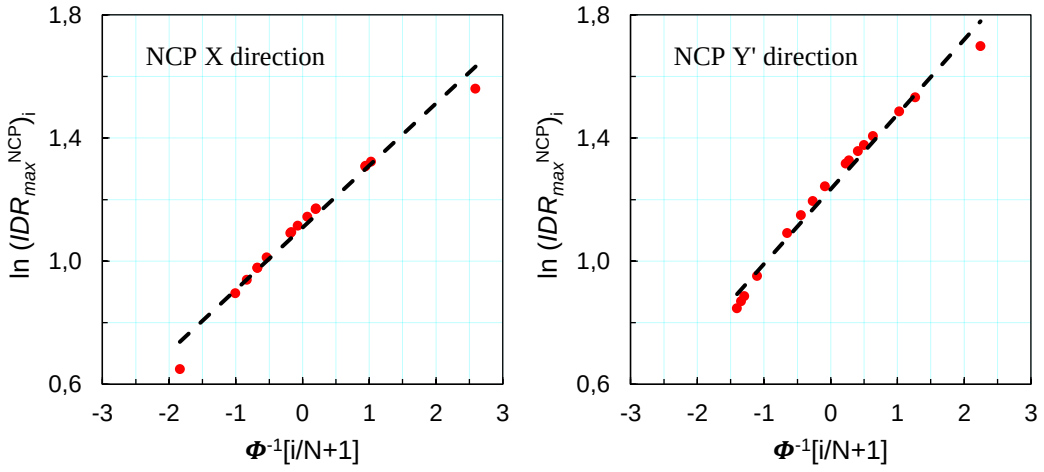

(a) (b)

Figure 6.5 The rank-ordering method for the NCP limit states in the (a) X and (b) Y′ directions.

These $\hat{C}$ values for the PCP and NCP limit states in this study are compared with collapse prevention limit states in the literature. Ji et al. [2007a; 2007b; 2009] and Pejovic and Jankovic [2016] underestimate, whereas AFAD [2018a], LATBSDC

[2020] and PEER [2017] overestimate the collapse drift capacity. However, these limits are building specific for tall buildings. More studies are needed before making any generalizations.

6.3.3 Fragility curves

Table 6.1 summarizes all the fragility function parameters. Total uncertainty (both epistemic and aleatoric) can be calculated as 0.51, 0.55, 0.50 and 0.50 for the IO, LS, PCP and NCP limit states, respectively. The mean IDR-based seismic fragility curves for the IO, LS, PCP and NCP limit states are illustrated in Figures 6.6 and 6.7 for the X and Y′ direction, respectively.

Table 6.1 Summary of the fragility function parameters.

		X direction	Y' direction
Demand			
a		5.73	6.32
b		0.76	0.75
$\beta_{D\|SI}$		0.41	0.43
Capacity		(%)	(%)
$\hat{C}$	IO	0.44	0.51
	LS	2.0	2.0
	PCP	2.4	2.8
	NCP	3.0	3.4
β_c	IO	0.22	0.21
	LS	0.30	0.30
	PCP	0.20	0.21
	NCP	0.20	0.24
Modeling			
β_M		0.20	

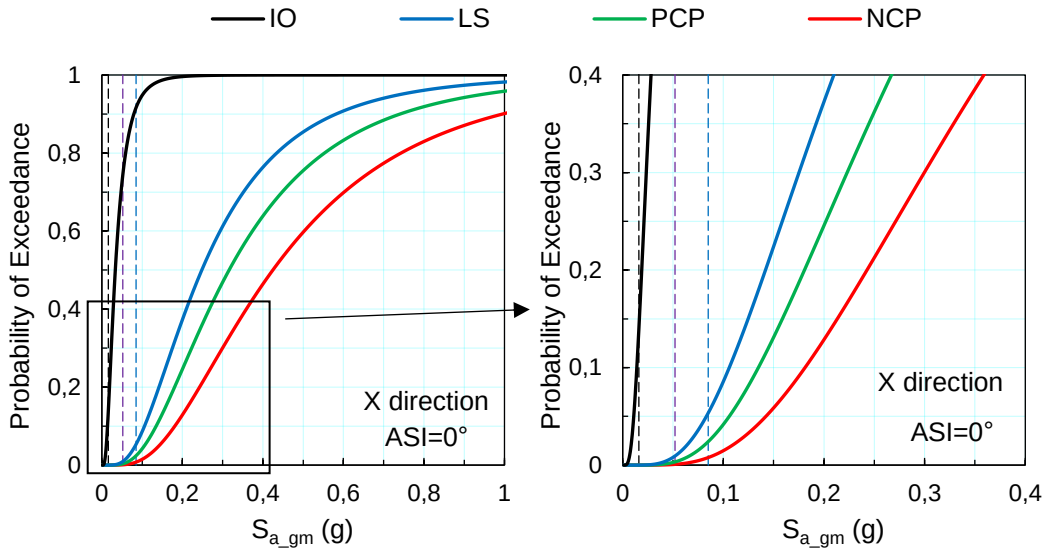

Figure 6.6 Seismic fragility curves of the building for the X direction (dashed lines represent the $S_{a,gm}(T_1)$ values corresponding to the SLE, DBE and MCE hazard levels in increasing order).

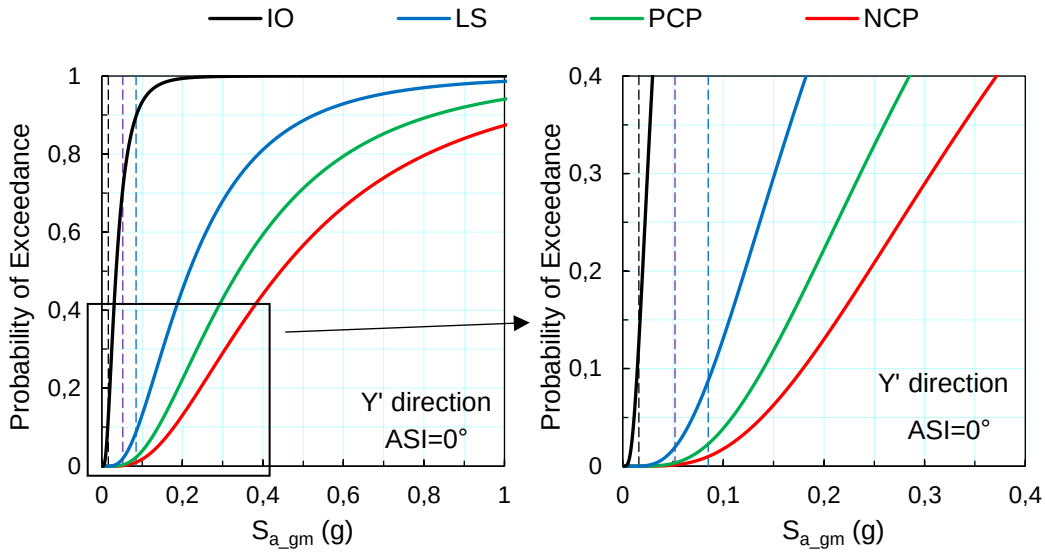

Figure 6.7 Seismic fragility curves of the building for the Y′ direction (dashed line color code defined in Figure 6.6).

Tables 6.2 and 6.3 present the probabilities of exceeding the limit states in the X and Y′ directions. At the MCE hazard level, there are 92%, 6%, 3% and 0% probabilities that the building will exceed the IO, LS, PCP and NCP limit states in the X direction,

respectively. The probabilities are 90%, 9%, 3% and 0% in the Y′ direction, respectively. The partial collapse probability of the building is quite small (3%) and the near collapse probability is none. At the DBE hazard level, the probability that the building will exceed the LS limit state is also quite small (1–2%). On the other hand, there is 13–14% probability that the building will exceed the IO limit state at the SLE hazard level. It is possible to increase the capacity of the coupling beams for a better performance under the SLE excitations.

Table 6.2 Probabilities of exceeding the limit states in the X direction.

Hazard Level	$S_{a,gm}$ (g)	Probability of exceeding the limit states (%)			
		IO	LS	PCP	NCP
SLE	0.02	14	0	0	0
DBE	0.05	74	1	0	0
MCE	0.09	92	6	3	0

Table 6.3 Probabilities of exceeding the limit states in the Y′ direction.

Hazard Level	$S_{a,gm}$ (g)	Probability of exceeding the limit states (%)			
		IO	LS	PCP	NCP
SLE	0.02	13	0	0	0
DBE	0.05	71	2	0	0
MCE	0.09	90	9	3	0

6.4 Plastic Rotation-Based Seismic Fragility Curves for Structural Components

The mean plastic rotation-based seismic fragility curves of the building were derived by considering the most critical coupling beam (i.e., CB2 on floor L14; see Figure 3.2). $\theta_{p,max}$ was selected as the seismic demand measure and $S_{a,gm}$ was selected as the seismic IM. Figure 6.8 presents the seismic demands in terms of $\theta_{p,max}$, which are given by the probabilistic demand model:

$$\theta_{p,max} = 23.4S_{a,gm}^{0.98}, \beta_{D|SI} = 0.41 \quad (6.6)$$

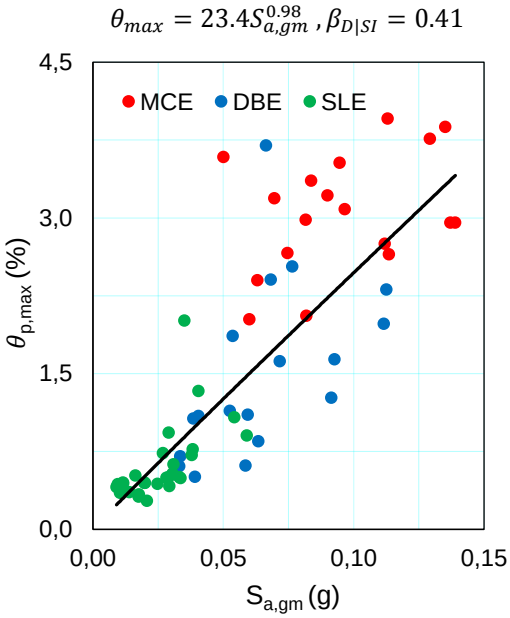

Figure 6.8 Seismic demand on the most critical coupling beam.

The seismic fragility curves were derived for three limit states: IO, LS and PCP. $\hat{C}$ associated with the IO and PCP limit states were set to the yield and plastic rotation capacities of the coupling beam, respectively, which were determined from its moment-curvature relationship based on median material properties [AFAD 2018a]. $\hat{C}$ associated with the LS limit state was taken as 75% of the $\hat{C}$ for the PCP limit state [AFAD 2018a; ASCE 2017b]. β_C for all limit states were assumed as 0.3. Table 6.4 summarizes all the parameters used in deriving the mean plastic rotation-based seismic fragility curves of the building, which are illustrated in Figure 6.9.

Table 6.5 presents the probabilities of exceeding the limit states defined for the coupling beam. At the MCE hazard level, there are 98%, 8% and 3% probabilities that the coupling beam will exceed the IO, LS and PCP limit states, respectively. At the DBE hazard level, the probability that the coupling beam will exceed the LS limit state is insignificant (1%). On the other hand, there is 19% probability that the coupling beam will exceed the IO limit state at the SLE hazard level. It is possible

to increase the capacity of the coupling beams for a better performance under the SLE excitations.

Table 6.4 Summary of the fragility function parameters.

		X Direction
Demand		
a		23.4
b		0.98
$\beta_{D\|SI}$		0.41
Capacity		(%)
$\hat{C}$	IO	0.67
	LS	4.50
	PCP	6.00
β_c	0.30	
Modeling		
β_M	0.20	

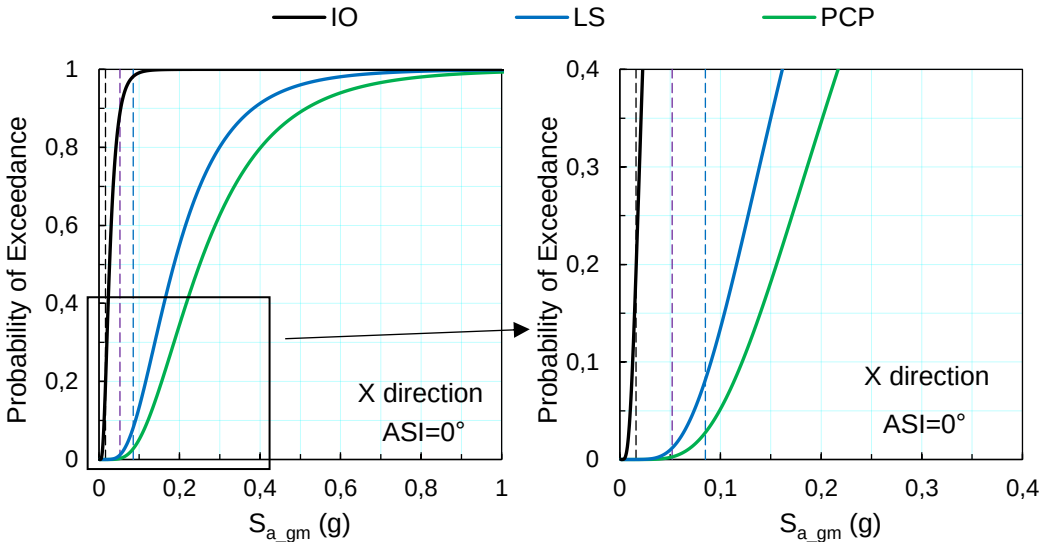

Figure 6.9 Plastic rotation-based seismic fragility curves of the building (dashed line color code defined in Figure 6.6).

Table 6.5 Probabilities of exceeding the limit states defined for the coupling beam.

Hazard Level	$S_{a,gm}$ (g)	Probability of exceeding the limit states (%)		
		IO	LS	PCP
SLE	0.02	19	0	0
DBE	0.05	88	1	0
MCE	0.09	98	8	3

6.5 PFA-Based Seismic Fragility Curves for Non-Structural Components

In seismic risk assessment of buildings, damage to structural as well as non-structural components needs to be quantified. Non-structural components are especially important in seismic loss prediction studies. The non-structural systems in buildings contain a broad variety of architectural, mechanical and electrical components that can be categorized as either "drift-sensitive" (e.g., non-load bearing partition walls, exterior curtain walls) or "acceleration-sensitive" components (e.g., suspended ceilings, HVAC systems). PFA is commonly used as the seismic demand parameter for non-structural component evaluations. Figure 6.10 presents the in-structure amplification factors (PFA/PGA) under the SLE, DBE and MCE ground motion pairs.

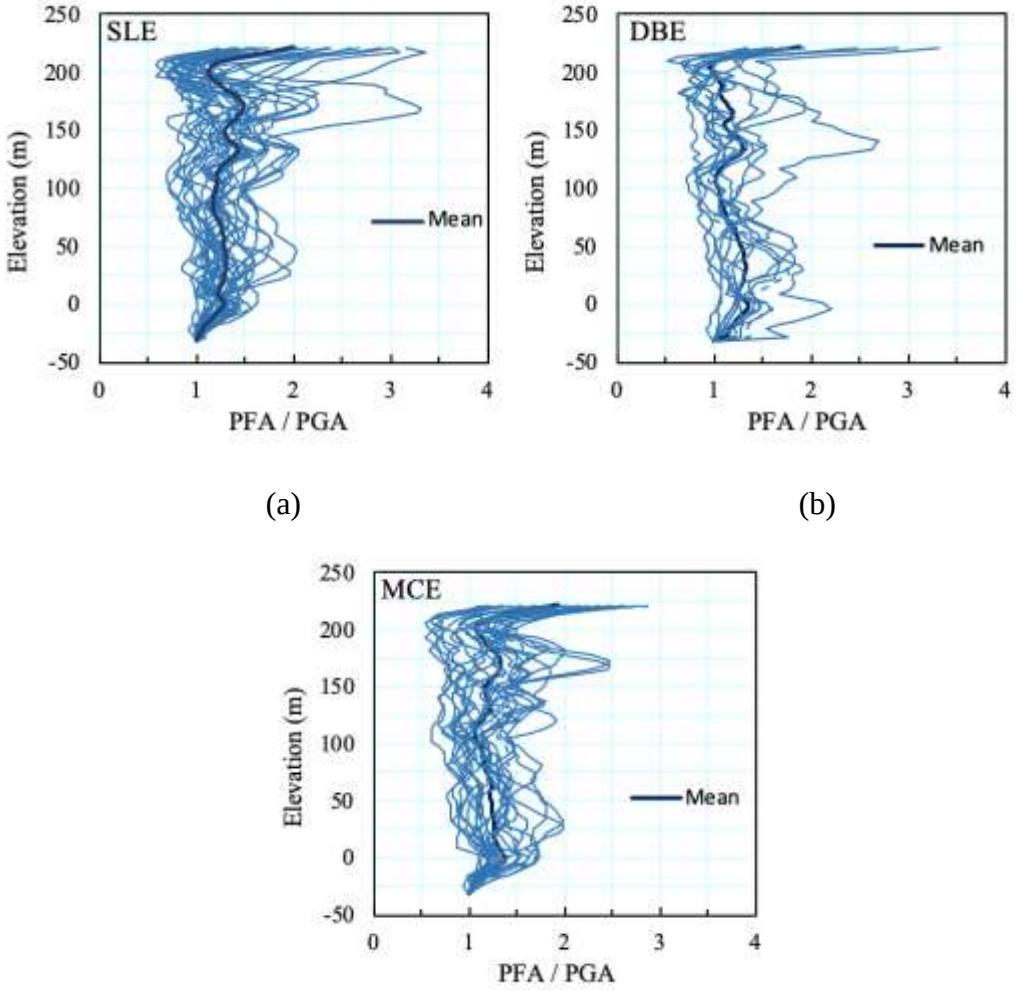

Figure 6.10 In-structure amplification factors under the (a) SLE, (b) DBE and (c) MCE ground motion pairs.

Figure 6.11 presents the seismic demands in terms of PFA_{max} as a function of PGA for different floors, which are represented by the probabilistic demand models given in Table 6.6.

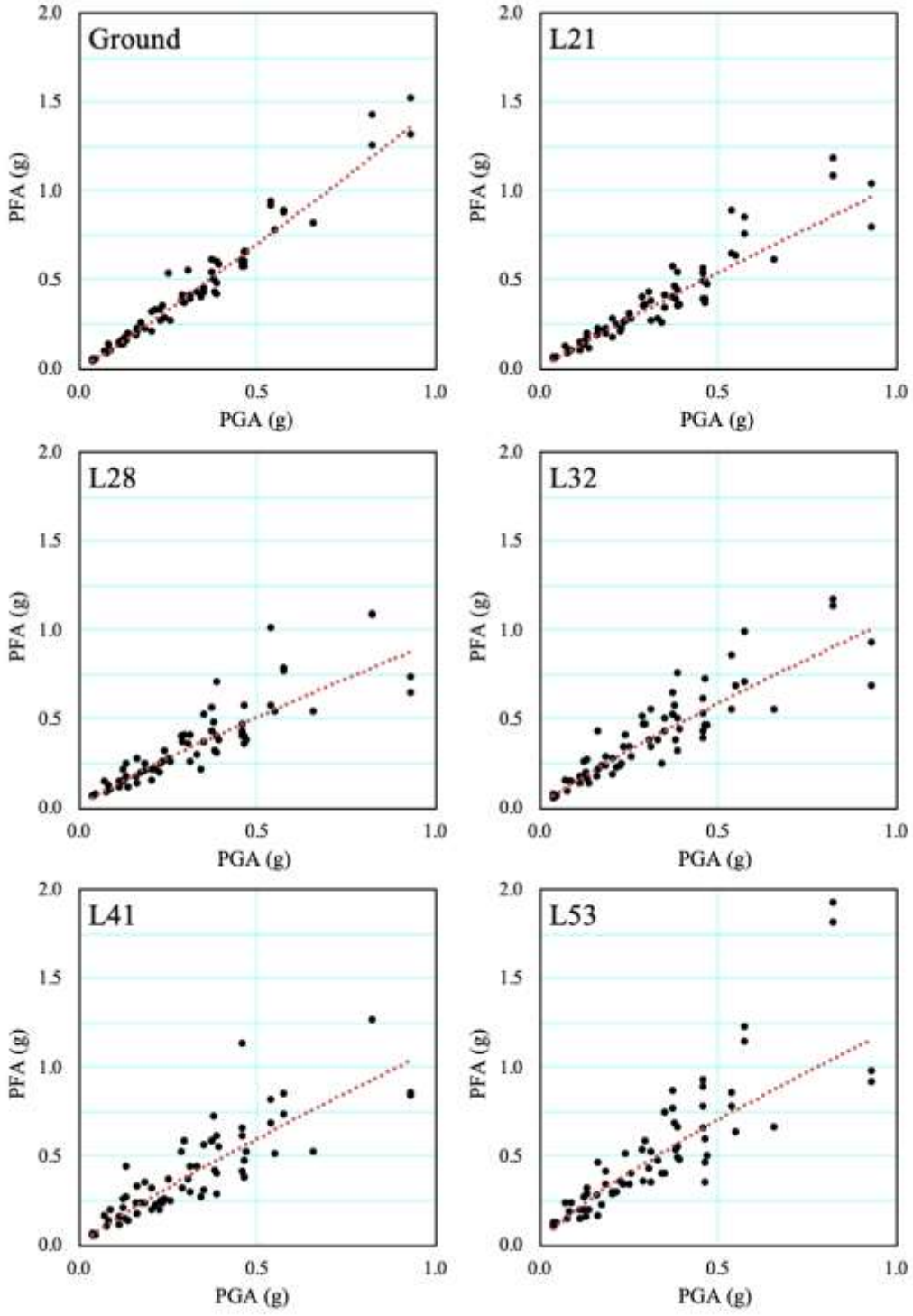

Figure 6.11 Seismic demands for different floors.

Table 6.6 Probabilistic demand models for different floors.

Floor	Median Demand	$\beta_{D\|SI}$
Ground	$PFA_{max} = 1.47PGA^{1.08}$	0.14
L21	$PFA_{max} = 1.03PGA^{0.94}$	0.19
L28	$PFA_{max} = 0.93PGA^{0.87}$	0.24
L32	$PFA_{max} = 1.07PGA^{0.86}$	0.25
L41	$PFA_{max} = 1.11PGA^{0.88}$	0.32
L53	$PFA_{max} = 1.22PGA^{0.80}$	0.28

The PFA-based seismic fragility curves were derived for the selected floors. An attempt was made to create a catalog for acceleration-sensitive components. Four different levels of $\hat{C}$ were considered: 50%, 100%, 150% and 200% of the PGA at the SLE hazard level (0.4 g). β_C was assumed as 0.3. The fragility curves derived for these four limit states are presented in Figures 6.12 and 6.13. Ground and top floors are more vulnerable than other floors. These fragility curves can be used to determine the probabilities of exceeding the capacities of acceleration-sensitive non-structural components, if known, under the expected seismic hazard levels.

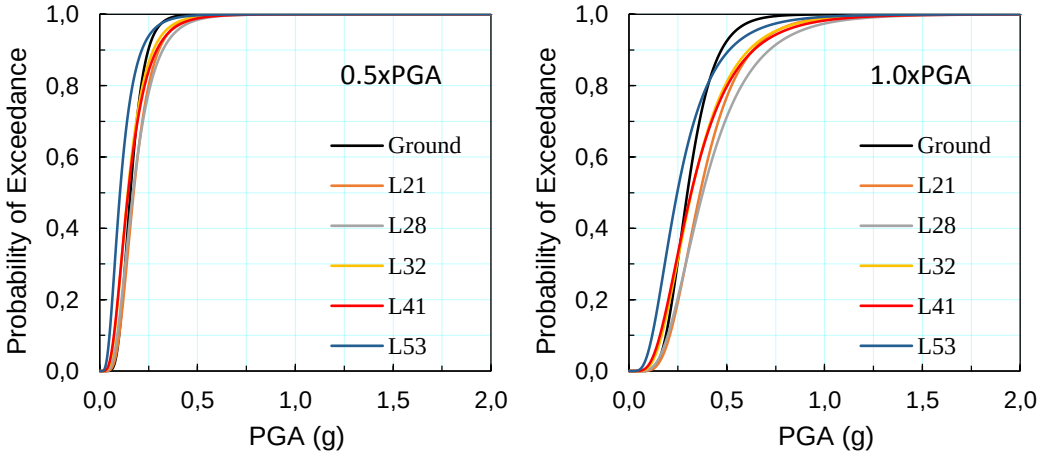

Figure 6.12 PFA-based seismic fragility curves of the building.

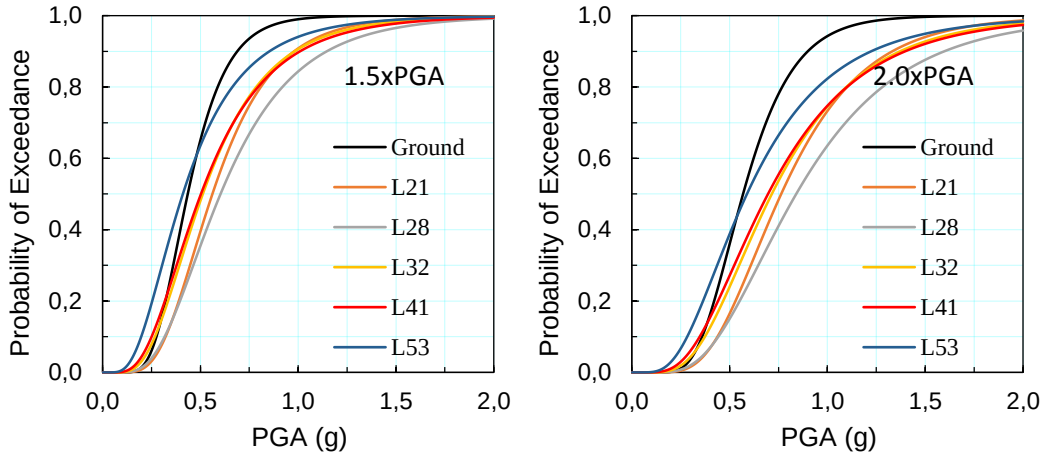

Figure 6.13 PFA-based seismic fragility curves of the building.

6.6 The Effect of ASI on Seismic Fragility Curves

The uncertainty related to the ASI arises from the fact that the principle direction of a structural system axes with regard to the position of fault ruptures is unknown. In addition, the critical angle for a given response parameter varies with dynamic properties of the structure, types of model and the level of nonlinear response of the structure. Accordingly, the ASI of the input ground motion pairs may affect the performance assessment and damage state of the building based on nonlinear deformation results. Accordingly, the performance evaluation and design validation of the structures designed to undergo nonlinear deformations should be ideally conducted with bi-directional ground motion series imposed at several angles in accordance with the principal orientations of the structures.

The principal orientation of the building is defined as X and Y (see in Figure 3.2). The design and performance assessment of the building was performed with respect to this global axis. However, interstory drift ratio at the Y′ direction was used when deriving the drift-based seismic fragility curves due to parallelogram shape of the building. This definition is more realistic and reliable to assess probability assessment of the building. This part of the study examines the effect of the ASI

(α) on structural analysis and on way of accounting for this effect on the seismic fragility relationships. Further, it is aimed to define the most critical angle of building that gives the highest response under ground motion pairs.

3-D nonlinear modeling and analysis of tall building are computationally demanding particularly under various input ground motions. The fragility analysis results show that the record to record variability is so high, hence the identification of the most critical ASI on the structural response is a hard task by using nonlinear dynamic analysis. For the definition of critical ASIs before starting seismic fragility analysis, a set of nonlinear dynamic analysis considering various angles $(0^{\circ}, 20^{\circ}, 45^{\circ}, 60^{\circ}, 90^{\circ}110^{\circ}, 135^{\circ}, 150^{\circ}, 180^{\circ})$ were performed by using the first set of ground motion (set #1). As stated previously, this ground motion set was used during the design and performance assessment of the building, hence the design and performance assessment of the building are verified by using this ground motion set. Figure 6.14 illustrates the IDR results over the height of building when the building is subjected seven bi-directional ground motion pairs along different ASI. each pair represents the result obtained from a different ground motion pair. The results show that the variability due to ASI is high and IDRs vary with the change of ASI. Further, the results also show that there is no meaningful correlation between ASI when the ground motion pair is changed.

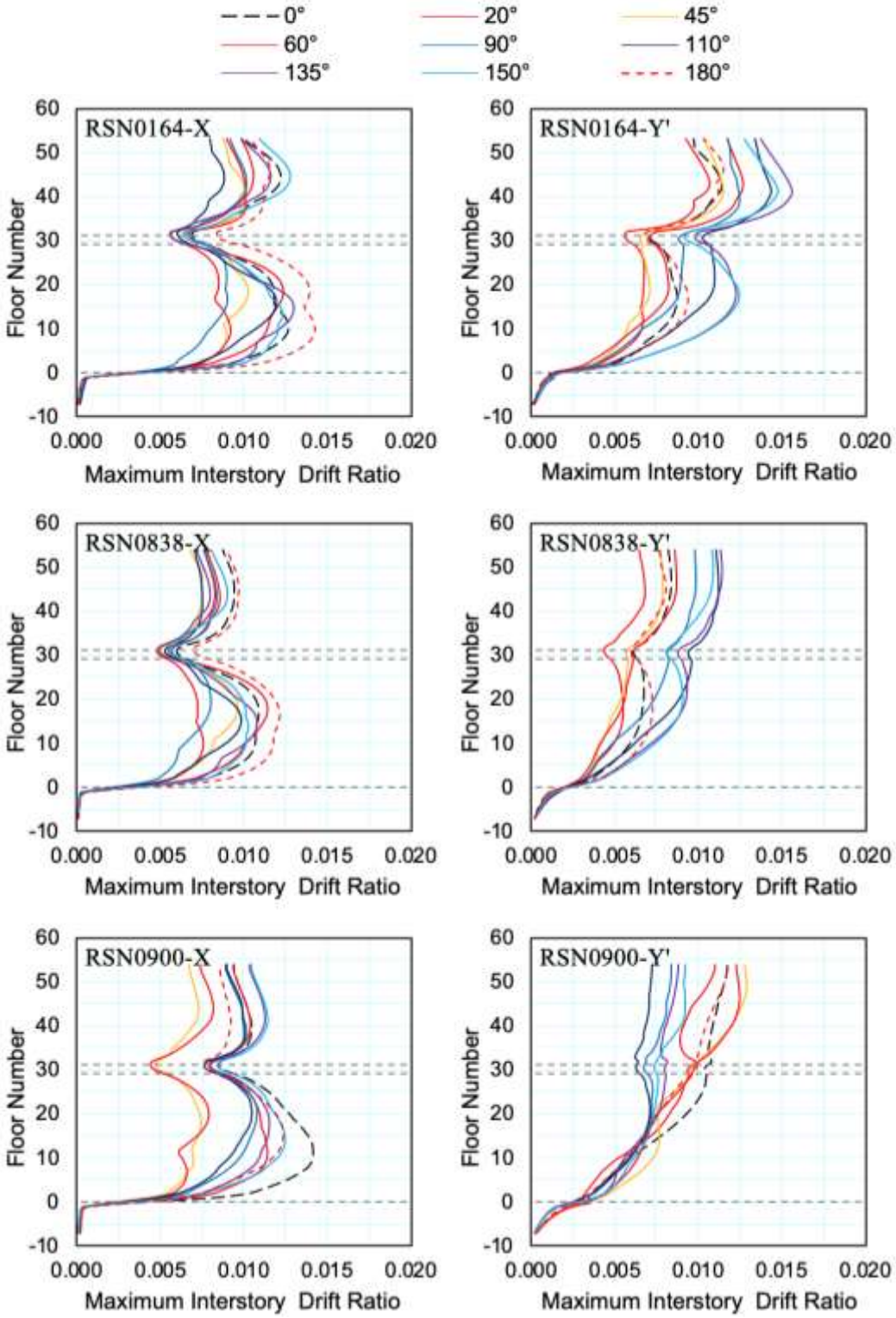

Figure 6.14 Interstory drift ratios obtained for selected ASIs under different ground motion pairs.

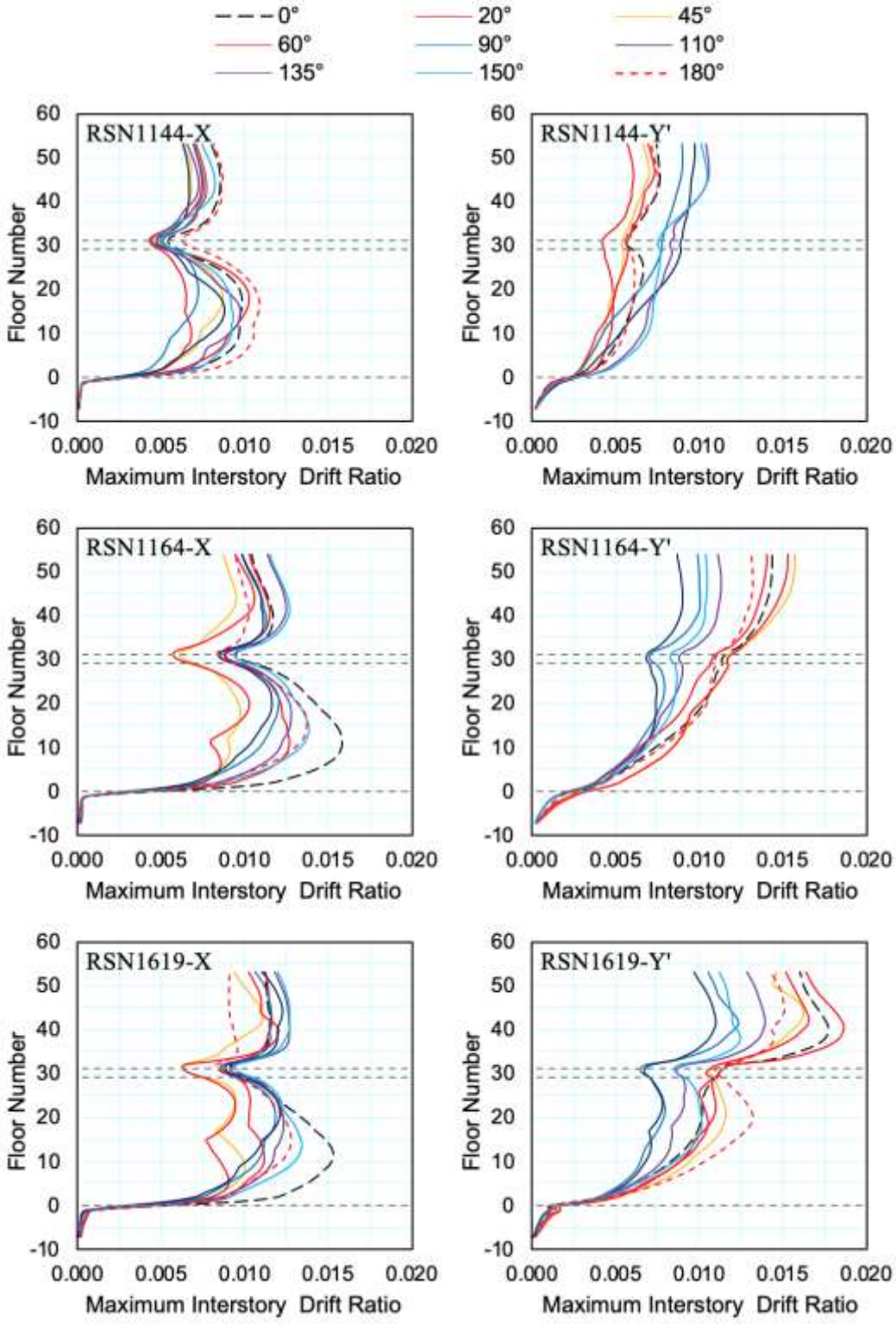

Figure 6.14 Interstory drift ratios obtained for selected ASIs under different ground motion pairs (continued).

Figure 6.15 presents the maximum plastic rotation of coupling beam CB2 (see in Figure 3.2) over the building height from selected two ground motion pairs only, RSN0838 and RSN0900 (see Table 3.5). Similar to drift results, the variability in the result of maximum plastic rotation of coupling beams is high. Further, the results also show that there is no significant correlation between ASI and the obtained results when the ground motion pair is interchanged. However, due to reducing the number of ASI for seismic fragility analysis (e.g., reducing computational demand), some of ASIs can be selected with respect to all obtained results and the requirements in seismic codes [AFAD 2018a] and pertinent guidelines [LATBSDC 2020; PEER 2017]. Seismic codes and pertinent guidelines already require analysis at 0° and 180°. In addition, when all of the results obtained for set #1 ground motion pairs were examined, the angles that were found to be more critical in ground motion pairs were selected as $0°, 20°, 45°$ and 180° for seismic fragility analysis.

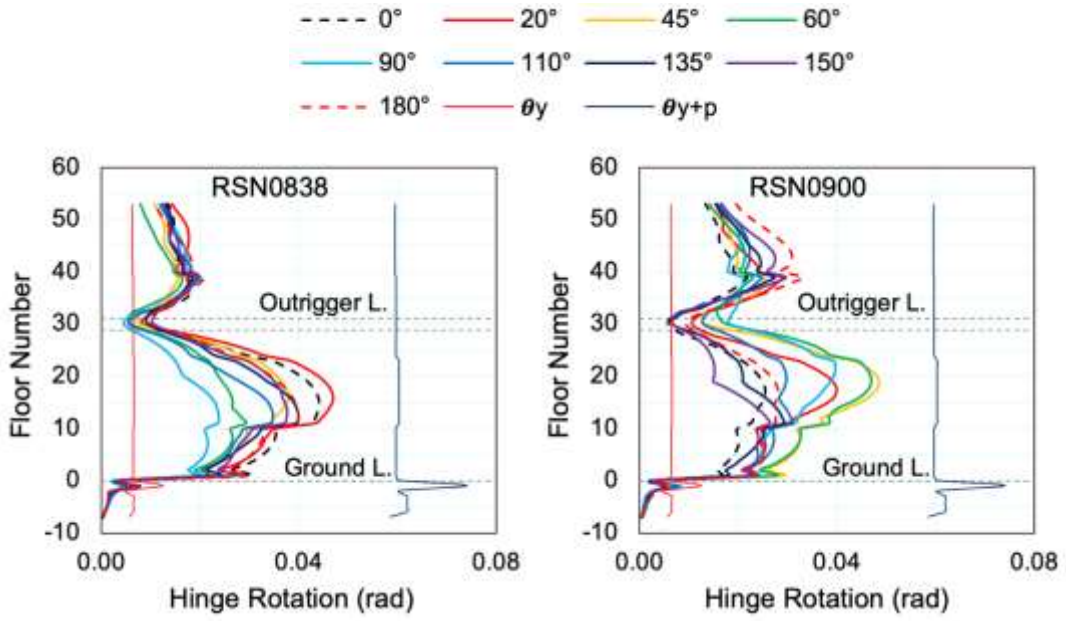

Figure 6.15 Maximum plastic rotation of coupling beam CB2 over the building height for selected ASI under different ground motion pairs.

Figures 6.5, 6.16, 6.17 and 6.18 present the relationship between seismic demand with seismic intensity when ASI is taken as $0°, 20°, 45°$ and 180°, respectively.

Table 6.7 summarizes all probabilistic seismic demand parameters for selected ASI used in the drift-based fragility formulation.

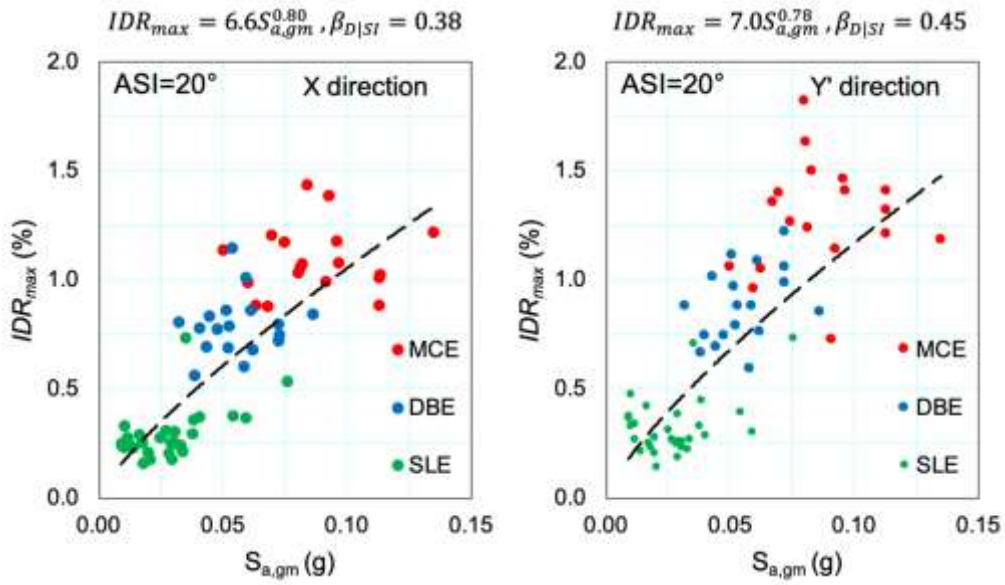

(a) (b)

Figure 6.16 Seismic demand in the (a) X direction and (b) Y` direction under selected ground motion pairs when ASI is 20º.

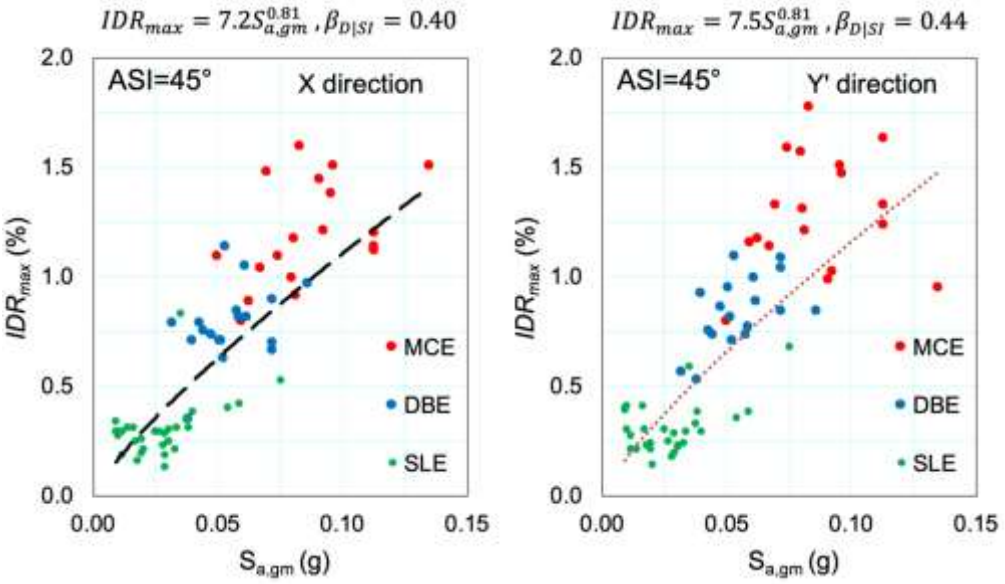

(a) (b)

Figure 6.17 Seismic demand in the (a) X direction and (b) Y′ direction under selected ground motion pairs when ASI is 45º.

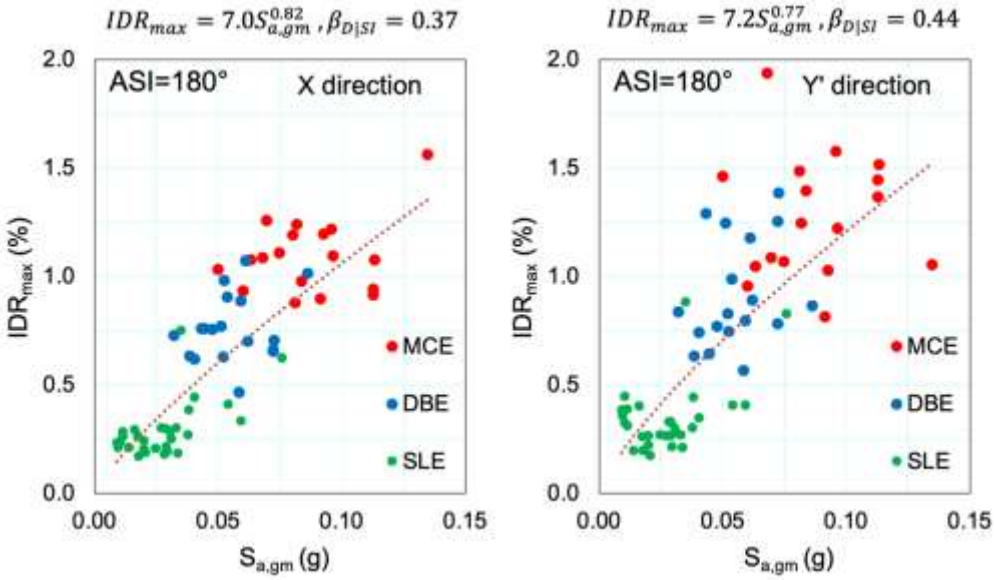

(a) (b)

Figure 6.18 Seismic demand in the (a) X direction and (b) Y′ direction under selected ground motion pairs when ASI is 180º.

Table 6.7 Probabilistic demand models for different ASIs.

	X - Direction		Y′- Direction	
ASI	Demand Model	$\beta_{D\|SI}$	Demand Model	$\beta_{D\|SI}$
0º	$IDR_{max} = 5.73S_{a,gm}^{0.76}$	0.41	$IDR_{max} = 6.31S_{a,gm}^{0.75}$	0.43
20º	$IDR_{max} = 6.57S_{a,gm}^{0.80}$	0.38	$IDR_{max} = 7.01S_{a,gm}^{0.78}$	0.45
45º	$IDR_{max} = 7.22S_{a,gm}^{0.81}$	0.40	$IDR_{max} = 7.54S_{a,gm}^{0.81}$	0.44
180º	$IDR_{max} = 6.96S_{a,gm}^{0.82}$	0.37	$IDR_{max} = 7.18S_{a,gm}^{0.77}$	0.44

Figure 6.19 presents the comparison of the demand curves obtained from cloud analysis for each ASI. The results show that the most critical angle in the X and Y′ direction is obtained as 45º and 180º, respectively, since the largest IDR_{max} is obtained in that direction if only seismic demand is considered. The results also demonstrated that applying bi-directional ground motion pairs only along the

principal axis of the building (when ASI is 0º) underestimates the maximum interstory drift ratio demand when compared to those obtained in other ASI especially when seismic intensity increases. On the other hand, the uncertainties due to demand in the Y′ direction is bigger than that in the X direction. In addition, the effect of ASI on the uncertainties in demand is less.

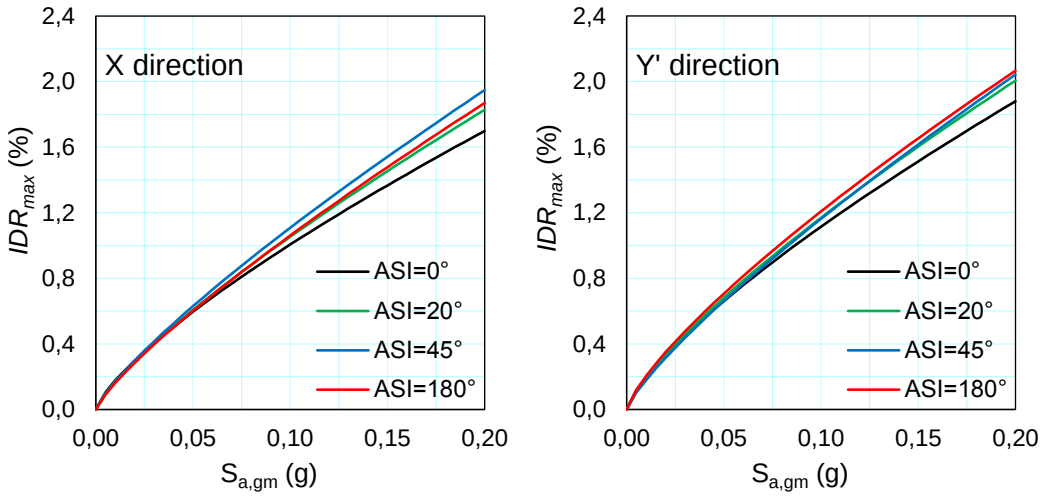

(a) (b)

Figure 6.19 Comparison of seismic demand curves for different ASI.

The effect of ASI on the structural capacity and the uncertainty in capacity is assumed as similar to the results obtained from incremental dynamic analysis when ASI is taken as 0º. The mean drift-based seismic fragilities with different ASI for each performance levels of the building are derived by employing the above probabilistic seismic fragility modeling, presented in Eq. 6.1. The comparison developed for mean drift-based seismic fragilities for each ASI for each performance level are illustrated in Figures 6.20–6.23 in the X and Y′ direction, respectively.

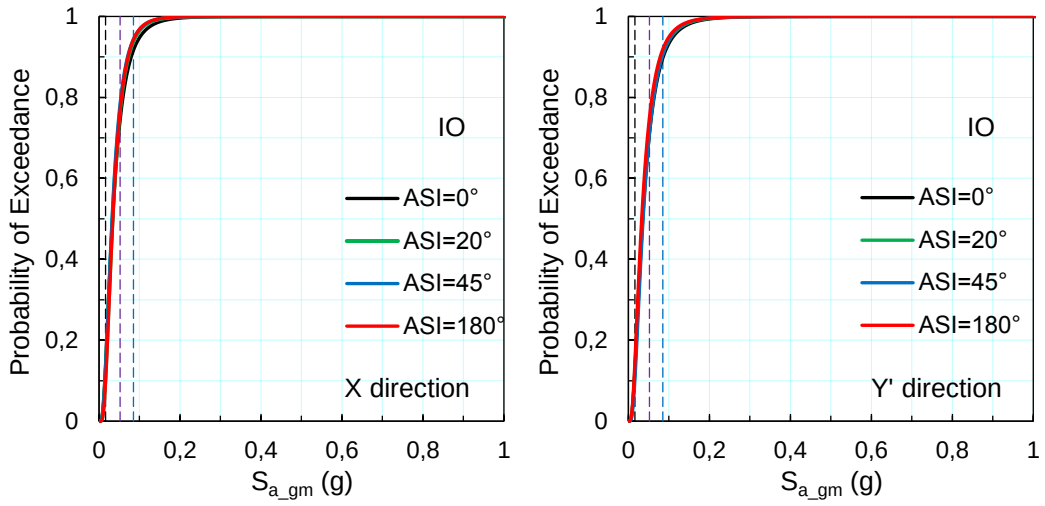

(a) (b)

Figure 6.20 Seismic fragilities for the building in the (a) X direction and (b) Y′ direction for IO performance level (dashed line color code defined in Figure 6.6).

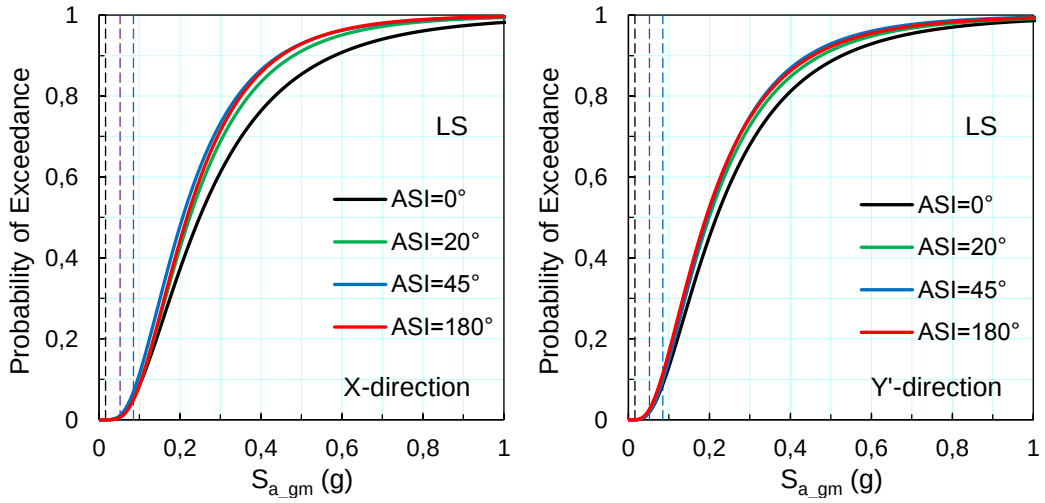

(a) (b)

Figure 6.21 Seismic fragilities for the building in the (a) X direction and (b) Y′ direction for LS performance level (dashed line color code defined in Figure 6.6).

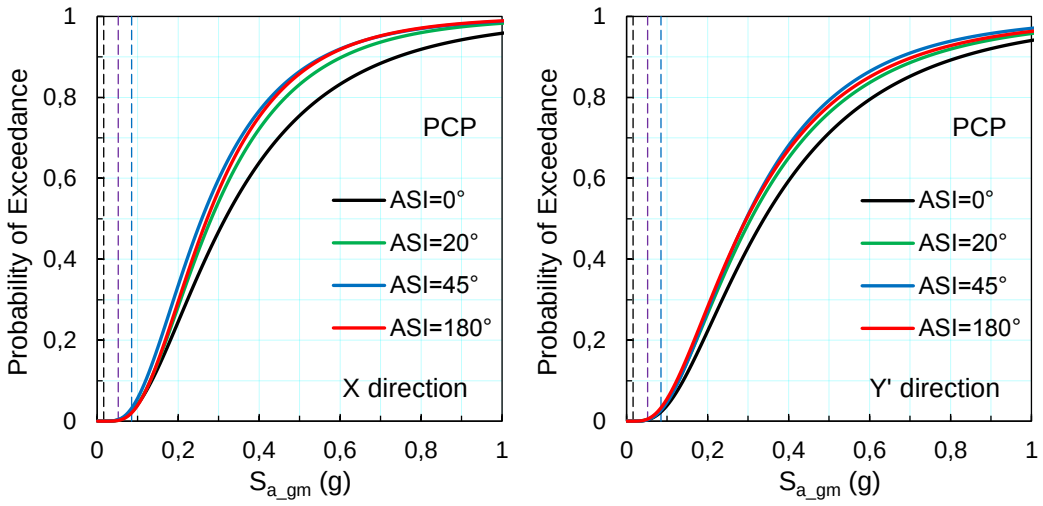

(a) (b)

Figure 6.22 Seismic fragilities for the building in the (a) X direction and (b) Y′direction for PCP performance level (dashed line color code defined in Figure 6.6).

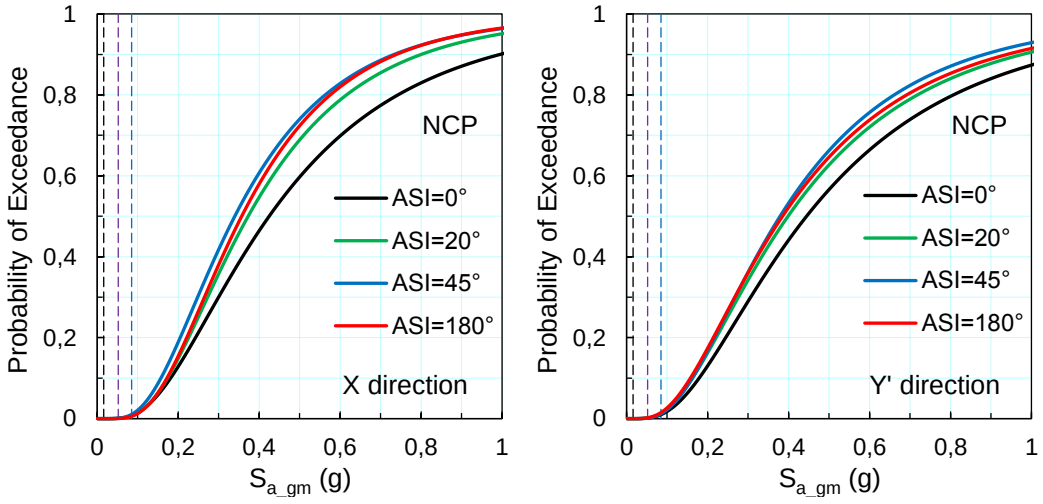

(a) (b)

Figure 6.23 Drift-based seismic fragilities for the building in the (a) X direction and (b) Y′ direction for NCP performance level (dashed line color code defined in Figure 6.6).

Tables 6.8 and 6.9 present the probability of exceeding the limit states in the X direction and Y′ direction, respectively under different hazard levels. The result show that as the intensity increases, especially under the partial and near collapse seismic hazard levels, the variation of the probability of exceeding the limit states increases

for NCP, PCP and LS performance levels. However, the variation of the probability of exceedance the limit states is quite low under MCE, DBE and SLE excitations, typically defined in the seismic codes and/or pertinent guidelines. Although, the variability due to ASI is high within themselves, the effect of ASI becomes less important when all results are evaluated for the same ensemble. The ground motion group size may cause these results since each of the cloud analysis consists of numerous nonlinear dynamic analysis.

Table 6.8 Probabilities of exceeding the limit states in the X direction.

Hazard Level	$S_{a,gm}$ (g)	Probability of exceeding the limit Statas (%)															
		IO				LS				PCP				NCP			
		0°	20°	45°	180°	0°	20°	45°	180°	0°	20°	45°	180°	0°	20°	45°	180°
SLE	0.02	14	11	13	10	0	0	0	0	0	0	0	0	0	0	0	0
DBE	0.05	74	77	78	77	1	1	1	1	0	0	0	0	0	0	0	0
MCE	0.09	92	94	94	94	6	5	7	5	3	2	3	2	0	0	1	1

Table 6.9 Probabilities of exceeding the limit states in the Y′ direction.

Hazard Level	$S_{a,gm}$ (g)	Probability of exceeding the limit Statas (%)															
		IO				LS				PCP				NCP			
		0°	20°	45°	180°	0°	20°	45°	180°	0°	20°	45°	180°	0°	20°	45°	180°
SLE	0.02	13	13	10	14	0	0	0	0	0	0	0	0	0	0	0	0
DBE	0.05	71	73	71	75	2	2	2	3	0	0	0	1	0	0	0	0
MCE	0.09	90	91	91	92	9	10	10	11	3	4	3	3	0	1	1	2

6.7 Summary

The structure-specific or member-specific seismic fragility relationships for defined performance levels were derived. Two different sets of seismic fragility relationship with respect to structural and non-structural components were developed when the ASI was assumed as zero. The effects of ASI on structural response and on ways for accounting for this effect on the seismic fragility relationships were investigated. The drift-based seismic fragility results showed that there are

- 0%, 3.0% probability that the structure will exceed the near collapse and partial collapse performance levels under MCE ground motion pairs
- only 1% probability that the structure will exceed life safety performance level under DBE ground motion pairs
- 14% probability that the structure will exceed the IO performance level under SLE hazard.

Similar results are also obtained maximum plastic rotation-based seismic fragility relationships for each performance level.

The results showed that the maximum interstory drift ratio and plastic rotation of coupling beams vary with different ASI. The variability due to ASI is high but there is no meaningful correlation between ASI when the ground motion pair is interchanged. The results also demonstrated that applying bi-directional ground motion pairs only along the principal axis of the building (when ASI is 0º) underestimates the maximum interstory drift ratio demand when compared to those obtained at other ASI. The most critical angle in the X and Y′ directions were obtained as 45º and 180º, respectively.

CHAPTER 7

SUMMARY, CONCLUSIONS AND FUTURE RESEARCH

7.1 Summary

Tall buildings, most of them located in seismic regions, have been steadily increasing in number worldwide. Istanbul is one of the cities located in a high seismic region where the number of tall buildings has exceeded 200. Design of tall buildings in seismic regions relies on engineering experience and sophisticated computer software.

The objective of this study was to investigate the structural response of tall concrete core wall buildings with outrigger systems in seismic regions. For this purpose, a 253 m tall building in Istanbul was selected as the case study building. Its seismic performance was assessed utilizing the derived fragility curves.

An ambient vibration test of the building was performed to identify its dynamic properties, including the damping properties for service loads. A 3-D linear elastic finite element structural model of the building was developed to determine its natural vibration periods and mode shapes, and compare them with the in-situ dynamic properties. The dynamic properties for the service-level and design-level states of the building were estimated using cracked section properties prescribed in design provisions. A 3-D nonlinear finite element model of the building was subsequently developed based on the validated linear elastic model.

The critical structure- and member-specific response parameters that significantly control the serviceability, safety and collapse performances of the building were determined. The intensities and annual occurrence frequencies of earthquake ground motions leading to local and global collapse were calculated.

The collapse capacity of the building was determined using incremental dynamic analysis. Structure- and member-specific seismic fragility relationships were derived and the performance of the building was evaluated at various levels of earthquake hazard in the region. The effects of angle of seismic incidence on structural response and subsequently on seismic fragilities were discussed.

The findings of this study will further improve the understanding of the seismic performance of tall concrete core wall buildings with outrigger systems under different seismic hazard levels.

7.2 Conclusions

The following conclusions are drawn from this study:

- The first twelve natural frequencies and mode shapes of the building were identified from the recorded ambient vibration data. Due to the parallelogram shape of the building in plan, translational modes are coupled.
- The identified in-situ dynamic properties are used in validating the 3-D linear elastic finite element structural model of the building at the time of testing. No model updating is required if gross section properties with moduli of elasticity for concrete defined in Turkish Building Earthquake Code is used in the model.
- The fundamental period of the building at the time of testing is 5.3 s and is expected to increase to 5.9 s and 7.8 s for the service-level and design-level evaluations in the light of developed structural models, respectively.
- Random decrement method was used to investigate the modal damping ratios. Statistical analysis using the random decrement technique essentially yielded median damping ratios of 0.6% with coefficients of variation in the order of 0.3–0.4 for the first six vibration modes, which can be considered as lower-bound values for service-level evaluations prescribed in design provisions.
- The simulated response of the building to the 2019 M_w 5.8 Marmara Sea earthquake ground motions, recorded at a strong ground motion station in close

proximity to the building, using the median in-situ damping ratios shows that the PFAs under this SLE exceed the ASCE 7-16 [ASCE 2017a] in-structure amplifications at the lower floors and do not reach to those values at the upper floors.

- Perimeter columns and diagonal outrigger members do not undergo inelastic action under the SLE, which conform to the basic design objectives. Further, there is no significant damage in these members under MCE as expected.
- Immediate occupancy performance level under SLE excitation is either controlled by the force response of coupling beams expressed in terms of demand to capacity ratio limits in regions of low wind speeds, or maximum interstory drift ratio limits specified for wind loads in regions of high wind speeds.
- Life safety and partial collapse limit states are controlled by the flexural response limits of coupling beams, whereas near collapse limit state is controlled by the concrete strain limits at the confined shear wall end regions at the B1 or ground floor level.
- An overstrength ratio (the maximum ratio of the MCE to SLE base shear demands) can be defined as 5.8 and 4.6 in X and Y directions. Both factors are about twice the overstrength factors suggested in ASCE 7-16 [ASCE 2017a] for ordinary concrete buildings.
- The annual frequency of the mean earthquake ground motions that will lead to collapse reduces from the target value of 4·10-4 (1/2475) defined for the MCE for ordinary buildings, to 8·10-5 (1/12000) for partial collapse, and to 4·10-5 (1/27000) for near collapse limit states.
- The median yield drift capacity and the aleatoric uncertainty in yield drift capacity were predicted as 0.44% and 0.22% in the X direction and 0.51% and 0.22% in the Y′ direction, respectively. In literature, there are some suggested values for serviceability limit states for tall buildings. For example, HAZUS defined IDR_{max} of 0.50% for high-rise buildings. Ji et al. [2007a] and Pejovic and Jankovic [2016] proposed this value as 0.52% and 0.53%, respectively.

LATBSDC [2020] and PEER-TBI [2017] limited also this value with 0.50%. However, there is no suggested limit in TEBC [AFAD 2018a].

- The median near collapse drift capacity and the aleatoric uncertainties in those were predicted 3.0% and 0.20% in the X direction and 3.4% and 0.24% in the Y′ direction, respectively. In literature, limited information is available for collapse limit state of tall buildings. For example, HAZUS defined IDR_{max} of 4% for high-rise buildings for collapse prevention performance level. Ji et al. [2007a; 2007b; 2009] calculated this value to be 1.1% for tall buildings. Pejovic and Jankovic [2016] found this value as 1.64%. Further, mean IDR_{max} obtained under the MCE ground motion ensemble and the IDR_{max} under each ground motion in the ensemble were limited to 3.0% and 4.5%, respectively in AFAD [2018a], LATBSDC [2020] and PEER-TBI [2017] for CP performance level.
- There is 0%, 3%, 6% and 92% probability that the structure will exceed the NCP, PCP, LS and IO performance level under MCE hazard level, respectively.
- There is no probability that the structure will exceed the NCP, PCP level and only 1% and 74% probability that structure will exceed the LS and IO performance level under DBE level.
- There is 14% probability that the structure will exceed the IO performance level under SLE hazard. It is possible to increase the seismic performances of the coupling beams for a better performance under SLE excitations.
- There is 3%, 8%, and 98% probability that the coupling beams will exceed the damage state for the PCP (or CP), LS and IO performance levels under MCE hazard level, respectively.
- There is 1% of probability that the structure will exceed the LS performance level under DBE hazard level.
- There is 19% of probability that the coupling beam will exceed IO performance level under SLE excitations. Similar to the results obtained drift-based seismic fragility curves.
- The developed peak floor acceleration based seismic fragility relationship results show that ground and top floor level are more vulnerable than other stories.

- The maximum interstory drift ratio and plastic rotation of coupling beams vary with the different ASI. The variability due to ASI is so high but there is no a meaningful correlation between ASI when the ground motion pair is interchanged.
- The results also demonstrated that applying bi-directional ground motion pairs only along the principal axis of the building (when ASI is 0º) underestimates the maximum interstory drift ratio demand when compared to those obtained at other ASI especially when seismic intensity increases.
- The results show that the most critical angle at the X and Y′ direction is 45º and 180º, respectively.
- Although the variability due to ASI is so high within themselves, the effect of ASI becomes less important on the derived seismic fragility curves

7.3 Future Research

This study can be extended in the following areas:

- The calculation of the modeling uncertainty such as the effect of the structural material properties, structural damping and more factors that may affect the modeling uncertainty should be considered.
- Multiple stripes analysis method should be used for the development of seismic fragility curves. The results obtained in this study should be compared with them.
- The joint effect of both the ground motion size (how many records should be used) and the ASI on the estimation of seismic fragility of tall building should be investigated.
- The yield and collapse capacity of the building should be determined considering different ASI and their impact on seismic fragility curves should be evaluated.
- The effect of selection seismic IMs on the deriving seismic fragility of tall buildings should be investigated.
- Financial aspects of the building including initial costs and projected damage repair costs associated with future earthquakes should be studied.

REFERENCES

ACI [2014] Building Code Requirements for Structural Concrete (ACI 318-14) and Commentary (ACI 318R-14). ACI Committee 318, American Concrete Institute, Farmington Hills, MI.

AFAD [2018a] Turkish earthquake code for buildings. Disaster and Emergency Management Authority, Ankara, Turkey.

AFAD [2018b] Seismic hazard maps of Turkey. Disaster and Emergency Management Authority, Ankara, Turkey. https://tdth.afad.gov.tr. Accessed 14 January 2022.

AFAD [2020] Guidelines for Structural Health Monitoring Systems. Disaster and Emergency Management Authority, Ankara, Turkey (in Turkish).

AFAD [2022] Turkish Acceleration Database and Analysis System, https://tadas.afad.gov.tr [28 April 2022]. Disaster and Emergency Management Authority, Ankara, Turkey.

Akkar S, Sucuoglu H, Yakut A [2005] Displacement-based fragility functions for low- and mid-rise ordinary concrete buildings. Earthquake Spectra 21(4): 901–927.

Akkar S [2014] Site-specific probabilistic hazard assessment to compute elastic response spectra of 43-year, 475-year and 2475-year return periods for Istanbul Tower 205 project and corresponding scaled ground motions, Report. Istanbul, Turkey.

Alwaeli W, Mwafy A, Pilakoutas K, Guadagnini M [2017] A methodology for defining seismic scenario-structure-based limit state criteria for RC high-rise wall buildings using net drift. Earthquake Engineering and Structural Dynamics 46: 1325–1344.

Anajafi H, Medina RA [2018] Evaluation of ASCE 7 equations for designing acceleration-sensitive nonstructural components using data from instrumented buildings. Earthquake Engineering and Structural Dynamics 47(4): 1075–1094.

Arup Inc. [2013] Conceptual design report of Istanbul Tower 205. Istanbul, Turkey.

ASCE [2012] Wind tunnel testing for building and other structures, ASCE/SEI 49-12. American Society of Civil Engineers, Reston, VA.

ASCE [2017a] Minimum Design Loads and Associated Criteria for Buildings and Other Structures. ASCE/SEI 7-16, American Society of Civil Engineers, Reston, VA.

ASCE [2017b] Seismic Evaluation and Retrofit of Existing Buildings. ASCE 41-17. American Society of Civil Engineers, Reston, VA.

Baker WF [2006] Validating wind-induced response of tall buildings: Synopsis of the Chicago full-scale monitoring program. Journal of Structural Engineering 132(10): 1509–1523.

Bernal D, Dohler M, Kojidi SM, Kwan K, Liu Y [2015] First mode damping ratios for buildings. Earthquake Spectra 31(1): 367–381.

Bilotta A, Tomeo R, Nigro E, Manfredi G [2018] Evaluation of the seismic demand of an existing tall building. Ingegneria Sismica 35(1): 67-87.

Bindi D, Petrovic B, Karapetrou S, Manakou M, Boxberger T, Raptakis D, Pitilakis KD, Parolai S [2015] Seismic response of an 8-story RC-building from ambient vibration analysis. Bulletin of Earthquake Engineering 13(7): 2095–2120.

Budak E, Sucuoğlu H, Konca F, Uludag A [2018] Performance based seismic evaluation of a 62 story RC tower in Istanbul. 16th European Conference on Earthquake Engineering, Thessaloniki, Greece.

Budak E, Sucuoğlu H [2016] Performance based seismic design of reinforced concrete tall buildings, 16th World Conference on Earthquake Engineering, Santiago, Chile.

Celebi M [2000] Seismic instrumentation of buildings: USGS Open-File Report 2000-157. Menlo Park, CA: US Geological Survey.

Celebi M [2016] Response of a 58-story RC dual core shear wall and outrigger frame building inferred from two earthquakes. Earthquake Spectra 32(4): 2449–2471.

Celebi M, Safak E [1991] Seismic response of Transamerica Building. I: Data and preliminary analysis. Journal of Structural Engineering 117(8): 2389–2404.

Celebi M, Sereci M, Boroschek R, Carreno R, Bonelli P [2013a] Identifying the dynamic characteristics of a dual core-wall and frame building in Chile using aftershocks of the 27 February 2010 (M_w=8.8) Maule, Chile, earthquake. Earthquake Spectra 29(4): 1233–1254.

Celebi M, Huang M, Shakal A, Hooper J, Klemencic R [2013b] Ambient response of a unique performance-based design tall building with dynamic response modification features. The Structural Design of Tall and Special Buildings 22: 816–829.

Celebi M, Kashima T, Ghahari FS, Abazarsa F, Taciroglu E [2016] Response of a tall building with U.S. code-type instrumentation in Tokyo, Japan, to events before, during and after the Tohoku Earthquake of 11 March 2011. Earthquake Spectra 32(1): 497–522.

Celebi M, Kashima T, Ghahari AF, Koyama S, Taciroglu E, Okawa I [2017a] Before and after retrofit behavior and performance of a 55-story tall building inferred from distant earthquake and ambient vibration data. Earthquake Spectra 33(4): 1599–1626.

Celebi M, Hooper J, Klemencic R [2017b] Study of response of 64-story Rincon Building to Napa, Fremont, Piedmont, San Ramon Earthquakes and ambient motions. Earthquake Spectra 33(3): 1125–1148.

Celebi M, Haddadi H, Huang M, Valley M, Hooper J, Klemencic R [2019] The behavior of the Salesforce Tower, the tallest building in San Francisco, California inferred from earthquake and ambient shaking. Earthquake Spectra 35(4): 1711–1737.

Celik OC [2007] Probabilistic assessment of non-ductile reinforced concrete frames susceptible to Mid-America ground motions. Ph.D. dissertation, School of Civil and Environmental Engineering, Georgia Institute of Technology, Atlanta, GA.

Celik OC, Ellingwood BR [2010a] An efficient seismic intensity measure for seismic risk analysis of structures. 9th US National and 10th Canadian Conference on Earthquake Engineering, July 25–29, Toronto, Canada.

Celik OC, Ellingwood BR [2010b] Seismic fragilities for non-ductile reinforced concrete frames – role of aleatoric and epistemic uncertainties. Structural Safety 32(1): 1–12.

Celik OC, Gulkan HP [2021a] Processing forced vibration test records of structural systems using the analytical signal. Journal of Vibration and Control 27(19-20): 2253–2267.

Celik OC, Gulkan HP [2021b] System identification for a six-storey precast concrete frame building. Magazine of Concrete Research 73(10): 527–539.

Celik OC, Sucuoglu H, Akyuz U [2015] Forced vibration testing and finite element modeling of nine-story reinforced concrete flat plate-wall building. Earthquake Spectra 31(2): 1069–1081.

CEN [2004] Eurocode 2: Design of Concrete Structures. EN 1992-1-1, European Committee for Standardization, Brussels, Belgium.

Choi HS [2009] Super Tall Building Design Approach, The American Institute of Architects Continuing Education Systems Program, Thornton Tomasetti Inc., New York, NY.

Choi HS, Joseph L [2012] Outrigger system design considerations. International Journal of High-Rise Buildings 1(3): 237–246.

Colaco J [2005] Structural systems for tall apartment towers. CTBUH 7th World Congress, New York, NY.

Cole HA [1973] On-Line Failure Detection and Damping Measurement of Aerospace Structures by Random Decrement Signatures. Report No. NASA CR-2205, National Aeronautics and Space Administration, Washington, D.C.

Cornell C A, Jalayer F, Hamburger RO, Foutch DA [2002] Probabilistic basis for 2000 SAC Federal Emergency Management Agency steel moment frame guidelines. Journal of Structural Engineering 28(4): 526–533.

Cruz C, Miranda E [2017] Evaluation of damping ratios for the seismic analysis of tall buildings. Journal of Structural Engineering 143(1): 04016144.

CSI [2016] Perform3D version 6.0, Performance-based design of 3D structures. Computers and Structures Inc., Walnut Creek, CA.

CSI [2020] ETABS, Building Analysis and Design. Computers and Structures, Inc., Walnut Creek, CA.

CTBUH [2022] Council on Tall Buildings and Urban Habitat, https://www.ctbuh.org [02 Nowember 2022], Chicago, IL.

Ellingwood BR, Celik OC, Kinali K [2007]. Fragility assessment of building structural systems in Mid-America. Earthquake Engineering and Structural Dynamics 36: 1935–1952.

El-Tawil, S, Deierlein, GG [2001a]. Nonlinear analysis of mixed steel-concrete frames. I: Element formulation. Journal of Structural Engineering 127(6): 647–655.

El-Tawil, S, Deierlein, GG [2001b] Nonlinear analysis of mixed steel-concrete frames. II: Implementation and verification. Journal of Structural Engineering, 127(6): 656–665.

European Committee for Standardization [2005] Eurocode 1: Actions on structures, EN 1991-1-4. Brussels, Belgium.

Fan H, Li QS, Tuan AY, Xu L [2009] Seismic analysis of the world's tallest building. Journal of Constructional Steel Research 65: 1206–1215.

FEMA [2000] State of the art report on performance prediction and evaluation of steel moment-frame buildings, FEMA-355F. Federal Emergency Management Agency Washington, D.C.

FEMA [2020] NEHRP recommended seismic provisions for new buildings and other structures, FEMA P-2082-1. Federal Emergency Management Agency, Washington, D.C.

Fontara IKM, Kostinakis GK, Manoukas EG, Athanatopoulou A [2015] Parameters affecting the seismic response of buildings under bi-directional excitation. Structural Engineering Mechanics 53(5): 957–979.

Giannopoulos D, Vamvatsikos D [2018] Ground motion records for seismic performance assessment: to rotate or not to rotate? Earthquake Engineering and Structural Dynamics 47(12): 2410–2425.

Guralp Systems [2009] CMG-DM24, Mk3 Digitizer, Operator's Guide, Part No. MAN-D24-0004, Aldermaston, England.

Guralp Systems [2013] CMG-5U, Single-Axis Accelerometer, Operator's Guide, Document No. MAN-050-0002, Aldermaston, England.

Jayaram N, Shome N, Rahnama M [2012] Development of earthquake damage functions for tall buildings. Earthquake Engineering and Structural Dynamics 41: 1495–1514.

Ji J, Elnashai AS, Kuchma DA [2007a] An analytical framework for seismic fragility analysis of RC high-rise buildings. Engineering Structures 29: 3197–3209.

Ji J, Elnashai AS, Kuchma DA [2007b] Seismic fragility assessment for reinforced concrete high-rise buildings. Report 07-14, Mid-America Earthquake Center, University of Illinois at Urbana-Champaign, Urbana, IL.

Ji J, Elnashai AS, Kuchma DA [2009] Seismic fragility relationships for reinforced concrete high-rise buildings. The Structural Design of Tall and Special Buildings 18: 259–277.

Kalkan E, Reyes JC [2015] Significance of rotating ground motions on behavior of symmetric- and asymmetric-plan structures: part II. Multi-story structures. Earthquake Spectra 31(3): 1613–1628.

Kinali K, Ellingwood BR [2007] Seismic fragility assessment of steel frames for consequence-based engineering: a case study for Memphis, TN. Engineering Structures 29(6): 1115–1127.

Kijewski T, Kareem A [2002] On the reliability of a class of system identification techniques: insights from bootstrap theory. Structural Safety 24(2–4): 261–280.

Kijewski-Correa T, Kilpatrick J, Kareem A, Kwon D, Bashor R, Kochly M, Young B S, Abdelrazaq A, Galsworthy J, Isyumov N, Morrish D, Sinn RC, Baker WF [2006] Validating wind-induced response of tall buildings: Synopsis of the Chicago full-scale monitoring program. Journal of Structural Engineering 132(10): 1509–1523.

Korista DS, Sarkisian MP, Abdelrazaq AK [1997] Jin Mao Tower - Shanghai response of an ultra-tall building to moderate seismic forces. In: Proceedings of the Fourth Conference on Tall Buildings in Seismic Regions, Los Angeles, California, pp 171‑186.

Kostinakis KG, Manoukas GE, Athanatopoulou AM [2018] Influence of seismic incident angle on response of symmetric in plan buildings. KSCE Journal of Civil Engineering 22(2): 725–735.

Kwon OS, Elnashai A [2006] The effect of material and ground motion uncertainty on the seismic vulnerability curves of RC structure. Engineering Structures 28: 289-303.

Lagaros ND [2010] The impact of the earthquake incident angle on the seismic loss estimation. Engineering Structures 32(6): 1577–1589.

LATBSDC [2015] An Alternative Procedure for Seismic Analysis and Design of Tall Buildings Located in the Los Angeles Region. Los Angeles Tall Buildings Structural Design Council, Los Angeles, CA.

LATBSDC [2017] An Alternative Procedure for Seismic Analysis and Design of Tall Buildings Located in the Los Angeles Region. Los Angeles Tall Buildings Structural Design Council, Los Angeles, CA.

LATBSDC [2020] An Alternative Procedure for Seismic Analysis and Design of Tall Buildings Located in the Los Angeles Region. Los Angeles Tall Buildings Structural Design Council, Los Angeles, CA.

Lowes LN, Lehman DE, Baker C [2016] Recommendations for modeling the nonlinear response of slender reinforced concrete walls using Perform-3D. In: SEAOC Convention. Maui, Hawaii.

Lu X, Xiao L, Guan H, Zhang W, Ye L [2013] Earthquake-induced collapse simulation of a super-tall mega-braced frame-core tube building. Journal of Constructional Steel Research 82: 59–71.

Lucchini A, Monti G, Kunnath S [2011] Nonlinear response of two-way asymmetric single-story building under biaxial excitation. Journal of Structural Engineering 137(1): 34–40.

Luco N, Cornell CA [2007] Structure-specific scalar intensity measures for near-source and ordinary earthquake ground motions. Earthquake Spectra 23(2): 357–392.

Magalhaes F, Cunha A, Caetano E, Brincker R [2010] Damping estimation using free decays and ambient vibration tests. Mechanical Systems and Signal Processing 24(5): 1274–1290.

Mander JB, Priestley MJN, Park R [1988] Observed stress-strain behavior of confined concrete, Journal of Structural Engineering, ASCE: 114(8): 1827–1849.

Moehle JP [2008] Performance-based seismic design of tall buildings in the US. The 14th World Conference on Earthquake Engineering, Beijing, China.

Moehle JP, Ghodsi T, Hooper JD, Fields DC, Gedhada R [2012] Seismic Design of Cast-in-Place Concrete Special Structural Walls and Coupling Beams, NIST GCR 11-917-11REV-1, National Institute of Standards and Technology, Gaithersburg, MD, 2012.

MPWS [2007] Specification for buildings to be built in seismic zones. Ministry of Public Works and Settlement, Ankara, Turkey.

Mwafy A [2012] Analytical derived fragility relationships for the modern high-rise building in the UAE. The Structural Design of Tall and Special Buildings 21: 824–843.

Naish D, Wallace JW, Fry JA, Klemencic R [2009] Experimental evaluation and analytical modeling of ACI 318-05/08 reinforced concrete coupling beams subjected to reversed cyclic loading. Report to Charles Pankow Foundation School of Engineering and Applied Science, University of California, Berkeley, CA.

National Institute of Building Sciences [1999] HAZUS technical manual, prepared for Federal Emergency Management Agency, Washington, DC.

NEHRP [2013] Nonlinear Analysis Research and Development Program for Performance-Based Seismic Engineering, NIST GCR 14-917-27, U.S Department of Commerce.

Nguyen V T, Kim D [2013] Influence of incident angles of earthquakes on inelastic responses of asymmetric-plan structures. Structural Engineering Mechanics 45(3): 373–389.

Pan Y, Ventura CE, Feng Y, Li X, Kaya Y, Xiong H, Zhang F, Cao J, Zhou M [2016] Ambient vibration testing of a super tall building in Shanghai. The Society for Experimental Mechanics, Inc, Dynamics of Civil Structures, Volume 2, Conference Proceedings of the Society for Experimental Mechanics Series.

PEER [2010] Modeling and acceptance criteria for seismic design and analysis of tall buildings, PEER/ATC 72-1. Pacific Earthquake Engineering Research Center, Richmond, CA.

PEER [2017] Guidelines for performance-based seismic design of tall buildings, PEER Report No. 2017/06. Pacific Earthquake Engineering Research Center, Berkeley, CA.

PEER [2022] PEER Ground Motion Database. Pacific Earthquake Engineering Research Center, Berkeley, CA. http://ngawest2.berkeley.edu [14 January 2022].

Pejovic J, Jankovic S [2016] Seismic fragility assessment for reinforced concrete high-rise buildings in Southern Euro-Mediterranean Zone. Bulletin of Earthquake Engineering 14(1): 185–212.

Porter KA, Beck JL, Shaikhutdinov RV [2002] Sensitivity of building loss estimates to major uncertain variables. Earthquake Spectra, 18(4): 719-743.

Pugh JS, Lowes LN, Lehman DE [2015] Nonlinear line-element of flexural reinforced concrete walls. Engineering Structures 104: 174–192.

Reinoso E, Miranda E [2005] Estimation of floor acceleration demands in high-rise buildings during earthquakes. The Structural Design of Tall and Special Buildings 14(2): 107–130.

Rigato AB, Medina RA [2007] Influence of angle of incidence on seismic demands for inelastic single-storey structures subjected to bi-directional ground motions. Engineering Structures 29(10): 2593–2601.

Rodrigues J, Brincker R [2005] Application of the random decrement technique in operational modal analysis. Proceedings of the First International Operational Modal Analysis Conference, April 26–27, Copenhagen, Denmark.

Rossetto T, Elnashai A [2003] Derivation of vulnerability functions for European-type RC structures based on observational data. Engineering Structures 25(10): 1241–1263.

Saatcioglu M, Razvi S [1992] Strength and ductility of confined concrete, Journal of Structural Engineering, ASCE, 118(6): 1590-1607.

Safak E, Cakti E [2014] Simple techniques to analyze vibration records from buildings. Proceedings of the Seventh European Workshop on Structural Health Monitoring, July 8–11, Nantes, France.

Sara Electronic Instruments [2022] https://www.sara.pg.it [28 April 2022], Perugia, Italy.

Satake N, Suda K, Arakawa T, Sasaki A, Tamura Y [2003] Damping evaluation using full-scale data of buildings in Japan. Journal of Structural Engineering 129(4): 470–477.

SEAONC [2007] Recommended administrative bulletin on the seismic design and review of tall buildings using non-prescriptive procedures, AB-083. Structural Engineers Association of Northern California, San Francisco, CA.

Shome N, Jayaram N, Krawinkler H, Rahnama M [2015] Loss estimation of tall buildings designed for the PEER Tall Building Initiative Project. Earthquake Spectra 31(3): 1309-1336.

Skoulidou D, Romao X [2019] Uncertainty quantification of fragility and risk estimates due to seismic input variability and capacity model uncertainty. Engineering Structures 195: 425–437.

Skoulidou D, Romao X [2020] The significance of considering multiple angles of seismic incidence for estimating engineering demand parameters. Bulletin of Earthquake Engineering 18(1): 139–163.

Skoulidou D, Romao X [2021] Are seismic losses affected by the angle of seismic incidence? Bulletin of Earthquake Engineering 19: 6271-6302.

Skoulidou D, Romao X, Franchin P [2019] How is collapse risk of RC buildings affected by the angle of seismic incidence? Earthquake Engineering and Structural Dynamics 48: 1575–1594.

Smith R [2011] Deflection limits in tall buildings are they useful? Structures Congress 2011. American Society of Civil Engineers, Las Vegas, Nevada, pp 515–527.

Spanos PD, Zeldin BA [1998] Generalized random decrement method for analysis of vibration data. Journal of Vibration and Acoustics 120(3): 806–813.

Tamura Y, Suganuma S [1996] Evaluation of amplitude-dependent damping and natural frequency of buildings during strong winds. Journal of Wind Engineering and Industrial Aerodynamics 59(2–3): 115–130.

Tamura Y, Zhang L, Yoshida A, Nakata S, Itoh T [2002] Ambient vibration tests and modal identification of structures by FDD and 2DOF-RD technique. Proceedings of the Structural Engineers World Congress, October 9–12, Yokohama, Japan.

Todorovska MI, Niu B, Lin G, Cao C, Wang D, Cui J, Wang F, Trifunac M D, Liang J [2020] A new full-scale testbed for structural health monitoring and soil-structure interaction studies: Kunming 48-story office building in Yunnan province, China. Structural Control and Health Monitoring e2545.

TSI [2000] Requirements for Design and Construction of Reinforced Concrete Structures. TS 500, Turkish Standards Institute, Ankara, Turkey (in Turkish).

Vandiver JK, Dunwoody AB, Campbell RB, Cook MF [1982] A mathematical basis for the random decrement vibration signature analysis technique. Journal of Mechanical Design 104(2): 307–313.

Ventura CE, Lord JF, Turek M, Brincker R, Andersen P, Dascotte E [2005] FEM updating of tall buildings using ambient vibration data. Structural Dynamics EURODYN 2005: Proceedings of 6th International Conference on Structural Dynamics, Paris, France, (pp. 237-242). Millpress.

Wallace JW [2007] Modeling issues for tall reinforced concrete core wall buildings. The Structural Design of Tall and Special Buildings 16: 615–632.

Wang S, Lai JW, Schoettler MJ, Mahin SA [2017] Seismic assessment of existing tall buildings: A case study of a 35-story steel building with pre Northridge connection. Engineering Structures 141: 624–633.

Welch PD [1967] The use of fast Fourier transforms for the estimation of power spectra: A method based on time averaging over short, modified periodograms. IEEE Transactions on Audio and Electroacoustics AU-15(2): 70–73.

Wen YK, Ellingwood BR, Bracci J [2004] Vulnerability function framework for consequence-based engineering. Mid-America Earthquake Center Project DS-4 report. University of Illinois at Urbana-Champaign, Urbana, IL.

Wen Q, Hua XG, Chen ZQ, Niu HW, Wang XY [2018] AMD-based random decrement technique for modal identification of structures with close modes. Journal of Aerospace Engineering 31(5): 04018057.

Wilson EL, Suharwardy I, Habibullah A [1995] A clarification of the orthogonal effects in a three- dimensional seismic analysis. Earthquake Spectra 11(4): 659–666

WTG [1996] Windkanaluntersuchungen in der Gebaudeaerodynamik, Windtechnologische Gesellschaft (in German)

Zekioglu A, Willford M, Jin L, Melek M [2007] Case study using the Los Angeles tall buildings structural design council guidelines: 40-storey concrete core wall building. The Structural Design of Tall and Special Buildings 16: 583–597.

Zhang Y, He Z [2020] Seismic collapse risk assessment of super high-rise buildings considering modeling uncertainty: A case study. The Structural Design of Tall and Special Buildings 29: e1687.

Zhang AL, Ventura CE, Xiong H, Lu W, Pan Y, Cao J [2018] Evaluation of the dynamic characteristics of a super tall building using data from ambient vibration and shake table tests by a Bayesian approach. Structural Control and Health Monitoring 25: e2121.

Zhou Y, Zhou Y, Yi W, Chen T, Tan D, Mi S [2017] Operational modal analysis and rational finite-element model selection for ten high-rise buildings based on on-site ambient vibration measurements. Journal of Performance of Constructed Facilities, 31(5): 04017043.

Zhou K, Li Q [2021] Reliability analysis of damping estimation by random decrement technique for high-rise buildings. Earthquake Engineering and Structural Dynamics 50(5): 1251–1270.

APPENDIX A

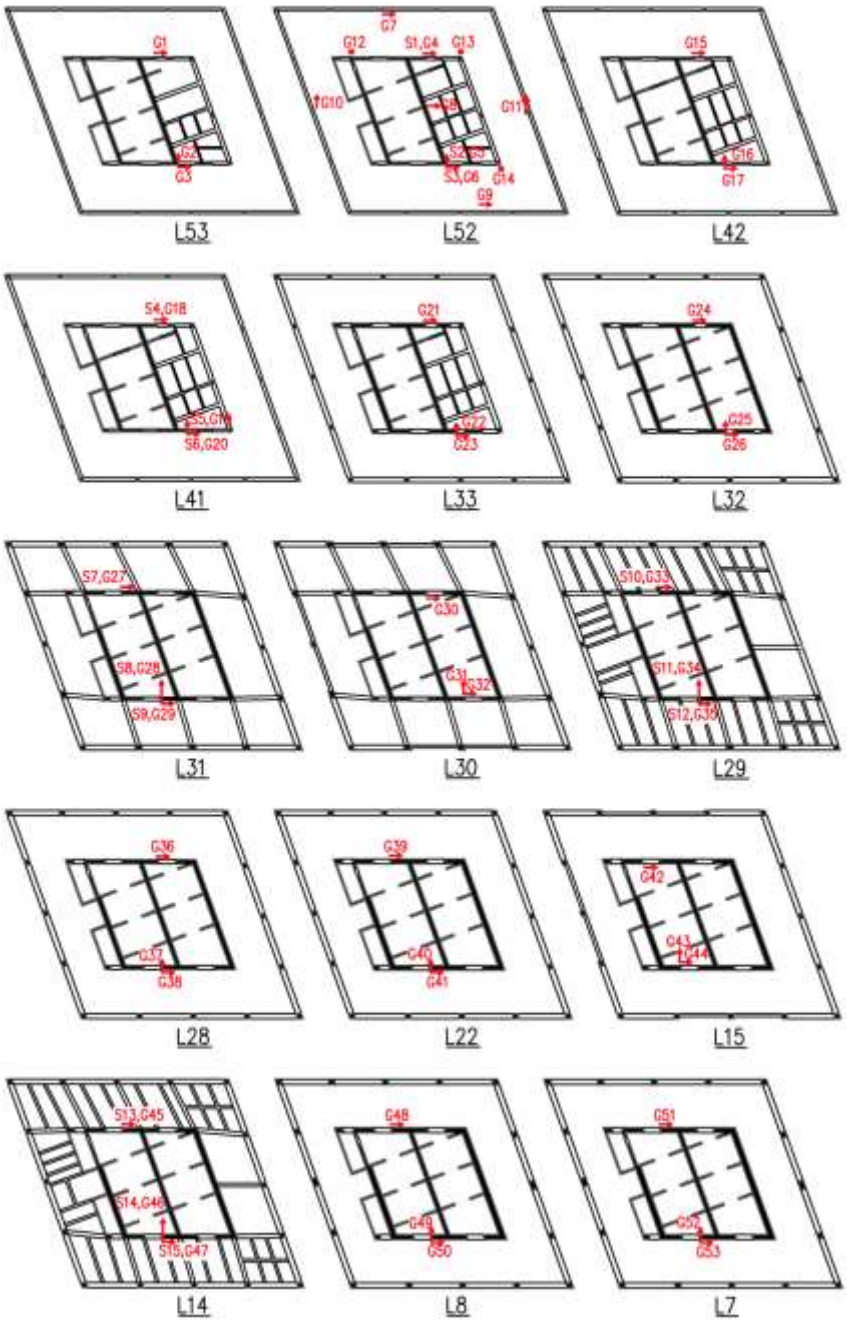

Figure A.1 Plan views of the floors where accelerometers are deployed through the building.

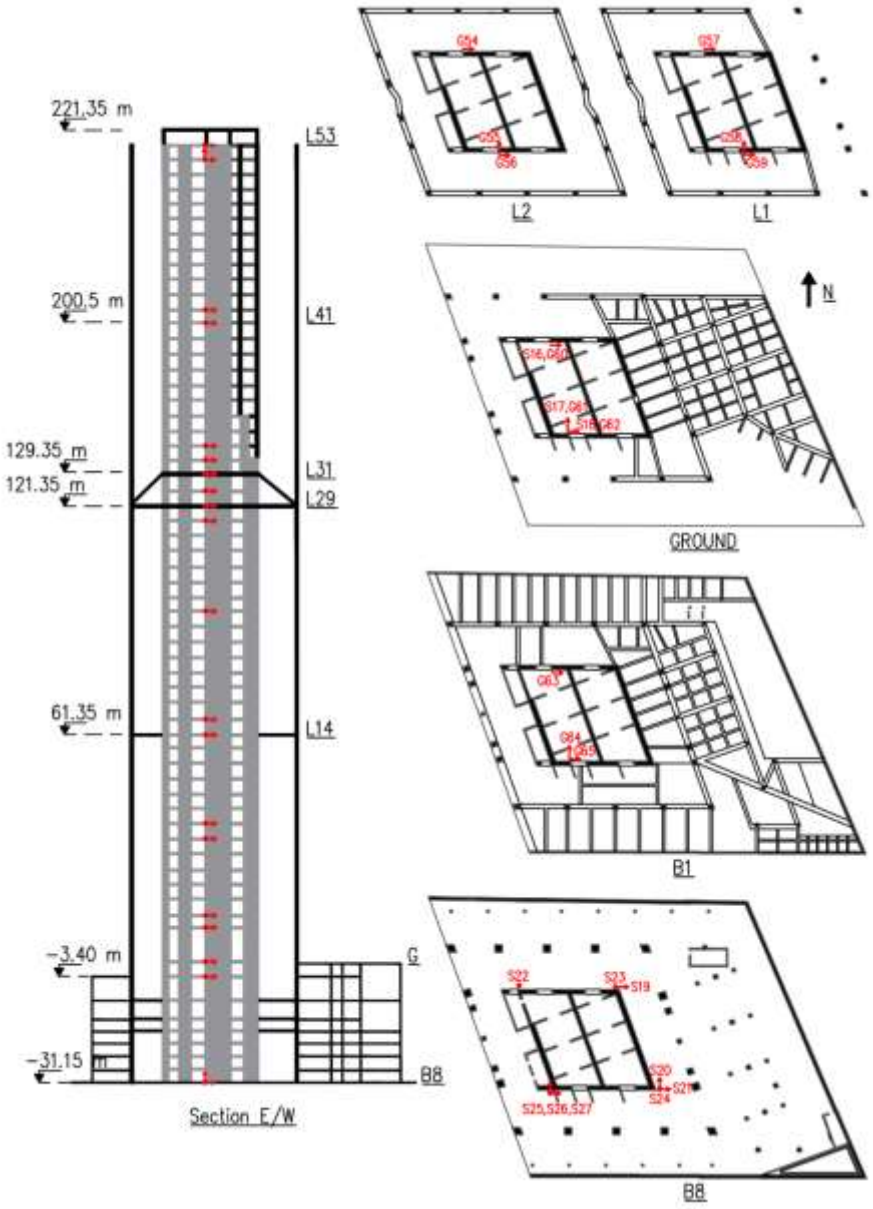

Figure A.2 Vertical section and plan views of the floors where accelerometers are deployed through the building.

APPENDIX B

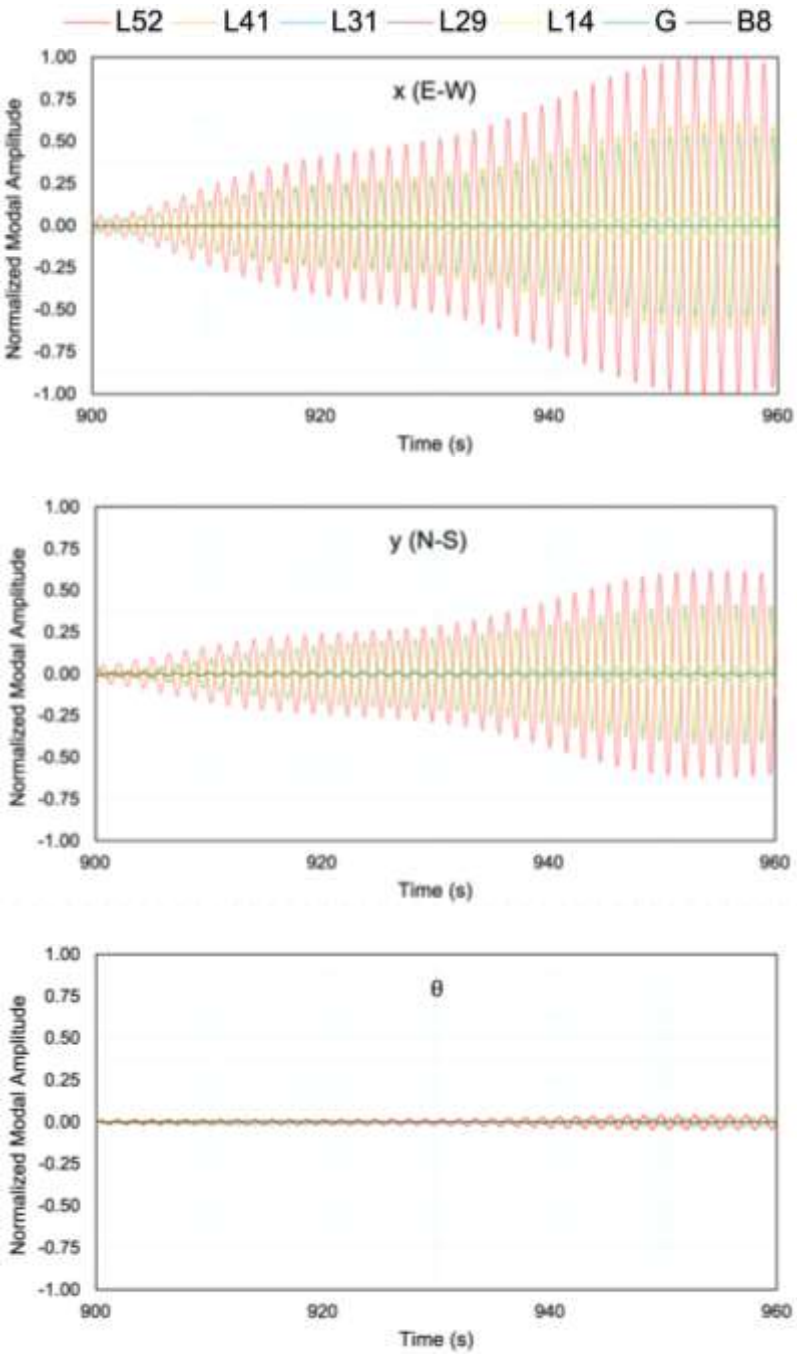

Figure A.3 Normalized modal time histories for the forth mode: 12.09.2018 10:00:00 GMT.

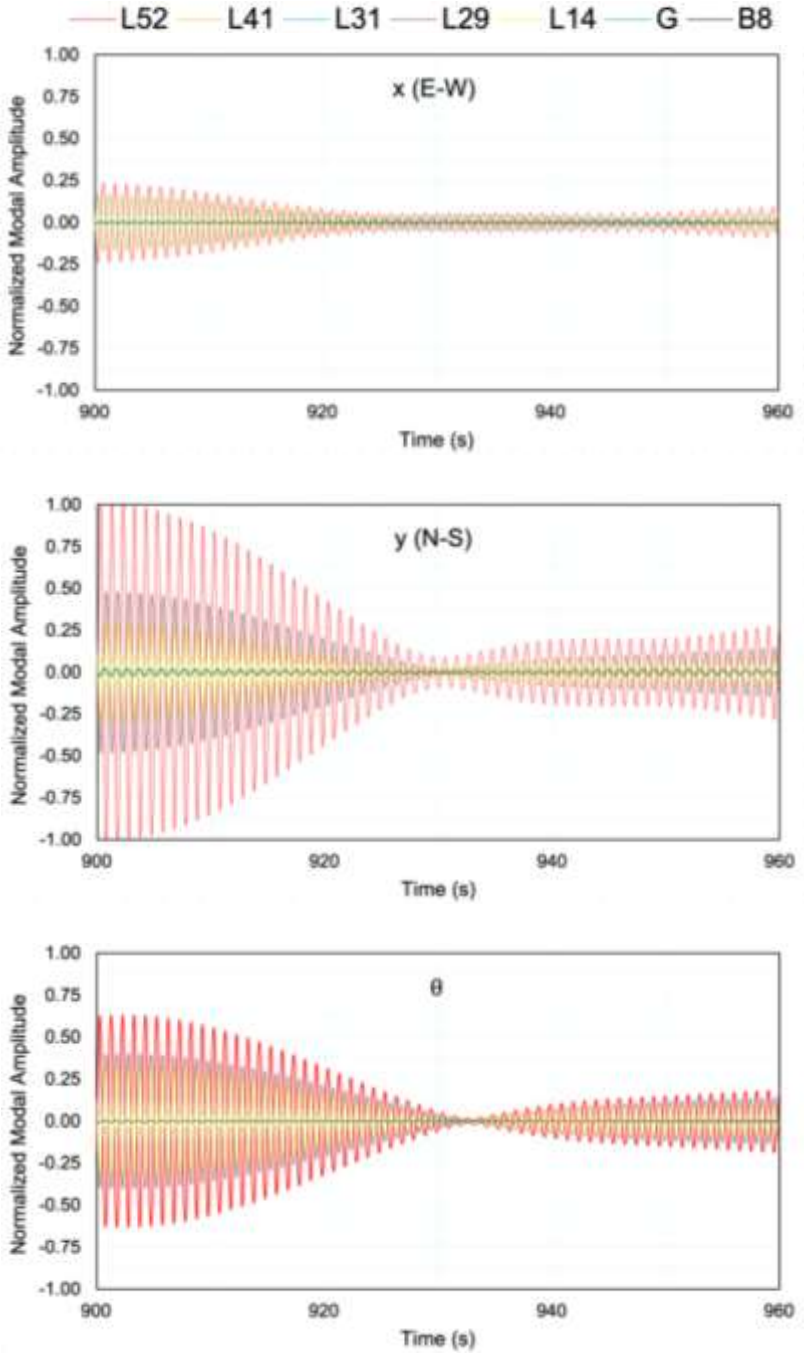

Figure A.4 Normalized modal time histories for the fifth mode: 12.09.2018 10:00:00 GMT.

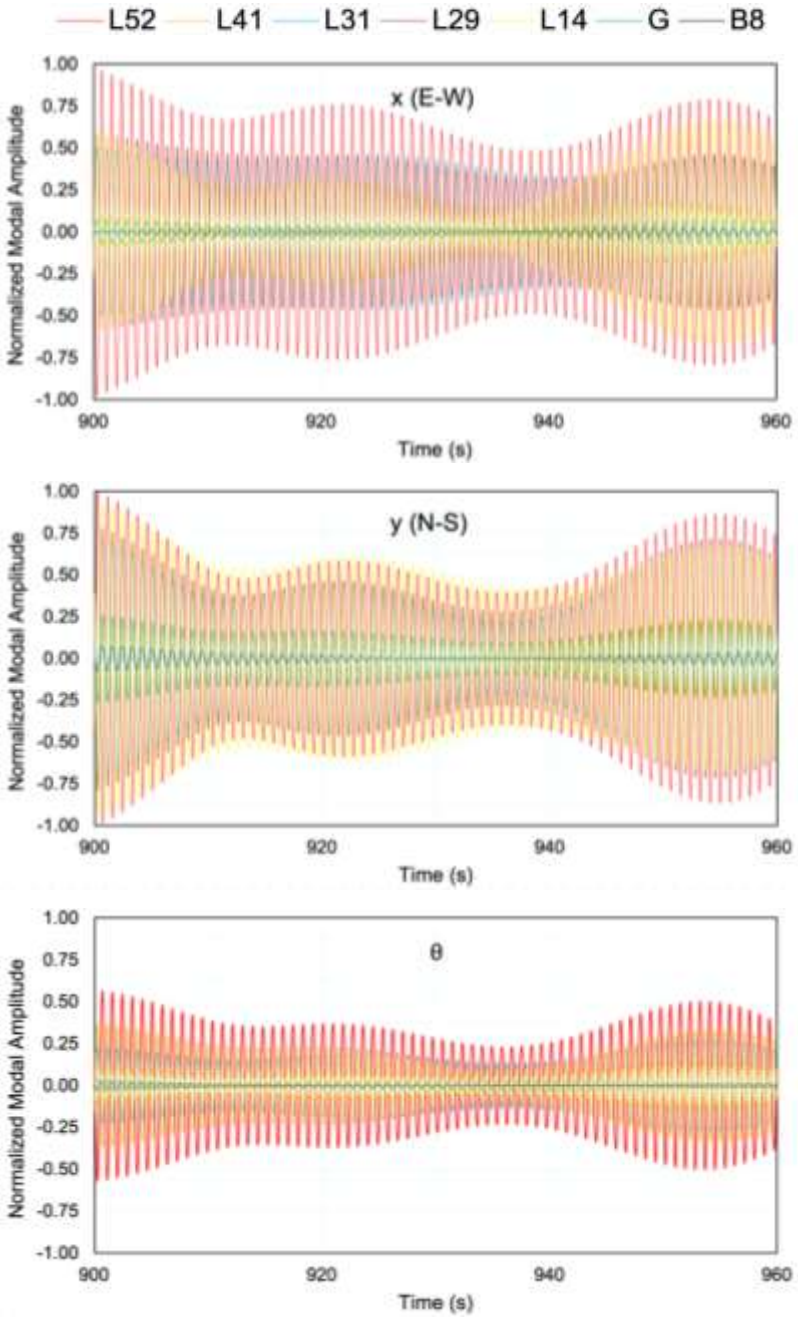

Figure A.5 Normalized modal time histories for the sixth mode: 12.09.2018 10:00:00 GMT.

CURRICULUM VITAE

Surname, Name: Budak, Erhan

EDUCATION

Degree	Institution	Year of Graduation
MS	METU Civil Engineering	2015
BS	YTU Civil Engineering	2011
High School	Kızıltepe Anadolu High School, Mardin	2005

FOREIGN LANGUAGES

English, Kurdish

PUBLICATIONS

Budak E, Sucuoğlu H, Konca F, Uludag A [2018] Performance based seismic evaluation of a 62 story RC tower in Istanbul. 16th European Conference on Earthquake Engineering, Thessaloniki, Greece.

Budak E, Sucuoglu H and Celik OC [2022] Response parameters that control the service, safety and collapse performances of a 253 m tall concrete core wall building in Istanbul. Bulletin of Earthquake Engineering (in press).